Magnetic Outflows in the Virgo Galaxy NGC 4388

Dissertation

zur

Erlangung des Doktorgrades (*Dr. rer. nat.*)

der

Mathematisch-Naturwissenschaftlichen Fakultät

der

Rheinischen Friedrich–Wilhelms–Universität
Bonn

vorgelegt von

Damas Segovia, Ancor

aus

Madrid, Spanien

Bonn 2016

RHEINISCHEN
FRIEDRICH–WILHELMS–UNIVERSITÄT BONN

Abstract

by Ancor Damas Segovia

for the degree of

Doctor rerum naturalium

We investigate the effects of ram pressure on the ordered magnetic field of the edge-on Virgo galaxy NGC 4388 hosting a radio halo and strong nuclear outflows. New radio images in total and polarized intensity were obtained within the CHANG-ES EVLA project. The unprecedented noise level reached allows us to detect striking new features of the ordered magnetic field. The nuclear outflow driven by an AGN extends far into the halo to about 5 kpc from the center and is spatially correlated with $H\alpha$ and X-ray emission. For the first time, a southern outflow is detected. Above and below both spiral arms we find extended blobs of polarized emission with an ordered field oriented perpendicular to the disk, probably generated by a galactic wind driven by star formation in the underlying spiral arms. The synchrotron lifetime of the cosmic-ray electrons (CREs) in these regions yields a mean outflow velocity of $(270 \pm 70)\,\mathrm{km\,s^{-1}}$, in agreement with a galactic wind scenario. The observed symmetry of the polarized halo features in NGC 4388 excludes a compression of the halo gas by the ram pressure of the intracluster medium (ICM). The assumption of equilibrium between the halo pressure and the ICM ram pressure allows an estimate of the ICM density that is consistent with both the ICM density derived from X-ray observations and recent *Planck* Sunyaev–Zel'dovich measurements. The detection of a faint radio halo around cluster galaxies can thus be used for an estimate of ICM ram pressure.

We find an asymmetry in the Faraday rotation measure RM pat-

tern of the southern part of the northern hotspot at the end of the northern nuclear outflow. The profile of this hotspot can be interpreted as the magnetic field changing its direction along the line of sight. We suspect that this RM asymmetry could be due to the action of a precessing nuclear outflow of the northern and southern filaments with respect to the center of the galaxy. Another indication of the precession is the wiggling structure seen in the magnetic field vectors along the southern nuclear outflow.

We show that a precession model of the nuclear outflow gives similar structures in the morphology of the radio polarization filaments in the halo of NGC 4388. The precession model allows us to estimate a velocity of $1300 - 2300 \, \mathrm{km \, s^{-1}}$ and $500 - 1000 \, \mathrm{km \, s^{-1}}$ for the northern and southern parts of the nuclear outflow, respectively. We find a similar structure between the direction of the modeled precessing outflow and the observed sign of RMs. We interpret this similarity as the result of the magnetic field following the helical direction of a precessing nuclear outflow, which is an independent proof of precession as a plausible scenario in the nuclear outflow of this galaxy.

Complementary observations at S-band and X-band (VLA) and at 610 MHz (GMRT) in order to confirm and further study the new features found in the radio halo of this galaxy. A spectral index distribution analysis of the nuclear outflow in NGC 4388 suggests diffusive shock acceleration of CREs produced by the interaction with the ICM environment. Our estimates give velocities and inclination for the northern and the southern nuclear outflows that agree with the ones estimated by the precession model. The action of ram pressure probably pushes the ISM material towards the north giving rise to different velocities and hence Mach numbers in both halves of the outflow.

A poet once said, "The whole universe is in a glass of wine". We will probably never know in what sense he meant that, for poets do not write to be understood. But it is true that if we look at a glass of wine closely enough we see the entire universe. There are the things of physics: the twisting liquid which evaporates depending on the wind and weather, the reflections in the glass, and our imagination adds the atoms. The glass is a distillation of the earth's rocks, and in its composition we see the secrets of the universe's age, and the evolution of stars. What strange array of chemicals are in the wine? How did they come to be? There are the ferments, the enzymes, the substrates, and the products. There in wine is found the great generalization: all life is fermentation. Nobody can discover the chemistry of wine without discovering, as did Louis Pasteur, the cause of much disease. How vivid is the claret, pressing its existence into the consciousness that watches it! If our small minds, for some convenience, divide this glass of wine, this universe, into parts-physics, biology, geology, astronomy, psychology, and so on - remember that nature does not know it! So let us put it all back together, not forgetting ultimately what it is for. Let it give us one more final pleasure: drink it and forget it all!

Richard Feynman
The Feynman Lectures, volume I; "The Relation of Physics to Other Sciences".

Acknowledgements

Contents

List of Figures

List of Tables

Introduction

Contents

1.1 Magnetic Fields in Galaxies

Magnetic fields play an important role in galaxies (Kulsrud & Zweibel, 2008; Beck, 2016). Their contribution has a key role in many of the processes in the interstellar medium (ISM) like the propagation of cosmic rays out of the galactic disk and the decrease of angular momentum in protostellar clouds. They are also responsible of distributing the energy from supernova explosions within the ISM and for the gas dynamics in molecular clouds. They drive outflow events that transport gas from the disk of galaxies into the halo and the intergalactic medium. The evolution of a galaxy is deeply related with the physics of magnetic fields.

Radio observations of the synchrotron radiation are one of the main tools to study magnetic field in spiral galaxies. Particularly, the Effelsberg radio telescope and the Very Large Array (VLA) have been precursors in this field. The polarized radio emission shows a ordered magnetic field in almost every spiral galaxy (Wielebinski & Beck, 2005). The large scale magnetic field follows a spiral structure as seen in the galactic arms and, as shown in numerous examples (see Figure 1.1), it appears to be ordered in the interarm regions (also known as
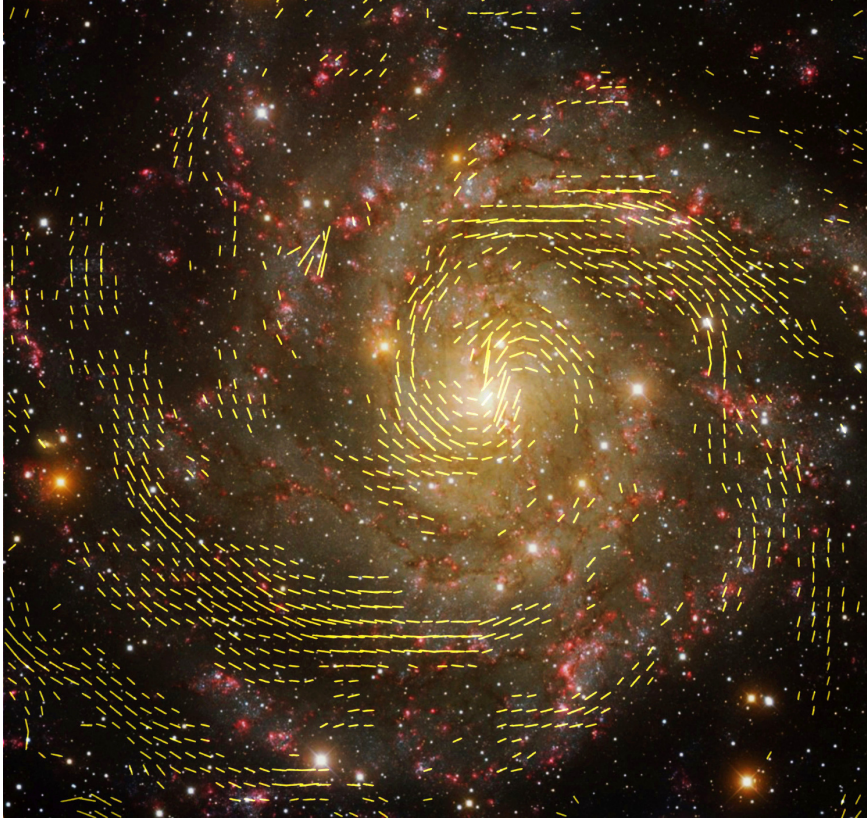
Figure 1.1: Magnetic vectors of the spiral galaxy IC 342 at $\lambda 6.2$ cm (VLA + Effelsberg) at $25''$ of resolution, overlaid on an optical image from the Kitt Peak Observatory (credit: T.A. Rector, University of Alaska Anchorage, and H. Schweiker, WIYN and NOAO/AURA/NSF) (Beck, 2015).

"magnetic arms") where the turbulence of the ISM is weaker. Within the spiral arms, the degree of polarization is small probably due to the disturbance of the ordered field by supernova shock fronts and motions of clouds. Also, in these regions the shear and compression of the ISM is stronger. The spiral density waves that are responsible for these spiral structures (Lin & Shu, 1964), may be transient and the magnetic field responds quickly to changes in the spiral structure and may affect its formation. However, these magnetic arms might remain for a long time -hundreds of Myr- in such a state of spiral structure, which were produced by matter that moved away from them (Chamandy et al., 2013). At large scales, the magnetic field strength found in galaxies is typically $10 - 15\,\mu$G and its distribution can be turbulent and disordered or coherent and ordered. The effects of magnetic fields on the formation and stability of spiral arms and the interaction between gas motions and magnetic fields are still fundamental open questions of this field.

1.2 Studying Edge-on Galaxies

Depending on the the inclination of a spiral galaxy respect to our line of sight, we are able to study different properties of their magnetic fields.

In face-on galaxies, with inclinations close to 0°, we observe the magnetic field of the galactic disc. This orientation makes these galaxies a perfect object to study spiral patterns and the role of magnetic arms to the ISM evolution. The so-called edge-on galaxies have an inclination closer to 90° and are better to study the magnetic field of galactic halos (Krause, 2009). Most edge-on galaxies show a magnetic field parallel to the galactic plane within the disc and an "X-shaped" magnetic field in the halo (Mora & Krause, 2013).

By studying edge-on galaxies, we can understand the exiting connection between the different dynamical components of a galaxy. The spectral index analysis of these gaseous halos can provide information about the CR transport from the disk into the outskirts of the galaxy. The analysis of radio polarized emission and the rotation of the polarized vector due to the Faraday effect help understanding the formation of the large scale magnetic fields in the halo and their role in the dynamics and evolution of a galaxy.

The intergalactic medium (IGM) might have been magnetized by the action of galactic outflows (Kronberg et al., 1999). When the velocity of a galactic wind overcomes the scape velocity, galactic CR and magnetic fields can reach the IGM (Heesen et al., 2009). The study of galactic wind events is of crucial interest to understand the evolution of the environment of spirals.

Open questions related to edge-on galaxies are the lagging of the halos respect to the dense gas within the disk (Swaters et al., 1997). Ballistic fountain models seem to be insufficient to explain this phenomenon (Fraternali & Binney, 2006). Also, the interaction between the ICM ram pressure and the magnetic outflows of galaxies is far from being understood.

1.3 Synchrotron Radiation

The synchrotron radiation serves as the main tool to investigate the magnetic field in galaxies. This is the emission mechanism which dominates the non-thermal emission part of the spectrum (Longair, 1994) and dominates the radio continuum spectra. This radiation is formed from the deceleration of relativistic charged particles when rotating around magnetic field lines. In the frame of galactic magnetic fields, these are found where star formation occurs due to the relation between synchrotron radiation and cosmic ray (CR) density. The charged particles involved in this radiation are mostly electrons since positrons are rare, and protons have too high mass to be efficiently accelerated. Shock

fronts by supernova explosions are responsible for the injection of charged particles into the ISM of galaxies and these particles lose their energy in form of synchrotron radiation. As observers, we only detect the synchrotron radiation when the velocity vector of the particle is within an angle of $1/\gamma$ - where γ is the Lorentz factor- of the line of sight of the observation.

The synchrotron radiation depends on the magnetic field strength that is perpendicular to the line of sight (Klein & Fletcher, 2015) and on the frequency of the observation as follows:

$$I_\nu \sim B^{1+\alpha} \cdot \nu^{-\alpha}, \tag{1.1}$$

where I is the total intensity of the synchrotron radiation, B is the magnetic field strength, ν is the observation frequency, and α is the spectral index related to the energy spectrum of the CREs (with α positive for decreasing spectrum). This means that by studying radio observations we can also infer the main properties of CREs propagation from a certain source.

1.4 Radio Polarization

The velocity of the particles determines the type of polarization that we see. It can be linear, elliptical and in rare cases, with low values of γ, partly circular. In the case of highly relativistic particles, in the limit of $\gamma \gg 1$, the components of elliptical polarization parallel to the magnetic field cancel out and the result is linear polarization. The orientation of the electric vector detected by the receivers is perpendicular to the magnetic field lines in which the CR are gyrating. The observed polarization orientation is not a true vector because its direction is ambiguous by multiples of $\pm\pi$. It is this connection which makes the synchrotron emission so important for the study of magnetic fields in galaxies.

Since the synchrotron radiation is linearly polarized, radio observations of polarized signals are useful to study the phenomena associated to the CREs interactions with magnetic fields in astronomical sources. In radio astronomy, the polarized signals are detected by receivers that are able to separate the coming signal into different components of the Stokes parameters. In the case of the Very Large Array interferometer (VLA) the receivers of every antenna have circular feeds that measure the response of a linear combination of two Stokes parameters of the polarized signal as follows:

$$I = (LL + RR)/2 \tag{1.2}$$

$$Q = (RL + LR)/2 \tag{1.3}$$

$$U = (RL - LR)/2 \tag{1.4}$$

$$V = (LL - RR)/2, \tag{1.5}$$

where I Q, U, and V are the Stokes parameters, and RR, LL, RL, and LR are circular correlations.

Assuming no depolarization effects and a magnetic field that is totally uniform, the theoretical maximum degree of linear polarization is $\sim 70\%$. In practice, radio observations of galaxies suffer of depolarization effects and the degrees of polarization are much smaller than that limit. The main depolarization mechanisms are beam depolarization, caused by the integration of polarization vectors with different orientations within the same observational beam; internal Faraday depolarization, where the intrinsic geometry of the source depolarizes the emission; and the so-called bandwidth depolarization, where the integration of the polarized signal observed cancels polarized vectors when they are rotated by Faraday rotation within the individual channels.

1.5 Rotation Measures (RM)

The rotation of the electric field vector of a linearly polarized wave when in propagates through a magnetized plasma is called "rotation measure" (RM) (Klein & Fletcher, 2015). The rotation of this vector depends on the wavelength of the observation and on the RM value in the following way:

$$\Delta\chi = RM \cdot \lambda^2, \tag{1.6}$$

where χ is the angle of rotation of the vector, RM is measured in $\mathrm{rad\,m^{-2}}$, and the wavelength λ is measured in meters. The RM is an important quantity in astronomy as it relates magnetic field strength, thermal electron density, and path length in the following way:

$$RM \cong 0.81 < n_e \cdot B_{\shortparallel} > L, \tag{1.7}$$

where n_e is the electron density, $B_{\shortparallel}$ is the component of the magnetic field parallel to the line of sight, $<>$ denotes averaging along the line of sight, and L is the path length through the magnetized plasma. As $\Delta\chi$ depends on λ^2, this quantity increases rapidly at low frequencies. Measuring the RM of a radio source provides important information about the configuration of its magnetic field. In particular, the sign of RM measured over a sufficiently large radio frequency coverage, will tell us the orientation of the field in the line of sight. Thus, negative RMs will show magnetic field that points away from the observer and positives values of RMs will show the magnetic field that points towards the observer. This makes RM analysis a powerful tool to characterize the intrinsic

properties of astrophysical magnetic fields. However, $\Delta\chi$ may not be linearly proportional to λ^2, so that RM may be a function of λ^2 (see Section 1.6).

1.6   RM synthesis

New radio telescopes improve sensitivity and gain observation speed thanks to new broad band receivers. Although polarization observations also benefit from this improvement in sensitivity, modern receivers have multiple channels, so that bandwidth depolarization is small. A problem occurs at long wavelengths and at large RMs, when Faraday rotation is large across the band, so that Q signals are transferred into U signals and vice versa, and it is not possible to average Q and U over all channels. Furthermore, several synchrotron emitting and Faraday rotation sources may be located within the telescope beam and /or the line of sight. For this reason we make use of the RM synthesis technique (Brentjens & de Bruyn, 2005; Heald, 2009, 2015). This novel technique is an extension of the work on rotation measures and Faraday dispersion done by Burn (1966) and provides a tool to treat polarization broad band observations.

We define the Faraday depth (ϕ) as:

$$\phi(r) = 0.81 \int_{there}^{here} n_e \boldsymbol{B} \, \mathrm{d}r (\mathrm{rad\,m^{-2}}), \tag{1.8}$$

where n_e is the electron density in $\mathrm{cm^{-3}}$, $\boldsymbol{B}$ the component of the magnetic field along the line of side in μG, and r is the path length in pc. This means that if the Faraday depth is positive, the magnetic field points towards the observer and vice versa. Burn (1966) defined the complex Faraday dispersion function ($F(\phi)$) through:

$$P(\lambda^2) = \int_{-\infty}^{+\infty} F(\phi) \mathrm{e}^{2i\phi\lambda^2} \mathrm{d}\phi, \tag{1.9}$$

where $P(\lambda^2)$ is the complex polarized surface brightness. This expression is very similar to a Fourier transform but as $P(\lambda^2)$ only have physical meaning when it is positive, we have to make some assumptions for its calculation in the range of $\lambda^2 < 0$ and for limited bandwidths. For this reason Brentjens & de Bruyn (2005) introduced the weight function $W(\lambda^2)$ which is nonzero at all values of λ^2 that are measured and 0 when there is no measurements. This function represents the bandwidth of the observation and can be combined with equation 1.9 to obtain the Faraday spectrum:

$$\tilde{F}(\phi) = K \int_{-\infty}^{+\infty} \tilde{P}(\lambda^2) \mathrm{e}^{-2i\phi(\lambda^2 - \lambda_0^2)} \mathrm{d}\lambda^2, \tag{1.10}$$

where K is the inverse of the weight function and $\tilde{P} = W(\lambda^2)P(\lambda^2)$. This expression was obtained through the convolution between the Faraday dispersion function and the so called RM Spread Function (RMSF), which represents the response of the instrument and gives the resolution in Faraday space:

$$R(\phi) = K \int_{-\infty}^{+\infty} W(\lambda^2)\mathrm{e}^{-2i\phi(\lambda^2 - \lambda_0^2)}\mathrm{d}\lambda^2 \tag{1.11}$$

Notice from equation 1.10 that in practice, when we apply RM synthesis, we are transforming data cubes with two coordinates axis (right ascension and declination) and a third one of frequency, to data cubes of two coordinates axis plus a third one of Faraday depth. From this cube we can obtain the different values of ϕ in all the lines of sight of our radio maps. In the Faraday space, one narrow component is formed by the presence of a Faraday screen. Broad components are caused by emissivity and rotating sources. A combination of these sources within a single line of sight can create a complex Faraday spectrum.

1.7 Magnetic Field Strength

Total and non-thermal synchrotron radio emission provide information on the total magnetic field and the ordered magnetic field components, respectively.

However, we need to make estimations about the relation between the magnetic field and the cosmic ray electrons (CREs) for determining the magnetic field strength. There is an equilibrium between total cosmic rays and magnetic fields due to their exchange of energies. Thus, we can assume equipartition between these two factor ($\varepsilon_\mathrm{B} = \varepsilon_\mathrm{CR}$) (Beck & Krause, 2005).

The revised equipartition formula for the field goes as:

$$B_\mathrm{eq} = (6\pi G(K+1)L_\nu/V)^{\frac{1}{\alpha+3}} \tag{1.12}$$

where G depends on the frequency and on the spectral index α, K is the ratio between total energy density of cosmic ray nuclei and energy of electrons (and positrons), and L_ν is the synchrotron luminosity.

The radio emissivity L_ν/V is the average of the luminosity over the volume of the source. The total radio intensity comes mainly from areas where the magnetic field is strongest. This results in a equipartition of magnetic field strength larger than the averaged magnetic field.

For obtaining a reliable value of K, we would need to make a spectral analysis over the whole energy range of all kinds of cosmic rays. However, the limited frequency bands of radio observations allow to cover only the spectrum from cosmic electrons over a small range of energy.
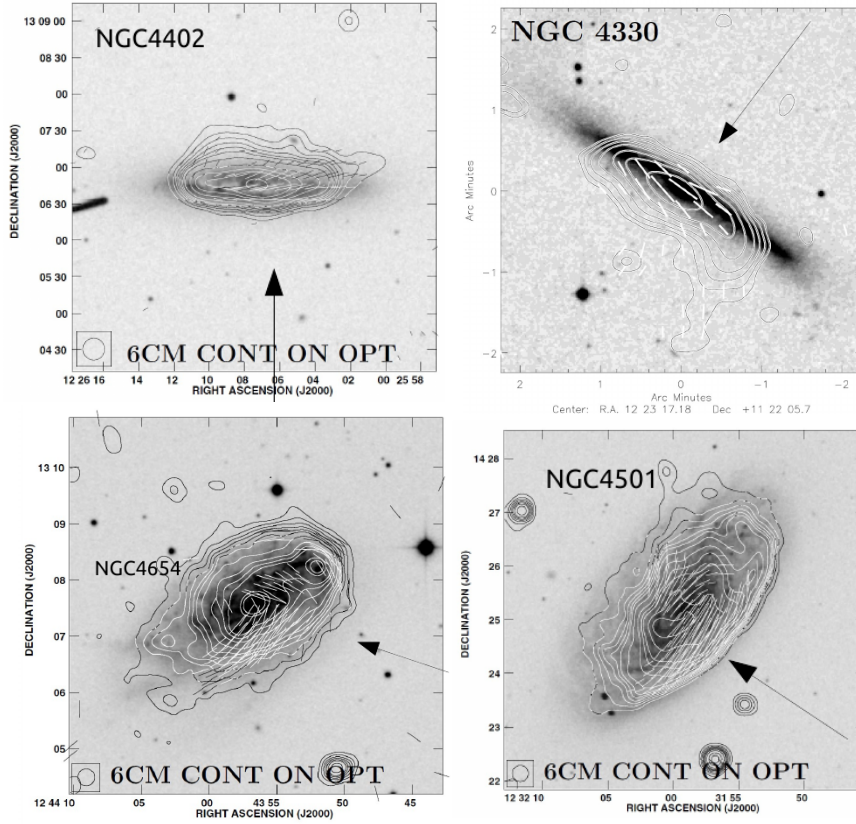
Figure 1.2: Examples of galaxies under the effects of ram pressure. These are total radio intensity contours of VLA at $6.0\,$GHz (C-band) over optical images in gray scale of various Virgo galaxies, plotted with magnetic vectors (Vollmer et al., 2013). Black arrows indicate the direction of the ram pressure action on each galaxy.

Beck & Krause (2005) solved these problems by replacing the synchrotron emissivity L_ν/V by the local synchrotron intensity over the path length through the emitting medium I_ν/l and by using $\mathbf{K}$, the ratio of proton to electron densities per particle energy interval in the energy range traced by the observed radio emission, instead of K. They propose a revised formula of the equipartition formula based on the above assumptions.

1.8 Interaction of Galaxies with the Intra Cluster Medium

The evolution of spirals in a cluster is strongly affected by the interaction with the intracluster medium (ICM). There is a strong relation between the galaxy type and the local density of a galaxy (Dressler, 1980). In general, S0 and elliptical

populations of galaxies increase while spiral populations decrease when increasing the local galaxy density. Nearby clusters of galaxies host mainly elliptical and S0 galaxies, while younger clusters contain larger blue spiral populations (Moore et al., 1996). By contrast, field galaxies that are not associated with any cluster have less morphological evolution. This means that galaxies inside a cluster must go through processes associated with the interaction with the intracluster medium (ICM) and with other galaxies that change their morphology drastically. This is the so called "galaxy harassment" and it is one of the main environmental factors that influence the evolution of galaxies in clusters.

Ram pressure is one of the main processes with which ISM gas is removed from a cluster galaxy. It is caused by the interaction between the ICM and a galaxy that travels with a certain velocity through a cluster. It is proportional to the square of the velocity of the galaxy and to the local ICM density. Ram pressure of the hot gas in a cluster might be enough to remove a large fraction of the gas in a galaxy, being able to turn spirals into S0's (Gunn & Gott, 1972). In general, when galaxies pass close to the core of rich galaxy clusters, they will have their gaseous disk truncated to $\sim 4\,\mathrm{kpc}$ loosing around ~ 80 per cent of its diffuse gas mass (Abadi et al., 1999). Galaxies that orbit in a poor gas cluster, or with inclinations towards the motion of the galaxy through the ICM, will loose less gas.

Although ram pressure is the main mechanism of galaxy stripping, viscosity, thermal conduction, and turbulence also affect the flow of ICM gas. These factors are associated with transport processes and are found to be often more determinant for gas stripping than ram pressure alone (Nulsen, 1982).

The Virgo cluster is one of the best studied cluster of galaxies. At a distance of $\sim 17\,\mathrm{Mpc}$, it is one of the closest cluster of galaxies (Yasuda et al., 1997). With a mass of $M = 1.2 \times 10^{15}\,M_\odot$ and a radius of $\sim 2.2\,\mathrm{Mpc}$ (Fouqué et al., 2001), it is also the nearest rich galaxy cluster (Chung et al., 2009) and it contains over ~ 2000 galaxies (Binggeli et al., 1985). This makes it a perfect laboratory for the study of interaction between galaxies and the ICM. Virgo is a dynamically young cluster and therefore contains a large fraction of spiral galaxies. Galactic collisions and interaction with the ICM environment give rise to a very low content of neutral hydrogen (H I) in the Virgo galaxies (Giovanelli & Haynes, 1983; Chamaraux et al., 1980). In general, Virgo spirals contain less star formation, less H I content, and are redder than field galaxies (Kennicutt, 1983).

Among all Virgo spirals there are a few edge-on galaxies for which we can see the effects of the ICM ram pressure on their halos. The effect of ram pressure on the halo of galaxies is more obvious when we observe at radio frequencies (see Figure 1.2). Radio continuum observations of a sample of Virgo galaxies affected by ram pressure show signs of interaction with the ICM: all galaxies show a truncated gas disk (Chung et al., 2009) with enhancements of ordered

field and sharp edges of the total power emission on the side of the galactic disk that faces ram pressure (black arrows in Figure 1.2) (Vollmer et al., 2013). It is unclear how galactic outflows interact with the ram pressure.
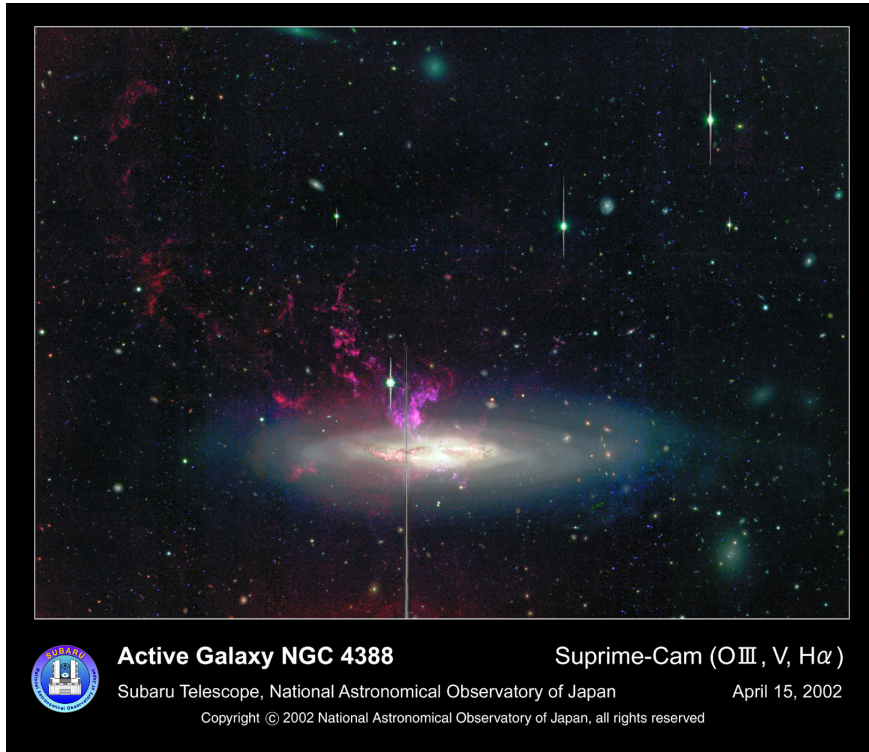
Figure 1.3: Optical image of NGC 4388 (Credits: National Astronomical Observatory of Japan, 2002).

1.9 This Project

In this thesis we study the interaction of the ICM on a very peculiar galaxy. NGC 4388 (see Figure 1.3 and Table 1.1 of the properties of the galaxy) is a Virgo galaxy that has many undergoing events at the same time. There is a clear interaction with the ICM ram pressure, which has removed a large portion of the ISM gas from its disk and created long tails and outflows of stripped gas now visible at kiloparsec scales out of its halo. This galaxy is also known for its AGN activity and its nuclear outflows, that are bright in radio emission at different scales. This is the first high resolution polarization study of these radio outflows and we want to characterize the main parameters of its intrinsic properties through a magnetic field analysis.

We intent to show how radio polarized observations can be useful when studying the relations between cluster galaxies and their environment. By tracing the magnetic field of this kind of objects we are able to study ICM properties. Specifically, new radio broad band receivers allow us to work with low values of noise never reached before for nearby galaxies. The noise reached in these new observation are on the order of $\sim 1\,\mu\mathrm{Jy/beam}$ and can reveal striking new details of

Table 1.1: NGC 4388 properties

R.A. (J2000)	$12^\mathrm{h}25^\mathrm{m}46.75^\mathrm{s}$
Decl. (J2000)	$12°39'43.5''$
Type	SA(s)b
Inclination[1]	$79°$
Position angle	$92°$
d_{25}[2]	$5.6'$
Distance	$17\,\mathrm{Mpc}$

the radio halo of a galaxy. Also, this is the first time that an RM analysis is done for this galaxy.

In Chapter 2 we present the first set of VLA observations from the CHANG-ES project. We show a first analysis of the new features found in the halo of NGC 4388 in Chapter 3. This first analysis is mainly focused on the interaction of the radio halo of this galaxy with the ICM of Virgo and the probable equilibrium between different pressure components present in the galaxy. The following Chapter 4 shows a study of the magnetic nuclear outflows discovered in this galaxy and how an scenario of precession of the accretion disk could explain the complex morphology of those outflows. With help of the precession model we estimate some of the intrinsic parameters that describe a precessing nuclear outflow. In Chapter 5 we show a campaign of new observations with the intention of confirming the new features seen in NGC 4388 and to extend our knowledge about the interaction between galactic outflows and ICM through an spectral analysis. The next Chapter 6 shows some of the possible future work to extend the study presented in this work and in the final Chapter 7 is a summary of the main results of this thesis.

Observations and Data Reduction

In this Chapter we give an overview of the procedures of the calibration of the radio datasets. Also, we show the the final radio maps of NGC 4388 for the Continuum HAlos of Nearby Galaxies - an EVLA Survey (CHANG-ES) C- and L-band datasets.

Contents

2.1 The CHANG-ES Project

The Continuum HAlos of Nearby Galaxies - an EVLA Survey (CHANG-ES) project consists of a continuum survey of 35 nearby edge-on galaxies with the VLA interferometer using different configurations at two frequencies. For all objects there are data at L-band (1.6 GHz) in B-, C- and D-configuration and at C-band (6 GHz) in C- and D-configuration using wide bandwidths in all polarization products. The broadband receivers of the VLA offer a quality never seen before reaching values of few μJy of rms in total intensity.

Many studies of galaxies have demonstrated that the continuum radio emission extends from the disk to large kilo parsec distances into the halo (Allen et al., 1978; Hummel et al., 1991). In the past, surveys of edge-on galaxies have had a limited number of galaxies and are constrained by frequency coverage and sensitivity. There was also a lack of scale variability in some of the observations. With CHANG-ES, this issue is solved since it takes advantage of the different array configurations of the VLA at different bands. By combining datasets of different array configurations we can get final images with more sensitivity and

with higher resolution. It is also the first survey providing all polarization products, in order to study the magnetic field in the halo of edge-on galaxies (Irwin et al., 2012).

One of the main goals of this survey is to address some of the key open questions of galaxy evolution:

- The origin of halos and their physical conditions.

- Lagging halos.

- The study of CR transport and galactic wind speeds.

- Magnetic fields and Faraday rotation.

- Towards consistency with gamma ray models.

- The FIR-Radio continuum correlation.

- Study of disks, nuclei, and AGNs.

In this thesis we made used of the CHANG-ES datasets of the galaxy NGC 4388. Table 2.1 shows details of the C-band observations of NGC 4388 and Tables 2.2 and 2.3 show details of the observations performed at L-band.

2.2   Calibration Process

Apart from the galaxy scans, all datasets observed as part of the CHANG-ES survey contain a flux calibrator for calibrating the flux of the rest of the sources, a phase calibrator to correct phase errors due to atmospheric effects, and a leakage calibrator to correct for the instrumental polarization. In general, the flux calibrator consists of a strong polarized radio source that is unresolved by the beam of the observation and of which we precisely know the radio flux and the polarization angle. Because we need a stable polarization angle over a broad range of frequencies, the RM value of the flux calibrator should be as close as possible to a value of $0\,\mathrm{rad\,m}{-2}$. The phase calibrator should be a radio source with a stable phase and which is located as close as possible to the target source. The leakage calibrator is a radio source that is known to be unpolarized. The data calibration was performed using the Common Astronomy Software Applications package (CASA[1]) provided by the National Radio Astronomy Observatory (NRAO[2]).

---

[1] http://casa.nrao.edu/
[2] https://casaguides.nrao.edu/

The calibration process began by carefully removing the most obvious radio frequency interferences (RFIs). In most of the cases, the observation consists of a collection of many scans that contain different CHANG-ES galaxies and calibrators. The calibrators used for the NGC 4388 datasets are: 3C286 as the flux calibrator, J1254+1141 as the phase calibrator, and J1407+2827 as the leakage calibrator. Both flux and leakage calibrators were always observed after the galaxy and the phase calibrators scans. RFIs were removed from the flux calibrator and then the flags were extended to the rest of the sources. Ringing across the frequency band might cause strong RFI since many spectral channels are affected by the RFI of a single channel. To remove this distortion, we made use of the Hanning smoothing algorithm included in the CASA package.

Once the measurements were free of the main RFI, we checked if the antenna positions were correct. VLA operators move the antennas regularly for maintenance work. As an observer, one must check the list of these corrections to make sure that these changes are included in the calibrations. The next step is to introduce a flux density model of the flux calibrator. We used the fluxes listed in (Perley & Butler, 2013). We later transfer the flux density scaling corrections to the rest of the sources in the measurement set. As the observations are taken in spectral line mode, we need to correct for the bandpass. With this step we make sure that all sub-bands (spectral windows) have a flat profile. Prior to this step, we had to make an initial phase calibration to ensure that we average the small variations in time. To correct for the complex antenna gains, we observed regularly a phase calibrator. This is done to minimize the effects of the atmosphere on the different lines of sight.

After the calibration for the total intensity terms (RR and LL) we had to set the gains for the cross terms used for Q and U images (RL and LR). For the polarization calibration, we had to manually introduce a model for the flux calibrator to define the fluxes of the cross terms (Irwin et al., 2012). After this, we correct for cross-hand delays and solve for instrumental polarization by deriving leakage solutions. Then we had to set the phase between R and L terms to correct the polarization angles. After the calibration process was done, the imaging was executed through the CLEAN task in CASA, which makes the Fourier transform of the visibilities and deconvolves the dirty beam from the image. This task is able to handle broad band data by estimating the spectrum of the radio signal Rau & Cornwell (2011). The CLEAN algorithm uses a large set of parameters that are sometimes very determinant to the final image. It is tedious to find the right set of parameters for each of the datasets and this makes the cleaning process one of the most time consuming time steps of all to obtain a final radio image. After the imaging process, we performed self-calibration in phase and amplitude. As a final step, a primary beam correction was applied to the images.

Table 2.1: Details of C-band C- and D-configuration VLA observations

Date of observations	2011 Dec 19 and 2012 Apr
Arrays	C, D
Central frequency	6.0 GHz
Bandwidth	2.0 GHz
Spectral channels	64
Channel width	2 MHz
Spectral windows	16
Primary calibrator	3C286
Secondary calibrator	J1254+1141
Leakage calibrator	J1407+2827

Table 2.2: Details of L-band D-configuration VLA observations

Date of observations	2011 Dec 21 and 30
Arrays	D
Central frequency	1.6 GHz
Bandwidth	0.5 GHz
Spectral channels	64
Channel width	2 MHz
Spectral windows	32
Primary calibrator	3C286
Secondary calibrator	J1254+1141
Leakage calibrator	J1407+2827

We applied RM synthesis to all CHANG-ES datasets to recover any polarized emission that could be affected by bandwidth depolarization effects. This is made by cleaning individual spectral windows (in case of the L-band data, they were spectral channels), applying a primary beam correction, and smoothing every image to the beam of the lowest frequency image.

2.2.1 Peeling

Some of the galaxies observed within the CHANG-ES project are part of the Virgo cluster. This is of great interest since we are able to study the interaction between edge-on galaxies and the ICM, and the effects of ram-pressure on radio halos. But observing such objects implies a very careful analysis of the data since the field of view of the Virgo cluster contains a very large number of sources that are very bright at radio frequencies. Among those radio sources, the most problematic ones are M87 (Virgo A) at the core of the cluster and M84, a double

Table 2.3: Details of L-band B- and C-configuration VLA observations

Date of observations	2012 Jul 30 and 2012 Apr 02
Arrays	B, C
Central frequency	1.6 GHz
Bandwidth	0.5 GHz
Spectral channels	64
Channel width	2 MHz
Spectral windows	32
Primary calibrator	3C286
Secondary calibrator	J1254+1141
Leakage calibrator	J1407+2827

lobe radio galaxy. M87 has a total flux density of 1.38 Jy at 1.5 GHz (Dunn et al., 2010) and has an extension of $60'' \times 30''$. M84 has a total flux density of 6.00 Jy at 1.4 GHz (Bîrzan et al., 2004) with an extension of $150'' \times 60''$.

In particular, NGC 4388 is relatively close to the cluster core ($\sim 1.3°$) where M87 is located, and it is also positioned close to M84 ($\sim 30''$). Strong radio sources that are out of the phase center of the observations are very problematic. This creates artifacts when cleaning the calibrated data that are very hard to deal with and the noise of the final images increases. In such cases, the use of a technique called "peeling" is helpful in order to decrease the effect of those artifacts and therefore, increase the signal to noise ratio of the radio maps.

Only for the case of the L-band D-configuration dataset, the use of the peeling technique was necessary since the noise after the self-calibration process was more than 5 times the theoretical noise. When peeling a radio source, it is important to make a good model of the source before subtracting it from the measurement set. This means that the peeling technique gives better results when applied to point-like sources in which the produced model is simpler than in the case of extended sources. Due to the extended radio lobes of M84, the peeling of this source is very difficult because of errors in the model image created by cleaning. M87 on the other hand, appears as a point source at the resolution of these observations so it is more suitable in this case to make a subtraction of this source using peeling.

To peel M87 we first made a clean image of this source by changing the phase center parameter in the cleaning task. Then we created a self-calibration table of this source and produced an inverted version of that table. After this, we applied the inverted calibration table to the measurement set and ran a second self-calibration process on the galaxy. In this process the point source is removed from the uv data directly. In the final image, the flux of M87 is
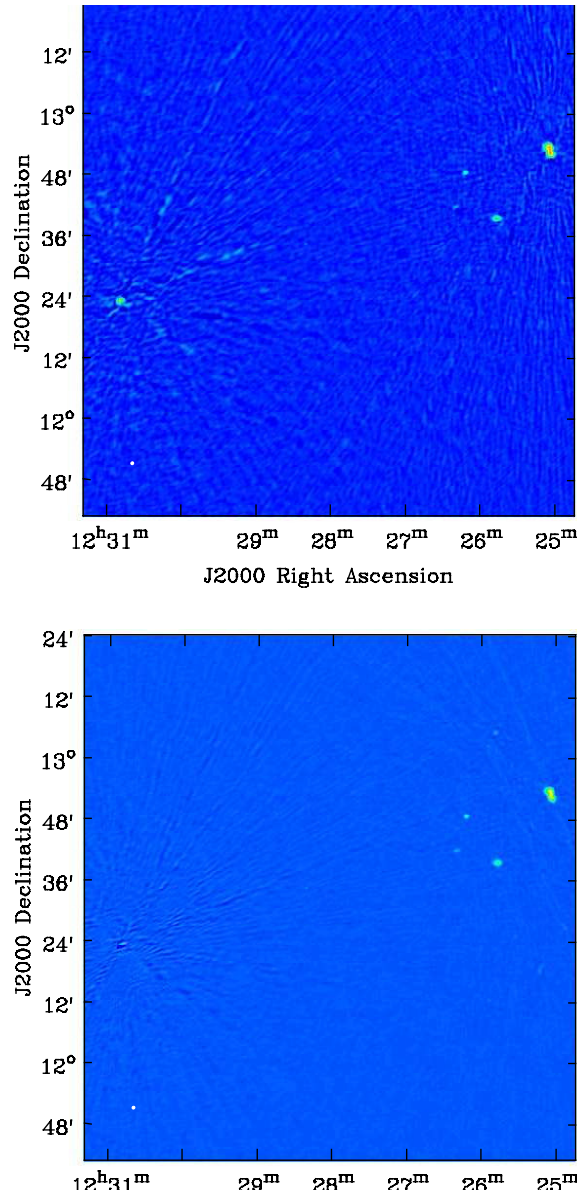
Figure 2.1: Example of an image after applying the peeling technique. These images correspond to the L-band D-configuration dataset and show the large field of these observations. The upper and bottom panels show the final radio image before and after the peeling technique was applied. M87 can be seen on the left side of the image while NGC 4388 and M84 can be seen on the right side. The noise in the upper panel is $\sim 500 \, \mathrm{mJy}$ while the bottom panel has a noise of $\sim 250 \, \mathrm{mJy}$ after the peeling technique was applied.

considerably reduced and the sidelobes are suppressed. In Figure 2.1 we show a comparison between the field of view before and after the subtraction. The noise has decreased from $\sim 500 \, \mathrm{mJy}$ to $\sim 250 \, \mathrm{mJy}$ and the emission of NGC 4388
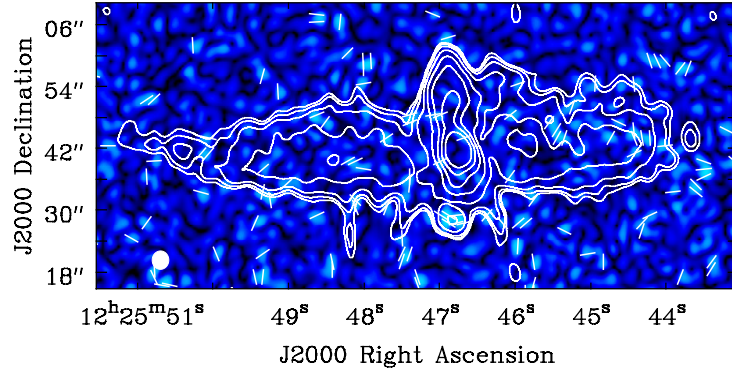
Figure 2.2: Data of NGC 4388 at 1.6 GHz (L-band) in B-configuration of the VLA. Resolution is $3.57'' \times 3.22''$. Total intensity in contours together with magnetic field vectors overlaid on a color scale of the polarized intensity. The contour levels are $(3, 4, 6, 12, 24, 48, 96, 192) \times 35\,\mu\mathrm{Jy\,beam}^{-1}$ with an rms noise of $35\,\mu\mathrm{Jy\,beam}^{-1}$. The peak of polarized intensity is $56\,\mu\mathrm{Jy\,beam}^{-1}$ being the noise of the polarized emission map $16\,\mu\mathrm{Jy\,beam}^{-1}$.

appears more extended towards the north-eastern part and towards the south-western part of the radio halo. The direction of the extensions of diffuse emission in the halo coincides with outflows seen at other frequencies, for instance Hα and X-ray (see Chapter 3). For more information about the peeling process see Pizzo & de Bruyn (2009), as well as the PhD thesis of Adebahr (2013).

2.3   Results at L-band

In Figures 2.2, 2.3, and 2.4 we present the final images obtained for the L-band datasets in B-, C-, and D-configurations, respectively. In the B- and C-configuration, the disk is detected and the nuclear radio outflow is also distinguished from the radio halo of the galaxy. The high resolution of $3.57'' \times 3.22''$ of the B-configuration map allows us to see in detail the nuclear outflow and both spiral arms. Although no polarization is detected in these datasets, there is a polarization peak of $\sim 3.5\sigma$ in the disk of the galaxy in the B-configuration image, corresponding to a total intensity blob of radio emission. This feature should be confirmed by further observations at other frequencies. The C-configuration image shows a radio halo that is more extended towards the eastern side of the galaxy and a sharp edge on the western side of the disk.
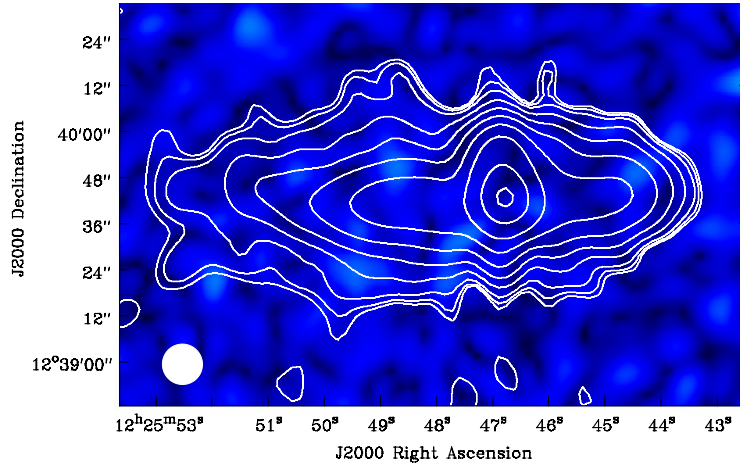
Figure 2.3: Data of NGC 4388 at 1.6 GHz (L-band) in C-configuration of the VLA. Resolution is $10.54''$ $\times$ $10.44''$.   Total intensity in contours together with magnetic field vectors overlaid on a color scale of the polarized intensity.   The contour levels are $(3, 4, 6, 12, 24, 48, 96, 200, 500, 900)$ $\times$ $50\,\mu$Jy beam^{-1} with an rms noise of $50\,\mu$Jy beam^{-1}. The noise of the polarized emission map is $30\,\mu$Jy beam^{-1}.
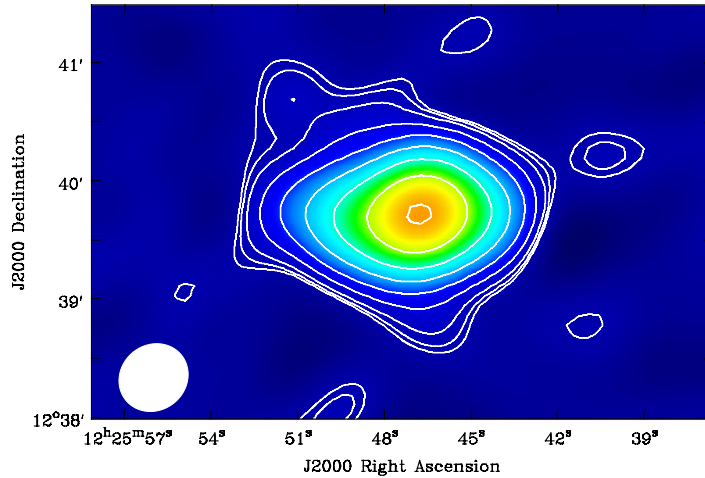
Figure 2.4: Total intensity image of NGC 4388 at 1.6 GHz (L-band) of the D-configuration data in contours and as a color scale.   Resolution is $36.33''$ $\times$ $33.05''$.   The rms noise of the map is $250\,\mu$Jy beam^{-1} and the contour levels are $(3, 4, 6, 12, 24, 48, 96, 200, 400)$ $\times$ $250\,\mu$Jy beam^{-1}.

In the case of the D-configuration final radio map, the resolution of $36.33''$ $\times$ $33.05''$ obtained is too low to differentiate the galactic disk and the nuclear outflow. However, it does show an asymmetric radio halo that extends in the north-
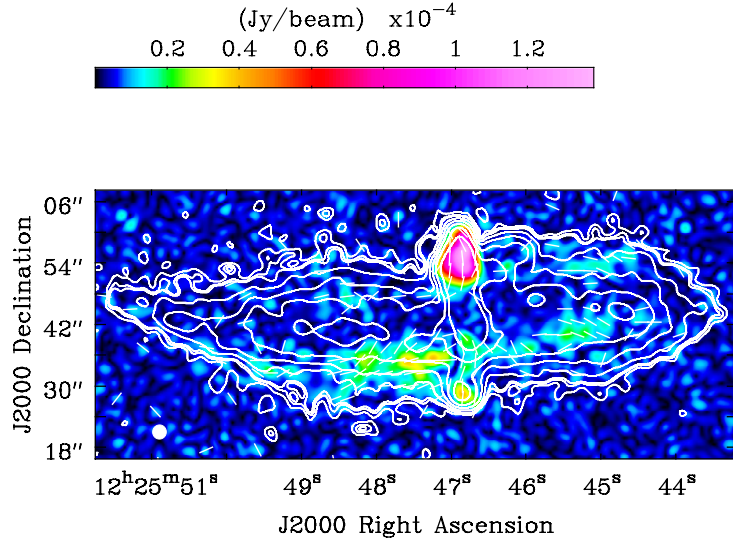
Figure 2.5: Data of NGC 4388 at 6.0 GHz (C-band) in C-configuration of the VLA. Resolution is $2.76'' \times 2.67''$. Total intensity in contours together with magnetic field vectors overlaid on a color scale of the polarized intensity. The contour levels are $(3, 5, 6, 12, 24, 48, 96, 200) \times 2.5 \, \mu\text{Jy beam}^{-1}$ with an rms noise of $2.5 \, \mu\text{Jy beam}^{-1}$. The noise of the polarized emission map is $4.5 \, \mu\text{Jy beam}^{-1}$.

eastern and south-western directions, coinciding with the areas where the Hα outflow was detected by Yoshida et al. 2002. As has already been seen in the B- and C-configuration datasets, there are no signs of polarized emission in the D-array dataset.

NGC 4388 shows no polarization in any of the datasets analyzed at L-band, although there are other radio sources in the field of view which are strongly polarized. The reason for this lack of polarization at this low frequency could be due to the fact that the noise is too high or that the source suffers from internal Faraday depolarization, which is expected to be high at this frequency. To confirm the reason for this lack of polarization detection we would need VLA polarization observations at higher frequency bands. However, we do detect polarized signal at the southern spot. The peak of polarized intensity in this spot is $56 \, \mu\text{Jy beam}^{-1}$ which is a $\sim 3.5\sigma$ detection.

2.4 Results at C-band

In Figure 2.5 we present the final image obtained for the C-band dataset in C-configuration with a robust 0 weighting. The final images of the C-band dataset

in the D-configuration was already presented by Wiegert et al. 2015. As in the case of the L-band B-configuration, the high resolution of the C-band C-configuration dataset shows many details of the disk and the nuclear outflow of NGC 4388. In total power we are able to detect both spiral arms and similarly to what we see in the L-band D-configuration dataset, we detect a radio halo of emission that is extended towards the eastern part of the galaxy and it shows sharp edges in the western side. In this case, we do detect polarized emission in the southern part of the halo, with magnetic vectors parallel to the spiral arms, and a strong area of polarized emission at the end of the northern nuclear outflow with an orientation of the magnetic field perpendicular to the galactic disk. In Chapter 3, we show the results where we give more weight to the shortest baselines during the imaging process and thus, we have more sensitivity to the extended radio emission.

Magnetic Outflows of NGC 4388

We investigate the effects of ram pressure on the ordered magnetic field of a galaxy hosting a radio halo and strong nuclear outflows. New radio images in total and polarized intensity of the edge-on Virgo galaxy NGC 4388 were obtained within the CHANG-ES EVLA project. The unprecedented noise level reached allows us to detect striking new features of the ordered magnetic field. The nuclear outflow extends far into the halo to about 5 kpc from the center and is spatially correlated with the Hα and X-ray emission. For the first time, the southern outflow is detected. Above and below both spiral arms we find extended blobs of polarized emission with an ordered field oriented perpendicular to the disk. The synchrotron lifetime of the cosmic-ray electrons (CREs) in these regions yields a mean outflow velocity of $(270 \pm 70)\,\mathrm{km\,s^{-1}}$, in agreement with a galactic wind scenario. The observed symmetry of the polarized halo features in NGC 4388 excludes a compression of the halo gas by the ram pressure of the intracluster medium (ICM). The assumption of equilibrium between the halo pressure and the ICM ram pressure yields an estimate of the ICM density that is consistent with both the ICM density derived from X-ray observations and the recent *Planck* Sunyaev–Zel'dovich measurements. The detection of a faint radio halo around cluster galaxies could thus be used for an estimate of ICM ram pressure.

Contents

3.1   Introduction

NGC 4388 is an almost edge-on SA(s)b galaxy (inclination 79°) in the Virgo
Cluster (at about 17 Mpc distance), located about 1.3° ($\approx$ 400 kpc) west from
the center of the cluster (Chung et al., 2009). The interstellar medium (ISM)
of NGC 4388 has undergone a stripping event by ram pressure, evident from the
rapid decline of star formation (190 ± 30) Myr ago (Pappalardo et al., 2010).
Like many other galaxies in cluster environments, NGC 4388 is an H I-deficient
galaxy that lost about 85% of its H I mass (Cayatte et al., 1990). The H I disk is
strongly truncated within the optical disk. An H I plume extends up to 100 kpc
out from the galaxy plane (Oosterloo & van Gorkom, 2005). The gas stripping
is possibly the result of the interaction between the galaxy and the intracluster
medium (ICM). Vollmer & Huchtmeier (2003) estimated that the galaxy passed
close to the cluster center about 120 Myr ago. A more recent model yields a
timescale of about 200 Myr (Vollmer, private communication).

Early VLA studies of this galaxy revealed a bright double source in the nu-
cleus and an outflow lobe that opens up like an hourglass and extends to about
1.5 kpc from the center (Hummel et al., 1983; Hummel & Saikia, 1991; Kukula
et al., 1995; Falcke et al., 1998). Observations with very long baseline interfer-
ometry (VLBI) revealed a radio jet with $\cong 0.5$ pc extent (Giroletti & Panessa,
2009). A circumnuclear disk of $\cong 0.1$ pc radius, oriented edge-on and almost par-
allel to the galaxy plane, was detected by its water maser emission (Kuo et al.,
2011). This indicates that the jet and the outflow emerge almost perpendicular
to the galaxy plane.

Previous VLA and Effelsberg radio continuum observations showed an ex-
tended halo and extended features out of the disk (Vollmer et al., 2010; Weż-
gowiec et al., 2012). These features may be related to the outflow event seen in
Hα and O III observations (Yoshida et al., 2002, 2004).

These deep optical spectroscopic observations are crucial to understanding
the complexity and the dynamics of the outflow of ionized gas from this galaxy.
Yoshida et al. (2002) concluded that the extended emission-line region is gas
stripped by the action of ram pressure and photoionized by the radiation from
the active galactic nucleus (AGN).

High-resolution X-ray observations with *Chandra X-ray Observatory* show
emission from the outflow, as well as from the radio jet (Iwasawa et al., 2003). On

the other hand, lower-resolution X-ray observations with *XMM-Newton* reveal the hot halo surrounding this galaxy. This halo might be shaped by the Mach cone created by the supersonic speed of the galaxy in that medium (Weżgowiec et al., 2011). The clear correlation between features in optical, radio, and X-ray frequencies suggests a common origin.

The distribution of polarized radio emission in a cluster galaxy tends to be asymmetric as a consequence of interaction with the ICM (Vollmer et al., 2007, 2013). This interaction enhances the polarized flux on the side that is facing the ram pressure due to the motion of the galactic disk in the denser environment. The H I plume detected by Oosterloo & van Gorkom (2005) represents clear evidence of interaction between the galaxy and the ICM of Virgo toward the southern part of its disk.

Little is known so far about the role of magnetic fields in the outflows of NGC 4388. Polarized radio emission is a signature of ordered magnetic fields. Previous low-resolution Effelsberg observations by Weżgowiec et al. (2012) showed a large-scale magnetic field that is inclined with respect to the disk plane. Higher-resolution VLA observations by Vollmer et al. (2010) show a complex magnetic field structure that is different in the outflow, the disk, and the halo.

Vollmer (2009) performed simulations with a sticky particle code (Vollmer et al., 2001) to quantify the outflow event that takes place in NGC 4388. They were able to reproduce with high fidelity the direction, speed, and density of the stripped gas. An important part of that study was to observe the evolution of the ram pressure of the ICM as a function of time. In that model the predicted ram pressure at the current stage of the galaxy's orbit is in a decreasing phase. They estimated a ram pressure of $1 \times 10^{-11}\,\mathrm{dyn\,cm^{-2}}$ at the present time. Within this scenario, it is expected that the action of ram pressure would transform the morphology of the gaseous galactic halo. The side of the galaxy facing ram pressure would be compressed leading to a sharp smooth edge of the radio continuum emission, with no extensions toward the outskirts of the halo.

We intend to investigate the impact of ram pressure on the magnetic field of NGC 4388 with help of the new radio polarization observations. In particular, wide-band polarimetric studies are of crucial importance for this purpose, since they reach lower limits of rms and therefore allow us to detect faint structures out in the halo of a galaxy where a weaker magnetic field is expected. In the current study we make use of improved instruments and new techniques. Higher resolution and sensitivity reveal many details of the magnetic field structure of NGC 4388 that were never observed before. New features of the galactic magnetic field in NGC 4388 extending up to 5 kpc out in the halo on both sides of the galactic disk are revealed. They are in conflict with models that include a continuous smooth ICM density profile which predict an asymmetric gas distribution within the galactic halo due to ISM compression.
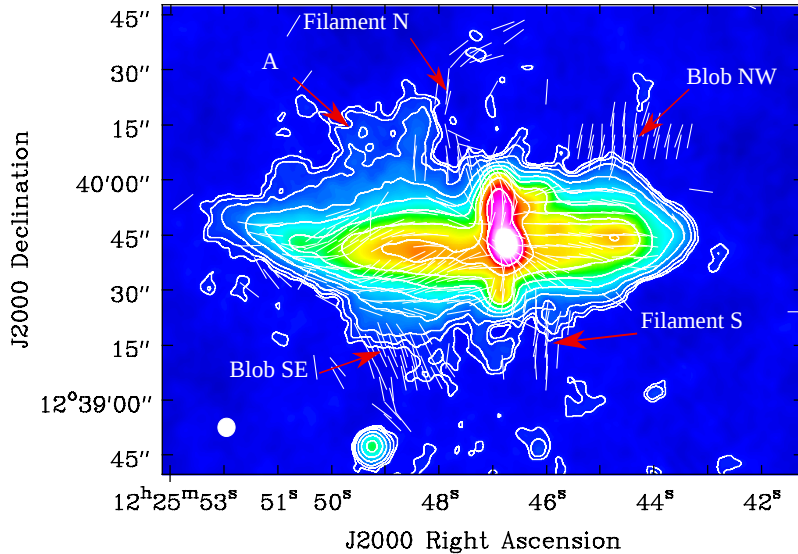
Figure 3.1: Total intensity at 6 GHz in contours plus magnetic vectors with the same vector length, corrected for Faraday rotation, with a resolution of $4.99'' \times 4.69''$ and an rms noise of $3.5\,\mu\mathrm{Jy\,beam}^{-1}$. The contour levels are $(3, 4, 6, 12, 24, 48, 96, 200, 500) \times 3.5\,\mu\mathrm{Jy\,beam}^{-1}$. A combination of the data from the C- and D- configuration of the VLA was used to make the total intensity map, whereas only C-configuration data were necessary to create the map of magnetic vectors. Both maps have been cleaned with a robust 2 weighting. The galaxy moves in the SW direction.

In Sect. 3.2 we present the observations and the data reduction. Images of radio total power and polarized emission, as well as an analysis of the magnetic field of NGC 4388, can be found in Sect. 3.3. A discussion on the different features seen in these new observations follows in Sect. 3.4. We suggest in Sect. 3.4.6 that ICM clumpiness is a possible explanation for the discrepancy between the ram pressure derived from observations and predicted by dynamical models. Sect. 3.5 contains a summary of the main points of the present study.

3.2   Observations and Data Reduction

As a part of the CHANG-ES project (Continuum Halos in Nearby Galaxies - an EVLA Survey; Irwin et al. 2012), the data set presented here was observed in C band (5–7 GHz) with the Karl G. Jansky Very Large Array (VLA) in D-configuration (Wiegert et al., 2015) and C-configuration (this paper). Details of the observations are given in Table 2.1. The large bandwidth at this frequency gives a high sensitivity never reached before in imaging of galaxies and allows
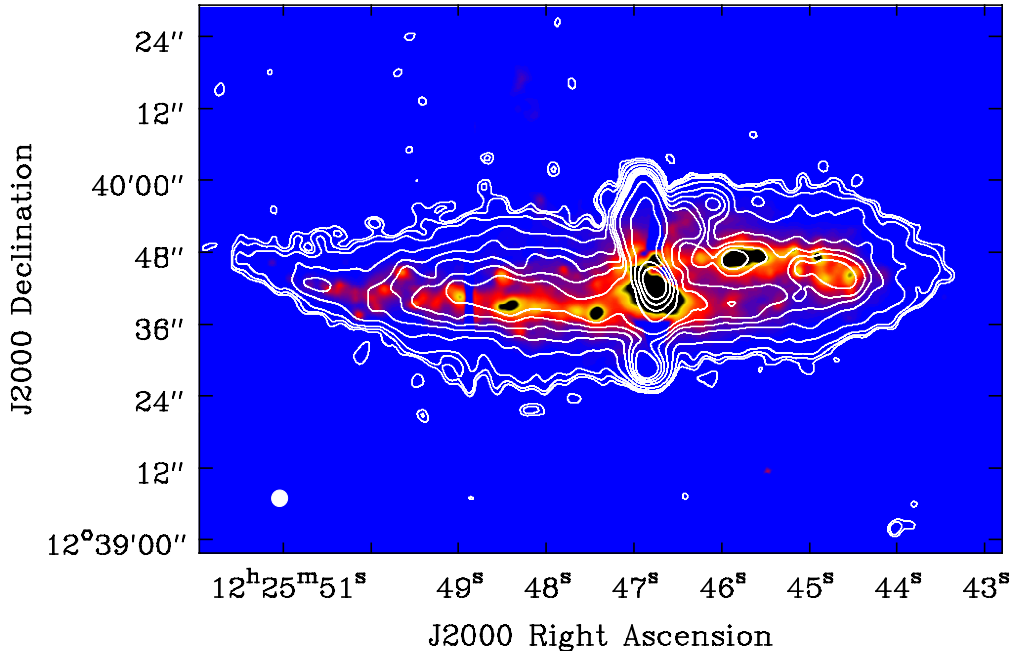
Figure 3.2: Total intensity contours plotted over the Hα map from Yoshida et al. (2002). Contours are $(3, 4, 6, 12, 24, 36, 48, 64, 128, 256, 512, 1024) \times 3.3\,\mu\mathrm{Jy\,beam}^{-1}$. This map was made with data of C-configuration with robust 0 weighting. The resolution of the radio total intensity is $2.76'' \times 2.67''$ and the rms noise is $3.3\,\mu\mathrm{Jy\,beam}^{-1}$.

the application of the RM (rotation measure) Synthesis technique (Brentjens & de Bruyn, 2005; Heald, 2009, 2015), which increases the signal-to-noise ratio of the polarized intensity images compared to previous studies.

By combining the data sets of both array configurations, we improved the uv coverage and the signal-to-noise ratio substantially.

L-band data (1–2 GHz) were also obtained as part of the CHANG-ES project, but unfortunately the data sets in this frequency band reveal large rms noise values for the NGC 4388 field. This is due to the fact that this galaxy is very close to the Virgo Cluster core in the plane of the sky ($\approx 1°$), and therefore cleaning residuals from M87, which is the central source of this cluster, increase the noise. M84, a radio galaxy that lies right at the edge of the primary beam at this frequency range, also increases the noise of these observations. In addition, no polarization was found in the L-band data sets, probably due to a stronger depolarization effect by Faraday dispersion at these frequencies and higher noise.

The data reduction was done using the CASA package. Radio frequency
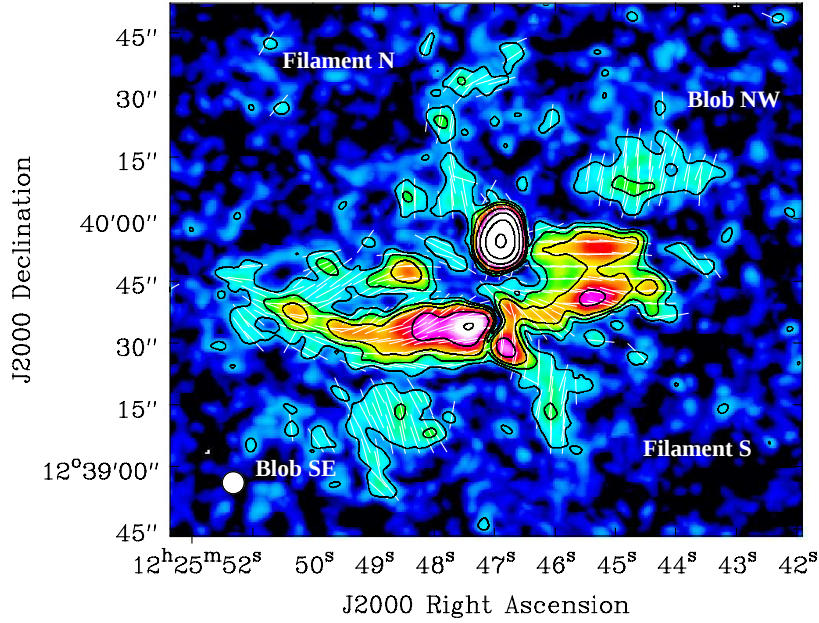
Figure 3.3: Linearly polarized intensity at 6 GHz in contours plus magnetic vectors with the same vector length, corrected for Faraday rotation, with a resolution of $5.33'' \times 5.33''$ and an rms noise of $2.3\,\mu\mathrm{Jy}\,\mathrm{beam}^{-1}$. The contour levels are $(3, 5, 8, 16, 32, 64, 128) \times 2.3\,\mu\mathrm{Jy}\,\mathrm{beam}^{-1}$. Both maps have been cleaned with a robust 2 weighting.

interference (RFI) flagging and calibration were performed for each individual channel. Imaging in Stokes I was done averaging the entire band of the data set, while imaging in Q and U was done for each of the 16 spectral windows to be combined into a cube. Natural weighting (robust $= 2$) was used during the cleaning process to ensure a higher sensitivity to extended emission. Due to the good-quality data, only two runs of self-calibration were made, one in phase and a second one in amplitude and phase.

For the first time for this galaxy, the polarization products of this data set were obtained by applying the RM Synthesis method (Brentjens & de Bruyn, 2005) to the 15 images of the usable spectral windows of 128 MHz each in Stokes Q and U. One window was removed due to low signal-to-noise ratios. Each individual spectral window image was smoothed to the resolution of the spectral window with the lowest resolution and corrected for primary beam attenuation. RM Synthesis allows us to recover most of the polarized emission that would be lost due to bandwidth depolarization while averaging Q and U intensities over the whole bandwidth. The final polarized intensity map was obtained from the Q and U values at the maximum intensity peaks in the Faraday spectrum at

each pixel in the sky plane. The bias generated in polarized intensity was then subtracted. Thanks to this technique, we reach a noise of $2.3\,\mu\mathrm{Jy\,beam}^{-1}$ at a resolution of $5.33'' \times 5.33''$ with an observation of 180 minutes on the target source (before flagging). To our knowledge, this is the lowest rms for a polarization map yet accomplished for an external galaxy.

The wavelength coverage of our observations in the given wavelength range $(\Delta\lambda^2)$ gives a resolution in Faraday space of $\delta\phi \cong 2000\,\mathrm{rad\,m}^{-2}$, which is sufficient to distinguish components in the Faraday spectrum that are separated by more than $\delta\phi/(2\mathrm{S/N})$, where S/N is the signal-to-noise ratio of the polarized intensity. As Faraday depths of a few times $10^2\,\mathrm{rad\,m}^{-2}$ are not expected from emitting regions along the line of sight through galaxies, we presume that we detect only one Faraday component at all locations.

3.3 Results

3.3.1 Images in Total and Polarized Intensity

The total intensity image obtained by combining D and C array observations from CHANG-ES shows new details in the morphology of this galaxy (see Fig. 3.1). The prominent jet-like structure just north of the nucleus is clearly detected, as in previous works (Hummel & Saikia, 1991; Kukula et al., 1995; Falcke et al., 1998), but now the disk is seen with higher resolution and sensitivity. The high surface brightness disk ($\approx 700\,\mu\mathrm{Jy\,beam}^{-1}$) of these new observations is quite symmetric, including two spiral arms (the northwestern arm being closer to us) observed in Hα (Yoshida et al. (2002, 2004); Fig.3.2). At intermediate surface brightness ($\approx 40\,\mu\mathrm{Jy\,beam}^{-1}$) we observe a pointed tail to the east (on the far east end of the galaxy) that bends toward the north. The southern part of that tail shows a sharp edge. A low surface brightness ($\approx 10\,\mu\mathrm{Jy\,beam}^{-1}$) diffuse halo is also detected. The halo is more extended and patchy in the eastern side of the galaxy. In the northeastern region (see region marked as A in Fig. 3.1) we find a similar structure between the total intensity radio emission and the Hα outflow.

Figure 3.3 shows the polarized emission of NGC 4388. The total power jet-like structure is also prominent in polarization. We detect strong polarized emission within the total power disk. The polarized intensity is strongest between the spiral arms as commonly observed in spiral galaxies (Beck & Wielebinski, 2013). The rms noise in the polarized maps is lower than in the total intensity maps; therefore, we are able to see many details in polarization that are not revealed in total power. Extended new features in polarized emission are discovered far away from the disk. Two almost vertical filaments have projected extensions of $50''$ ($\cong 4.1\,\mathrm{kpc}$) to the north and $20''$ ($\cong 1.7\,\mathrm{kpc}$) to the south. Other intriguing

features of these new observations are the two extended extraplanar regions of
polarized emission at large distances ($\approx 3.7\,\mathrm{kpc}$) northwest and southeast from
the galaxy center. In the following we will call these features the northwestern
and southeastern blobs. They reveal an ordered magnetic field and cosmic-ray
electrons (CREs) about $5\,\mathrm{kpc}$ projected distance from the plane of the galaxy.

3.3.2   The Magnetic Field in NGC 4388

Figure 3.1 shows magnetic vectors in the disk parallel to the major axis as ex-
pected for edge-on galaxies (Krause, 2011). In the southeastern part of the disk
the polarization vectors are no longer parallel to the disk and run along the
sharp edge of the total power emission. Vertical magnetic vectors can be seen in
the central region along the jet-like structure. All magnetic field vectors outside
the high and intermediate surface brightness of total power emission are almost
vertical with respect to the galactic disk.

Using the revised equipartition formula by Beck & Krause (2005), we calcu-
lated the ordered and total magnetic field strengths from the polarized and total
intensities, respectively. We assumed different path lengths and synchrotron
spectral indices for the various parts of the galaxy (see Table 3.1). The path
lengths through the emitting medium along the line of sight are taken to be the
same as the widths of the features in the sky plane. The ratio between the num-
ber densities of cosmic-ray protons and electrons in the relevant energy range of
a few GeV is assumed to be K = 100. This value may be larger in the halo due
to energy losses of CREs (see Sect. 3.4.4).

We discuss the possibility of a larger proton-to-electron ratio K than the
value of 100 assumed to derive the values in Table 3.1. The total equipartition
magnetic field B_{eq} depends on K as follows (Beck & Krause, 2005):

$$B_{\mathrm{eq}} \propto K_{\mathrm{eq}}^{1/(3+\alpha)}\,, \tag{3.1}$$

where B_{eq} and K_{eq} are the total magnetic field and the proton-to-electron ratio
from equipartition, respectively. In the absence of a cosmic-ray source in the
halo, we expect a steep spectral index ($\alpha > 1$ assuming $S_\nu \propto \nu^{-\alpha}$). Therefore,
magnetic strength depends on K_{eq} in the following way: $B \propto K_{\mathrm{eq}}^{1/4\ldots 1/5}$. Thus,
the magnetic field strength is not very sensitive to K_{eq}. An uncertainty in K_{eq}
of a factor of 2 leads to an error in B of about 20%.

We also considered different spectral index values for the various parts of the
galaxy. Large deviations in this parameter will not significantly change the final
values of the computed magnetic field strength. The resulting field strengths
in the disk are consistent with typical values for a spiral galaxy (Beck, 2001).
For the two blobs (NW and SE), B_{tot} was estimated by using a mean degree of
polarization for the NW blob of $p \cong 40\pm10\%$ derived from Fig. 3.4 and assuming
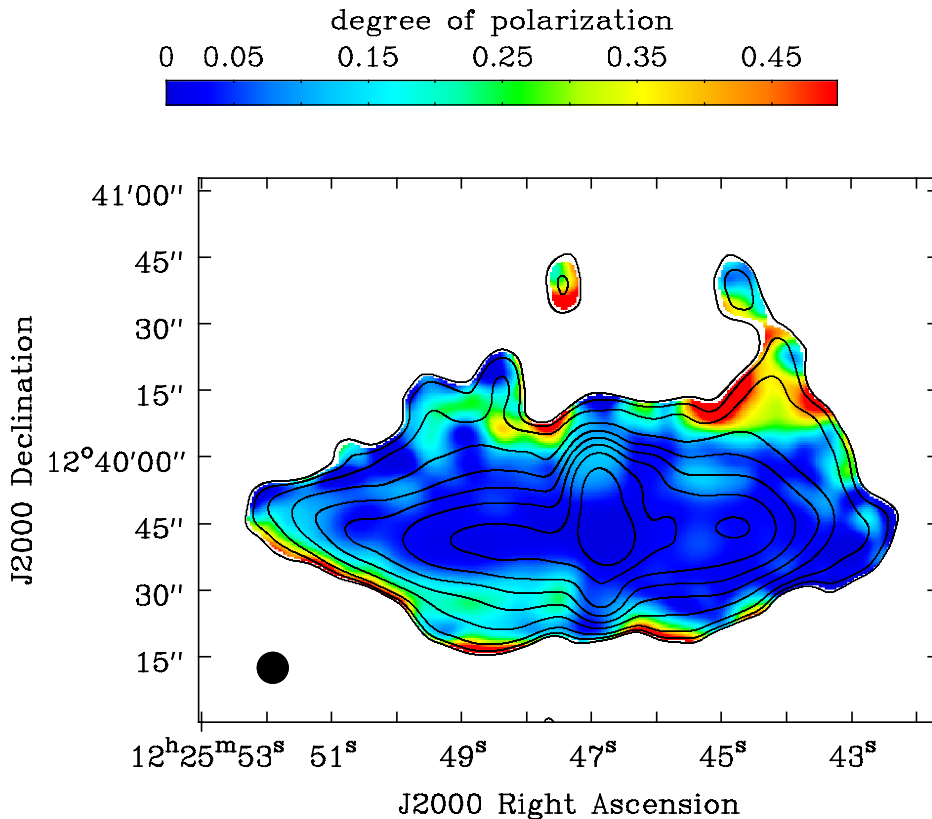
Figure 3.4: Contours of total intensity emission plotted with degree of polarization in color scale. Contours of total intensity emission are $(3, 4, 6, 12, 24, 48, 96, 200, 500) \times 6\,\mu\text{Jy beam}^{-1}$. The resolution is $7'' \times 7''$ and the rms noise is $6\,\mu\text{Jy beam}^{-1}$.

a similar degree of polarization for the SE blob. The uncertainty in p introduces an error in B_{tot} of about 10%.

The intrinsic degree of polarization p_0 in the NW blob may be larger if Faraday depolarization occurs there, possibly by $H\alpha$ clouds similar to those observed in the northeast by Yoshida et al. (2002). A turbulent field strength $B_{\text{turb}} = \sqrt{B_{\text{tot}}^2 - B_{\text{ord}}^2} \cong 8\,\mu\text{G}$, a path length of about 2300 pc (Table 3.1), and an rms thermal electron density of about $0.35\,\text{cm}^{-3}$ in $H\alpha$ clouds of about 200 pc size and 2×10^{-3} volume filling factor (Yoshida et al., 2002) lead to a dispersion in rotation measure of $\sigma_{\text{RM}} \cong 70\,\text{rad m}^{-2}$. The resulting depolarization at 6 GHz by internal Faraday dispersion (e.g. Sokoloff et al., 1998; Arshakian & Beck, 2011) is negligible ($p/p_0 \cong 0.97$). Faraday depolarization by hot gas in the halo of NGC 4388 is even less significant because its electron density is only a few times $10^{-3}\,\text{cm}^{-3}$ (Weżgowiec et al., 2011).

The strengths of the ordered field obtained from the polarization map are lower limits, since this emission only represents the component of the magnetic

Table 3.1: Equipartition field strengths in NGC 4388

Parameter	L (kpc)	α	B_{ord} (μG)	B_{tot} (μG)
Nucleus	1.0	0.8	-	67
Outflow N	1.0	0.8	23	45
Outflow S	1.0	0.8	14	30
Arm/disk SE	1, 4 [a]	0.8	16	23
Arm/disk NW	1, 4 [a]	0.8	13	21
Blob NW	2.3	1.0	9	11 [b]
Blob SE	2.3	1.0	9	11 [b]
Filament N	0.5	1.0	13	-
Filament S	0.5	1.0	13	-

[a] The path length through the spiral arm is used for polarization,
the path length through the inclined disk for total intensity.
[b] Estimated from the degree of polarization of Fig. 3.4.

vector in the plane of the sky. If the ordered field is inclined by, say, 30° with respect to the line of sight, its strength would increase by 11%.

Figure 3.5 shows the strengths of the ordered magnetic field obtained from the map of polarized intensities of NGC 4388. The strength of the ordered magnetic field within the disk is comparable to that of other spiral galaxies. The highest ordered field strengths in the extraplanar region are observed in the vertical filaments. It is notable that the magnetic field in the NW and SE blobs is weaker than in the filaments although the polarized intensities are similar. This is due to the different path lengths chosen for each region (see Sect. 3.4.2).

3.4   Discussion

3.4.1   Nuclear Outflow

We clearly detect the northern outflow extending from the center of NGC 4388 in total intensity (Fig. 3.1), while the southern counterpart is weaker. Due to the inclination of the galaxy, the emission from the northern outflow travels through the disk on the way to the observer, contrary to the emission of the southern counterpart. It is common in AGN observations to see one side of the jet brighter than the other due to Doppler beaming (Pearson & Zensus, 1987; Kellermann et al., 2007). The blue-shifted velocities of the Hα outflow in the north indicate that the northern outflow is pointing toward the observer. In those cases, the jet has an inclination toward the observer and it travels at relativistic speed. This high speed would imply a difference in size between northern and
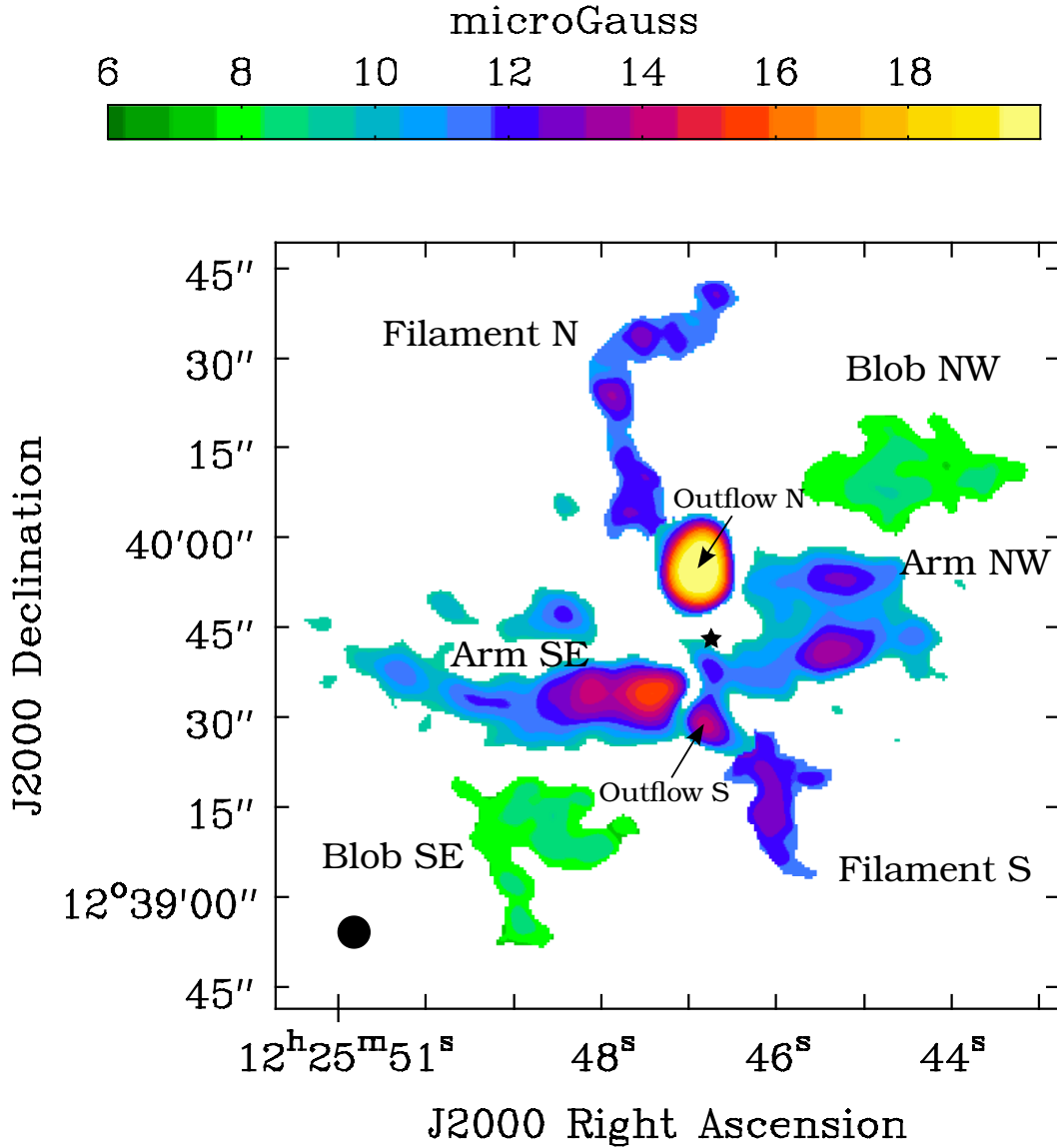
Figure 3.5: Strengths of the ordered field computed from the map of polarized intensities using the revised equipartition formula by Beck & Krause (2005). The nucleus of the galaxy is marked with a star.

southern polarization filaments due to relativistic effects. However, the AGN jet cannot remain relativistic until kiloparsec scales. A possible explanation for this configuration would imply an internal asymmetry in the ISM density close to the AGN core. This situation is supported by O III observations (Falcke et al., 1998) where there is a region of diffuse emission toward the south of the nucleus, possibly due to an interaction between the AGN outflow and the ISM gas.

In the northeastern part of the halo we can identify total power emission

associated with the outflows in Hα and O III (Yoshida et al., 2002, 2004) and X-rays (Iwasawa et al., 2003).

The northern outflow shows strongly polarized emission at the top with degrees of polarization of 12 % (Fig. 3.4), while the central part of the same structure, i.e., the nuclear region of the galaxy, reveals no detectable polarization (< 1 %). As the outflow is oriented almost perpendicular to the galaxy disk, Faraday depolarization could occur in the northern (nearby) part of the disk that is located between the outflow and the observer. Strong depolarization ($p/p_0 < 0.1$) at 6 GHz by external Faraday dispersion requires a dispersion in rotation measure of $\sigma_{\mathrm{RM}} > 400\,\mathrm{rad\,m^{-2}}$, e.g. by a diffuse ionized medium with an average thermal electron density of $> 0.03\,\mathrm{cm^{-3}}$, assuming a turbulent field strength in the disk of $B_{\mathrm{turb}} \cong 15\,\mu\mathrm{G}$ (Table 3.1), a path length through the disk of about 5000 pc, 100 pc turbulence length, and a volume filling factor of 0.5. Such electron densities are typical for the ISM of spiral galaxies (e.g. Beck, 2007). Alternatively, depolarization could occur by internal Faraday dispersion in the outflow itself. For a turbulent field strength of $B_{\mathrm{turb}} \cong 50\,\mu\mathrm{G}$ and a path length of 1000 pc, an average internal thermal electron density of $> 0.05\,\mathrm{cm^{-3}}$ is needed, which is a reasonable value.

Thanks to the new polarized emission maps, we are able to identify for the first time the counter-outflow toward the south. The main indication is the change of the orientation of the magnetic vectors from parallel to the spiral arms of the disk to being oriented along the nuclear outflow in the southern part that is connected to the center of the galaxy (Fig. 3.1). This is a clear indication of a different structure in front of the southern arm. The degree of polarization in the southern outflow is 8%, similar to the outer part of the northern outflow. Contrary to the central northern outflow, the southern outflow does show polarization, probably because the southern spiral arm does not obstruct the view of the southern outflow by the observer.

3.4.2   NGC 4388: Not an M82-like Superwind

The particular configuration of filaments and blobs seen in polarized radio continuum and Hα emission of NGC 4388 might suggest that these are different parts of the same event. Both filaments and blobs seem to form an hourglass-shaped structure. This kind of structure is typically seen in starburst galaxies. The prototypical starburst galaxy M 82 shows such an hourglass shape in Hα emission. In such a case, strong star formation in the galactic center and subsequent supernova explosions eject gas into the galactic halo within a biconical structure (Strickland et al., 2002). Hot tenuous gas expands as a superbubble into the halo pushing the extraplanar disk to larger galactic radii and compressing it. The compressed gas cools radiatively and becomes visible in many frequency
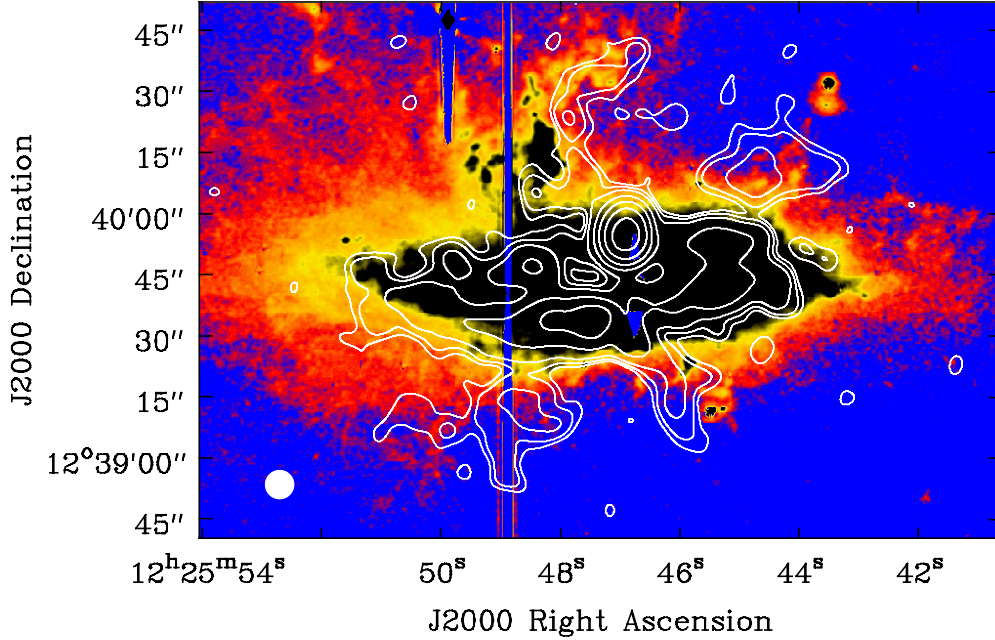
Figure 3.6: Polarized emission obtained with RM Synthesis compared to Hα observations from Yoshida et al. (2002). Contours of polarized emission are $(5, 6, 8, 16, 32, 64, 128) \times 2\,\mu\mathrm{Jy\,beam^{-1}}$. The resolution is $7'' \times 7''$ and the rms noise is $2\,\mu\mathrm{Jy\,beam^{-1}}$.

ranges, leading to the observed hourglass shape. Due to gas compression, the magnetic field is enhanced and aligned, giving rise to a large-scale ordered magnetic field observed as polarized radio continuum emission (e.g., NGC 5775; Soida et al. 2011). Within this picture the compressed shells should also be visible in X-rays (M82, Ranalli et al. 2008, NGC 253, Dahlem 1997, NGC 5775, Li et al. 2008). Observations of the diffuse X-ray emission of M82 (Strickland et al., 1997) show that the superbubble in this galaxy is partly filled with hot ($\gtrsim 10^6\,\mathrm{K}$) gas. The radio continuum emission of M82 (Adebahr et al., 2013) is co-spatial with the Hα and the X-ray emission. In NGC 5775 the diffuse X-ray emission (Li et al., 2008) fills the radio continuum superbubble on the southwestern quadrant of the disk (Soida et al., 2011). The observed correlation between X-rays, Hα, and radio continuum indicates that the hot X-ray plasma is closely linked to cooler and denser gas detected in Hα and to CREs. Such filaments extend into the galactic halo up to $\cong 10\,\mathrm{kpc}$ in the case of NGC 253 (Strickland et al., 2002).

In NGC 4388 the situation is different. The X-ray emission (see Fig. 3.7)
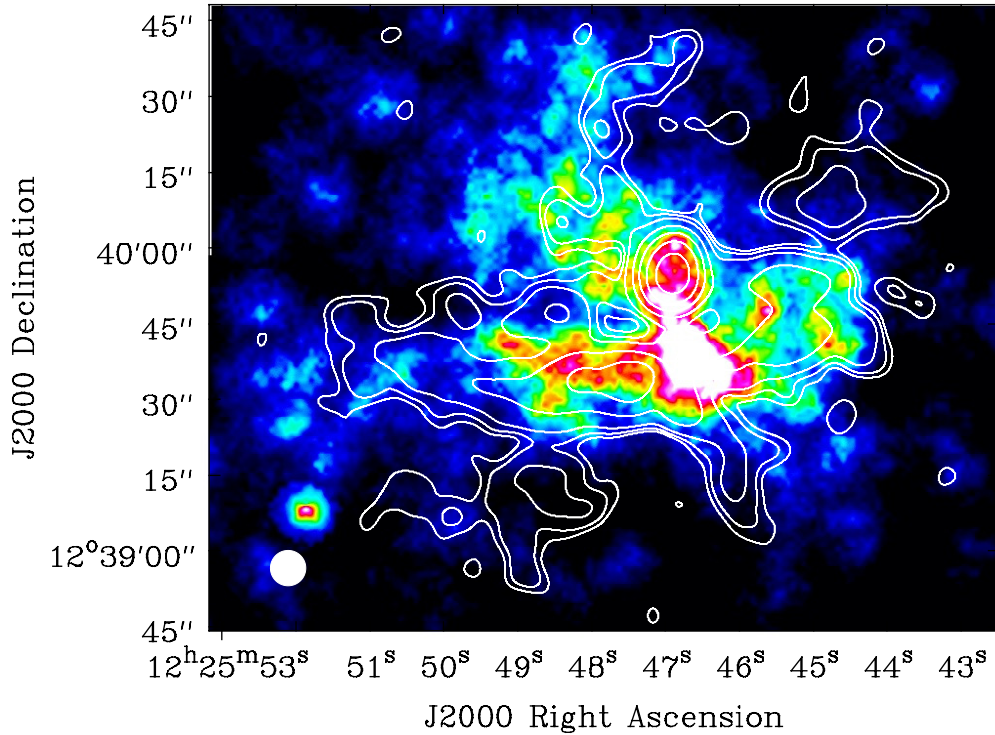
Figure 3.7: Polarized emission obtained with RM Synthesis over a CHANDRA X-ray map from Iwasawa et al. (2003). Contours of polarized emission are $(5, 6, 8, 16, 32, 64, 128) \times 2\,\mu\mathrm{Jy\,beam^{-1}}$. The resolution is $7'' \times 7''$ and the rms noise is $2\,\mu\mathrm{Jy\,beam^{-1}}$.

is not symmetric as expected from superwind models. Compared to the X-ray emission of NGC 253, we do not see enhanced extraplanar X-ray emission south of the galactic disk, in the area where the base of the bubble should be found. North of the galactic disk there is extraplanar X-ray emission. However, it is very asymmetric with almost all X-ray emission coming from the northeastern side of the galactic disk. In addition, the polarized radio continuum emission shows a filamentary structure as expected by a galactic outflow (Soida et al., 2011) only in the northeastern and the southwestern quadrants. Moreover, the observed SE and NW blobs are elongated parallel to the disk. Therefore, we conclude that the observed spatial distribution of polarized radio continuum, Hα, and X-ray emission is not consistent with a symmetric superwind scenario. In Sect. 3.4.4 we show that NGC 4388 hosts a less prominent galactic wind probably originating from the spiral arms.

3.4.3 Origin of the Polarization Filaments

We detect faint polarized emission filamentary in structure extending beyond the end of both sides of the outflow. There are striking similarities in morphology between these features and the Hα outflow (Fig. 3.6). The polarized radio continuum filaments are offset from the Hα plumes toward the minor axis of the galaxy. The projected lengths of these filamentary structures are about $50''$ (4.1 kpc) and $20''$ (1.7 kpc) for the northern and southern parts, respectively. In both cases the deconvolved half-power width is about $3.9''$ (0.3 kpc). The symmetry of the two filaments with respect to the galaxy center suggests a collimated outflow perhaps driven by a radio jet. The position angle of the filament is about $20° − 30°$, i.e. it is not perpendicular to the disk plane. The magnetic field vectors show an ordered field along both filaments (see Fig. 3.3). None of these external features are seen in total intensity due to the lower noise in the polarization maps.

The magnetic field vectors in the southern part connect the nucleus with the southern polarization filament through an apparently wiggling structure. This change of direction could be due to precession event of the AGN jet. In that case, the polarization filaments we see at kiloparsec scales are the continuation of a structure that originates in the nucleus. The fact that there is a drastic drop in polarized intensity between the nuclear outflows and the filaments could be the result of an abrupt change in the direction of the outflow giving rise to this change in polarized intensity. In that case, what we see are different parts of the same event. The origin of the filaments of NGC 4388 will be discussed in more detail in a future paper.

3.4.4 Origin of the Polarization Blobs in the Halo

We observe two blobs of polarized emission far out in the galactic halo (about 2 kpc from the disk plane), in the northwestern and southeastern regions above and below the disk, with magnetic field vectors forming an almost vertical field structure (Fig. 3.1 and 3.3). The magnetic field vectors within the disk and in the halo are perpendicular to each other, so that there are two areas between the blobs and the disk of low polarization due to geometrical depolarization within the beam. The vertical field in the blobs can be part of a large-scale halo field or field loops stretched by a strong galactic wind (see Sect. 3.4.6). These polarized blobs remain undetected at other frequencies, e.g., optical, Hα, or X-rays. However, some of the channel maps of the H I cubes from Chung et al. (2009) show structures that extend from the outskirts of the western part of the H I disk in the northeastern direction, coincident with the NW blob, indicating a possible relation to the blobs detected in polarization. We interpret this as a galactic outflow from the spiral arms. The fact that the polarized blobs are

detected close to both spiral arms in projection ($\approx 15''$) may indicate that they are related to the disk. Furthermore, there is X-ray (see Fig. 3.7), polarized, and total power emission extending $\approx 10''$ south of the southeastern spiral arm and north of the northwestern spiral arm. If so, possibly the CREs are transported by the galactic wind from the spiral arm. In this case, we estimate the speed of the galactic wind using CREs' synchrotron lifetime (e.g. Beck & Wielebinski, 2013):

$$t_{\text{syn}} \cong 1.06 \times 10^9 \, \text{yr} \left(\frac{B}{\mu\text{G}} \right)^{-\frac{3}{2}} \left(\frac{\nu}{\text{GHz}} \right)^{-\frac{1}{2}} \cong (12 \pm 3)\,\text{Myr} \qquad (3.2)$$

where $B \cong 11\,\mu\text{G}$ is the total magnetic field (Table 3.1) with an estimated error of about $2\,\mu\text{G}$, and $\nu \cong 6.0\,\text{GHz}$ is the central observation frequency. The distance between the spiral arm and the outer edge of the blobs (at the level of 5σ) is about $35'' \cong 2.9\,\text{kpc}$ for the NW blob and about $45'' \cong 3.7\,\text{kpc}$ for the SE blob. To reach this height, CREs have to travel with an average velocity of $v \cong (270 \pm 70)\,\text{km}\,\text{s}^{-1}$, which is typical for the speed of galactic winds (e.g. Heesen et al., 2009; Arribas et al., 2014). The true speed in the blob depends on the velocity profile of the outflow and could be several times larger, at least by a factor of two for constant acceleration.

The velocity of about $270\,\text{km}\,\text{s}^{-1}$ refers to the component of the galactic wind in the sky plane. With a disk inclination of $79°$ and assuming an outflow velocity vertical to the disk plane, we can estimate the component parallel to the line of sight of that vector and compare it to the observed radial velocities in Hα. We estimate the radial velocity of the outflow to be $\approx 60\,\text{km}\,\text{s}^{-1}$, which is close to the value observed in Hα (Veilleux et al., 1999). Although there is no stringent reason for the same velocity of the hot (or CREs) and the Hα-emitting cool gas flows, it is remarkable that these two components have similar velocities.

The magnetic field computed by the equipartition formula ($11\,\mu\text{G}$) could be underestimated. The energy spectrum of CREs propagating into the halo is steepened by energy losses and hence is not proportional to the proton spectrum, i.e. the proton-to-electron ratio K is significantly larger than 100 as assumed in Sect. 3.3.2 (see discussion in Beck & Krause 2005). In this case we would get a shorter synchrotron lifetime and therefore a larger velocity of the outflow. A better estimate of the outflow speed needs knowledge of the synchrotron spectral index as a function of height above the plane, which cannot be obtained with the present data.

It is surprising that there is no counterpart of both blobs on the opposite sides of the disk in any other wavelength. The two blobs might be due to an earlier AGN-related outflow, because AGNs can turn off and on, as well as change direction. However, the age of a previous outflow would be much beyond the syn-
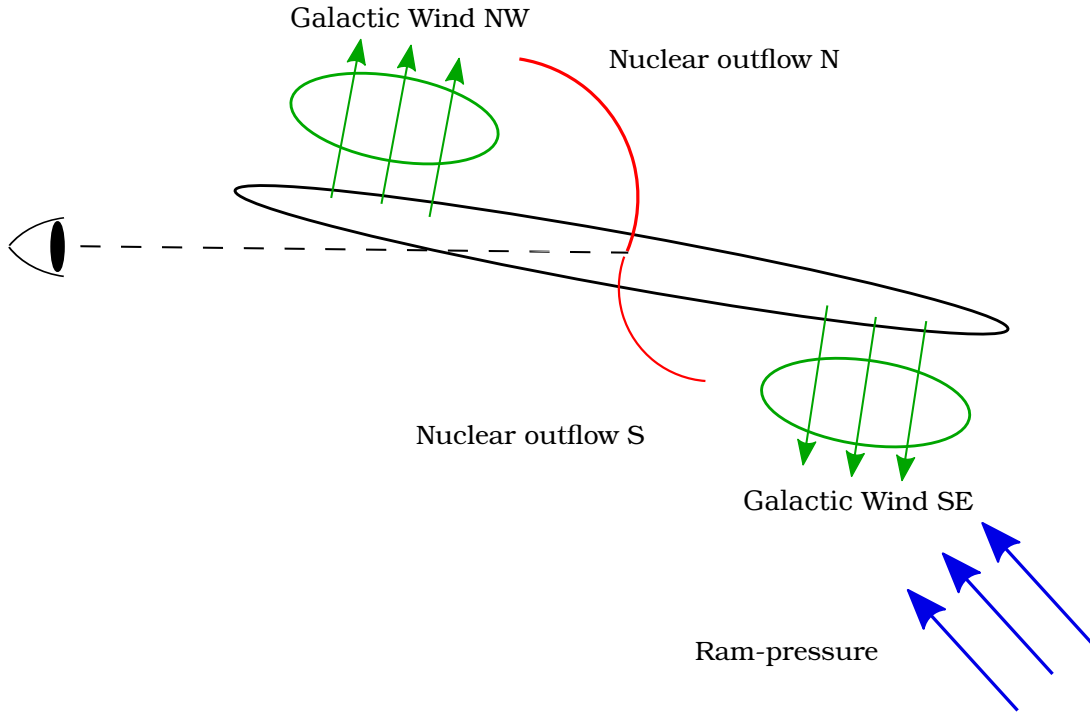
Figure 3.8: Sketch showing how the galactic winds are placed respect to the observer.

chrotron lifetime (see above). In the case of a continuous galactic wind expanding from the disk, one would expect that the outflow of particles and magnetic field is equally strong on both sides of the spiral arm. The asymmetric distribution suggests that the outflow is not homogeneous, but emerges from individual star-forming complexes that are located not exactly in the disk plane. The non-detection of the NE counterpart, on the other hand, could be caused by intrinsic depolarization due to the overlapping with the material coming from the nuclear outflow in that area.

We conclude that NGC 4388 hosts a collimated nuclear outflow and a galactic wind originating mainly from the spiral arms. Figure 3.8 is a diagram of the galaxy that shows how the winds would be orientated respect to us and respect to the ram pressure.

3.4.5 Halo Pressure

The halo pressure can have several components: thermal gas pressure, magnetic pressure, cosmic-ray pressure, and ram pressure from the galactic outflow. The thermal pressure of the hot gas of $P_{\text{th}} = nkT \cong (3 \pm 2) \times 10^{-12} \, \text{dyn} \, \text{cm}^{-2}$ is estimated using a temperature of $kT = (0.5 \pm 0.3) \, \text{keV}$ and a density of

$n \cong (4 \pm 2) \times 10^{-3}\,\mathrm{cm}^{-3}$ from Table 3 of Weżgowiec et al. (2011), interpolated between disk and tail, assuming a volume filling factor of 0.5. With an expansion velocity of $(270 \pm 70)\,\mathrm{km\,s}^{-1}$, the ram pressure of the galactic wind is $P_{\mathrm{wrp}} = 0.61\,n\,\mathrm{m_H\,v^2} \cong (3 \pm 2) \times 10^{-12}\,\mathrm{dyn\,cm}^{-2}$. With an equipartition magnetic field strength of $B \cong (11 \pm 2)\,\mu\mathrm{G}$ the magnetic pressure[1] is $P_B \cong B^2/(8\pi) \cong (5 \pm 2) \times 10^{-12}\,\mathrm{dyn\,cm}^{-2}$. Thus, there is approximate equipartition between the different pressure components (except for the cosmic-ray pressure, which is one-third of the magnetic pressure in case of energy equipartition). If the pressure components can be simply added, the total pressure is about $1.3 \times 10^{-11}\,\mathrm{dyn\,cm}^{-2}$. If, however, the pressure components are not co-spatial or some of the pressure fluctuations are anticorrelated, they should not be added to a total pressure value. Hence, the pressure in the halo is in the range of $P_{\mathrm{halo}} \cong 3 - 13 \times 10^{-12}\,\mathrm{dyn\,cm}^{-2}$.

The equipartition between the ram pressure of the outflow and the thermal pressure can be understood by the interplay between shocks and the ambient halo gas, which keeps the outflow velocity close to the sound speed of the hot halo gas.

A large-scale magnetic field may exist in the entire halo of NGC 4388 (a magnetosphere), but is observable only in regions into which a sufficiently large number of CREs are supplied from the disk by an outflow. Evidence for a large-scale regular field in the halo has to come from measurements of Faraday depth at lower frequencies with good resolution in Faraday space, i.e. a wide coverage in λ^2 space, which is not the case for the present observations centered at 6 GHz. Polarization observations in L band (centered at 1.5 GHz) are strongly affected by Faraday depolarization; hence, VLA S band (centered at 3 GHz) seems more promising. A lack of Faraday rotation around 3 GHz would support the idea of stretched field loops.

3.4.6 ICM Ram Pressure

In the first part of this subsection the ICM ram pressure is estimated via the H I stripping radius, the thermal pressure of the resisting ISM, and via a detailed comparison between observations and dynamical simulations. Magnetic pressure may help to resist ICM ram pressure. Its importance is investigated in the second part of this subsection. As a consistency check, the lower limit of the ICM ram pressure can be estimated via ionized high-velocity filaments that are accelerated by ram pressure. All ram pressure estimates yield values in excess of the pressure in the galactic halo. We suggest that the observed ICM clumpiness can account for this discrepancy, i.e. the galaxy is moving a portion of the clumpy ICM where

---

[1]The magnetic vectors in the blobs show a magnetic field that is oriented along the wind, and therefore the magnetic pressure term is smaller in this direction.

the local density is several times lower than the value predicted by a continuous smooth ICM distribution.

3.4.6.1 Ram Pressure Estimates

NGC 4388 is moving to the southwest. Therefore, we expect ram pressure compression in the southern part of the galactic disk. Vollmer (2009) described a scenario where the peak of ram pressure for this galaxy has already passed but in which the galaxy is still being affected in a considerable way by the ICM. The peak of the ram pressure in NGC 4388 occurred 190 ± 30 Myr ago (Pappalardo et al., 2010), having $P_{\max} \approx 5 \times 10^{-11}$ dyn cm^{-2} (Vollmer & Huchtmeier, 2003). At this time step the absolute velocity with respect to the cluster core is estimated to be $v \approx 2000$ km s^{-1} and the maximum ICM density $n_{\mathrm{ICM}} \approx 1 \times 10^{-3}$ cm^{-3} (Vollmer & Huchtmeier 2003 erroneously gave a maximum pressure three times higher than the actual value). The model predicts that the galaxy is now affected by a ram pressure of 1/5 of the peak ram pressure that occurred in the past. This means that at the present day this value would be $P \approx 1 \times 10^{-11}$ dyn cm^{-2}. Roediger et al. (2006) performed high-resolution 3D hydrodynamical simulations, using different parameters of densities and velocities, to reproduce the stripped gas as a result of the interaction between a massive galaxy and the ICM. In this study, the authors were also able to reproduce outflows of about 100 kpc extension. From all the scenarios considered, they concluded that the most similar one to the case of NGC 4388 can be described by a ram pressure of a few times 10^{-11} dyn cm^{-2}. However, improved hydrodynamical models by Roediger & Brüggen (2008) could not explain the shape of the gas tails of NGC 4388, possibly because the ICM is inhomogeneous or the outflow influences the interaction between the galaxy and the ICM. All these ram pressure estimates are based on the assumption that the spatial distribution of the ICM is continuous and smooth.

As a consistency check we apply the method of Vikhlinin et al. (2001) to calculate the ICM density. The ratio between the thermal pressure at the stagnation point P_0 and the thermal pressure of the freely streaming ICM P_{ICM} is a function of the galaxy's Mach number $\mathcal{M}$:

$$\frac{P_0}{P_{\mathrm{ICM}}} = \left(\frac{\gamma+1}{2}\right)^{(\gamma+1)/(\gamma-1)} \mathcal{M}^2 \left[\gamma - \frac{\gamma-1}{2\mathcal{M}^2}\right]^{-1/(\gamma-1)}, \tag{3.3}$$

where $\gamma = 5/3$ is the adiabatic index of the monoatomic gas. With an ICM temperature of 2.2 keV (Böhringer et al., 1994) the ICM sound speed is approximately $c_{\mathrm{ICM}} \cong 750$ km s^{-1}. We assume a galaxy velocity within the Virgo Cluster of $v_{\mathrm{gal}} \cong 1700$ km s^{-1}. The Mach number thus is $\mathcal{M} \cong 2.3$, leading to a pressure ratio of $P_0/P_{\mathrm{ICM}} \cong 8$. Assuming equilibrium between the thermal pressure of the hot gas halo of the galaxy and the ICM gas at the stagnation point, we can

replace P_0 by the halo pressure. With the thermal pressure of the halo P_{th} from Sect. 3.4.5, we obtain an ICM thermal pressure of $P_{ICM} \cong 4 \times 10^{-13}$ dyn cm^2 and an ICM density of $n_{ICM} \cong 1 \times 10^{-4}$ cm^{-3}. This agrees with the density derived from X-rays (Urban et al., 2011) and from the Sunyaev–Zel'dovich (SZ) signal measured by *Planck* (Planck Collaboration et al., 2015), while the dynamical model yields an ICM density of $n_{ICM}^{model} \cong 3 \times 10^{-4}$ cm^{-3}.

The model density thus seems to be overestimated by a factor of about 3. However, magnetic fields are not taken into account in the ICM pressure estimate of Eq. 3.3. Including magnetic fields will increase the estimated ICM ram pressure and thus the estimated ICM density. In Sect. 3.4.6.4 we show that ICM clumping might also mitigate the discrepancy between the two ICM pressure estimates.

Radio continuum observations of other Virgo galaxies affected by ram pressure such as NGC 4402 or NGC 4501 also show signs of interaction with the ICM: both galaxies show a truncated gas disk (Chung et al., 2009) with enhancements of polarization and sharp edges of the total power emission on one side of the galactic disk (Vollmer et al., 2007, 2010) (see Section 1.8). Vollmer et al. (2008) estimated a ram pressure of $P \approx 8.2 \times 10^{-12}$ dyn cm^{-2} for NGC 4501. For NGC 4402 we can estimate an upper limit of ram pressure by assuming that the western H I tail is pushed to higher galactic latitudes. According to Gunn & Gott (1972), the gravitational restoring force balances ram pressure: $P_{ram} = \Sigma v_{rot}^2 / R$. With a rotation velocity of $v_{rot} \cong 150$ km s^{-1}, a gas surface density of $\Sigma \cong 10 \, M_\odot$ pc^{-2}, and an H I radius of $R_{H I} \cong 7.7$ kpc the ram pressure of NGC 4402 is $P_{ram} \cong 3.2 \times 10^{-11}$ dyn cm^{-2}. If the H I tail is ram pressure stripped gas that now falls back to the galactic disk, the actual ram pressure would be a factor of a few lower than our estimate.

The estimated ram pressure of NGC 4388 is somewhat smaller than that of NGC 4402 and similar to that of NGC 4501. Since these galaxies show sharp edges of the radio continuum distribution and polarized ridges on one side of the galactic disk, we would expect to see the same phenomenon in NGC 4388.

3.4.6.2   Magnetic Pressure

In contrast to NGC 4402 or NGC 4501, the radio halo of NGC 4388 does not show a sharp southern edge. In addition, the polarized southwestern blob clearly belongs to the radio halo and thus implies that it is not compressed by ram pressure. The southern filament with a stronger magnetic field seems also unaffected by ram pressure. As observed in NGC 4569 (Chyży et al., 2006), the pressure of a galactic wind superbubble of NGC 4388 (Sect. 3.4.5) may resist ram pressure.

The magnetic pressure of a strong magnetic field may prevent ram pressure from removing the magnetic features seen in the halo. For that reason we estimate the magnetic field needed to balance the model ram pressure of

$P_{\rm ram} \approx 1 \times 10^{-11}\,{\rm dyn\,cm^{-2}}$. Setting this ram pressure equal to the magnetic energy density, a total magnetic field of about $16\,\mu$G is obtained. The value obtained from our observations in the southern blob is $(11 \pm 2)\,\mu$G (Table 3.1), smaller than what is needed to balance ram pressure, so that we would not expect any extensions of the magnetic field toward the southern halo.

We also consider the possibility that energy equipartition between total cosmic rays and total magnetic fields is not valid in the halo, e.g. because the magnetic field in the expanding wind flow is highly ordered. A close coupling of the cosmic rays to the field needs scattering at field irregularities, which may be less efficient in the halo. As a result, the cosmic rays may stream with respect to the field with a velocity higher than the Alfvén speed.

A field strength resisting the ram pressure of the model by Vollmer (2009) would mean that the magnetic energy density has to be larger than the equipartition value by at least a factor of $(16\,\mu{\rm G}/11\,\mu{\rm G})^2 \cong 2$. To provide the same synchrotron intensity as in the equipartition case, the energy density of the total cosmic rays has to be lower by a factor of $2^{-(1+\alpha)} \approx 0.25$ (for a synchrotron spectral index $\alpha \cong 1$). The corresponding ratio between the magnetic and cosmic-ray energy densities is $\gtrapprox 2^{(2+\alpha)} \approx 8$, which is an extreme deviation from equipartition, causing dynamical effects that lead to recovery of equilibrium.

Another argument against a super-equipartition field of $16\,\mu$G field in the halo comes from the synchrotron lifetime of CREs that would decrease to about $7\,$Myr. An unrealistically high average outflow speed of $500\,{\rm km\,s^{-1}}$ would be needed to reach the height of the blobs above the disk plane.

We conclude that the estimates of the field strengths in Table 3.1 are realistic. Either the ram pressure cannot be balanced by the magnetic pressure alone, or the modeled ram pressure is overestimated.

3.4.6.3 Ionized High-velocity Filaments

In the following, we will estimate a lower limit for the ram pressure needed to accelerate clumps of ionized gas observed by Yoshida et al. (2004). The "West High Velocity Filaments" contain several subclumps that are located east of the galactic disk outside the faint Hα halo. The radial velocities of the clumps in the filaments are between -250 and $-360\,{\rm km\,s^{-1}}$ with respect to the systemic velocity of NGC 4388. The radial components of the rotation velocity in these regions have positive values. Since the galaxy is leaving the cluster, the ionized clumps are decelerated by ram pressure of the ICM to negative velocities. The acceleration of a gas clump is given by $a = P_{\rm ram}/\Sigma$, where Σ is the column density of the clump. The acceleration is approximately $a = \Delta v/\Delta t = (\Delta v)^2/L$, where L is the distance over which the clump is accelerated. We assume $\Delta v \geq$

$350\,\mathrm{km\,s^{-1}}$ and $L \cong 5\,\mathrm{kpc}$. For the column density we take the mean gas density[2] of $n_{\mathrm{clump}} \cong 0.04\,\mathrm{cm^{-3}}$ and a size of $s = 100\,\mathrm{pc}$ given by Yoshida et al. (2002). In this way we estimate the minimum ram pressure to accelerate the ionized clouds to the observed velocities to be $P_{\mathrm{low}} \geq \rho\, s (\Delta v)^2 / L \cong 1.6 \times 10^{-12}\,\mathrm{dyn\,cm^{-2}}$, a factor of 2 lower than the individual halo pressure terms estimated in Sect. 3.4.5. This lower limit is consistent with ram pressure being equal to or somewhat lower than the halo pressure due to the galactic wind.

3.4.6.4   ICM Clumpiness

From the previous sections, there are indications that the ICM ram pressure from the numerical models (Vollmer 2009; Roediger et al. 2006) may be overestimated by a factor of several at this cluster radius.

X-ray spectroscopy of the Virgo Cluster (Urban et al., 2011) indicates a drastic drop of temperature and metallicity beyond a radius of $r \cong 450\,\mathrm{kpc}$ from the cluster center. A natural explanation for this decrease is clumping of the ICM that sets in at that radius. Based on the detailed comparison between observations and dynamical models, Vollmer (2009) determined the 3D distance of the Virgo spiral galaxies. With respect to the cluster center, the 3D distance of NGC 4388 is estimated to be $420\,\mathrm{kpc}$. This distance compares well with the distance where the ICM becomes clumpy. We note that due to clumpiness, the actual ICM ram pressure acting on NGC 4388 might be up to a factor of two lower than what is expected from a model including a smooth continuous ICM.

The *Planck* measurements of the Virgo Cluster SZ effect (Planck Collaboration et al., 2015) show that radially averaged ICM clumping cannot be strong at the cluster distance of $420\,\mathrm{kpc}$. Based on numerical simulations, typical radially averaged clumping factors $C = <n_e^2> / <n_e>^2$ of unrelaxed clusters are $C = 1.5 - 2$ (Zhuravleva et al., 2013). Locally, the density can be enhanced by a factor of $3 - 10$. However, locations with densities exceeding three times the mean density are extremely rare (see Figure 3 of Zhuravleva et al. 2013).

With a galaxy velocity of $1700\,\mathrm{km\,s^{-1}}$ and an ICM density of $n_{\mathrm{ICM}} \cong 1 \times 10^{-4}\,\mathrm{cm^{-3}}$ (Urban et al., 2011), the ICM ram pressure is $P_{\mathrm{ram}} \cong 3 \times 10^{-12}\,\mathrm{dyn\,cm^{-2}}$, which is consistent with the thermal halo pressure (Sect. 3.4.5). If the magnetic and CR pressures are co-spatial with the thermal halo pressure, the actual ICM ram pressure can exceed $3 \times 10^{-12}\,\mathrm{dyn\,cm^{-2}}$. On the other hand, the dynamical model predicts an ICM ram pressure of $1 \times 10^{-11}\,\mathrm{dyn\,cm^{-2}}$. Thus, ICM clumping cannot be excluded, and the actual ICM ram pressure acting on NGC 4388 might well be a few times higher than the radially averaged ICM density estimated from X-ray and SZ observations.

---

[2]This implies a volume filling factor of 10^{-3}

Current dynamical simulations of ram pressure stripping events assume a continuous ICM distribution (Vollmer et al. 2001, Roediger et al. 2006, Tonnesen & Bryan 2009). The influence of a clumpy ICM on these simulations depends on the stage of the interaction: a clumpy ICM distribution significantly affects only the beginning and the end of the simulations when the distance to the Virgo Cluster center of the galaxy exceeds $\approx 500\,\mathrm{kpc}$. If the galaxy is observed close to or after peak ram pressure, the changes of the simulation results with respect to a continuous ICM distribution are expected to be minor. However, if the galaxy is observed at the beginning of the ram pressure stripping event or more than $200\,\mathrm{Myr}$ after peak ram pressure, the clumpy ICM distribution will have a significant influence on gas distribution and velocity.

3.5 Summary

Our new VLA $5.0-7.0\,\mathrm{GHz}$ broadband observations of the edge-on Virgo Cluster galaxy NGC 4388 allowed us to reach unprecedentdly low noise levels, revealing striking new details of this object. The polarized emission, obtained for the first time for this galaxy with RM synthesis, shows extensions of the magnetic field toward the outskirts of the galaxy, indicating a connection between disk and halo. Two polarized filamentary structures appear at the end of both northern and southern nuclear outflows, which correlate with Hα and X-ray observations. The change in orientation of the magnetic vectors in the southern spiral arm reveals for the first time the southern nuclear outflow. Furthermore, two horizontally extended blobs of polarized emission are observed in the halo, about $2\,\mathrm{kpc}$ above and below the northeastern and southwestern spiral arms, respectively. Within these blobs, the ordered magnetic field is oriented perpendicular to the galactic disk.

The comparison between multiwavelength observations of prototype galactic winds shows that NGC 4388 does not host a symmetric central galactic wind. However, we suggest that, together with Hα, X-ray, and total power emission being located closer to the spiral arms within the halo, the blobs of polarized emission trace a galactic wind, which most likely originates from separate sources in the spiral arms. In such a scenario the CREs travel from the spiral arms into the halo, reaching distances of up to $\cong 3.3\,\mathrm{kpc}$ in the plane of the sky. Assuming equipartition between CR particles and the magnetic field, we estimate a total magnetic field strength for the different parts of the galaxy taking into account individual spectral indices and path lengths. In particular, our estimate of the total magnetic field strength for the polarization blobs is $(11 \pm 2)\,\mu\mathrm{G}$. With this magnetic field strength, the synchrotron lifetime of electrons in the polarized blob is $\cong (12 \pm 3)\,\mathrm{Myr}$. For traveling a distance of $\cong 3.3\,\mathrm{kpc}$, the average outflow

velocity of those particles is $(270 \pm 70)\,\mathrm{km\,s^{-1}}$, which agrees with the typical speed of a galactic wind expanding from the spiral arms into the halo.

Another edge-on Virgo galaxy, NGC 4402, shows a sharp edge in the radio continuum emission, which is interpreted as a compressed galactic halo. The observed symmetry of the polarized halo features in NGC 4388 excludes a compression of the halo gas by ICM ram pressure. We estimate the halo magnetic pressure and the ram pressure of the galactic wind to be $P_{\mathrm{halo}} \approx 3 \times 10^{-12}\,\mathrm{dyn\,cm^{-2}}$. This pressure is comparable to the thermal pressure derived from X-ray observations.

The estimate of the ICM ram pressure based on the galaxy velocity from dynamical models and a radially averaged ICM density profile from X-ray observations yields $P_{\mathrm{ICM}} \cong 3 \times 10^{-12}\,\mathrm{dyn\,cm^{-2}}$, in agreement with our estimate of the thermal halo pressure. If magnetic fields are ubiquitous in the halo, the halo pressure estimate increases. Allowing for ICM clumping, the actual ram pressure acting on NGC 4388 might be up to few times higher than what is expected based on a given galaxy velocity and an ICM density determined from X-ray and SZ observations.

NGC 4388, besides NGC 4569 (Chyży et al., 2006), is the second galaxy in the Virgo Cluster that shows a galactic outflow resisting ICM ram pressure. The detection of a radio halo around other cluster spiral galaxies could be used for an estimate of ICM density and ram pressure within a factor of a few.

Further observations at lower frequencies (GMRT, LOFAR, SKA) will reveal stronger total intensity emission from the halo of this galaxy, allowing us to do a spectral index analysis and therefore better constrain the aging of the CREs. Measurements of the large-scale structure of the halo magnetic field in NGC 4388 with the help of polarization data are needed, e.g. with the VLA S band, where good resolution in Faraday space can be reached. Hα observations are also crucial to constrain the velocities within the polarized blobs. We expect to see blue-shifted emission in the wind of the southern part and red-shifted in the northern part due to the inclination of the galaxy toward the observer.

This chapter is based on the article of Damas-Segovia et al. 2016 published in the Astrophysical Journal.

Precession of the Nuclear Outflow of NGC 4388

New broad band polarimetric observations of NGC 4388 showed extended features in the radio polarized intensity of this Virgo galaxy. In this chapter we show how a precession model can well explain those extended filaments. The precession model consists of a ballistic ejection of a precessing nuclear outflow. The direction of the outflow with respect to the line of sight is then introduced into the model and compared to a rotation measures map of the northern part of the nuclear outflow. We find that the precession model is in good agreement with the radio observations and this indicates a precession of the nuclear outflow as the origin of the polarization filaments seen in the halo of this galaxy.

Contents

4.1   Introduction

The magnetic outflows recently discovered in NGC 4388 revealed a filamentary magnetic field extending from the edge of both spiral arms of this almost edge-on galaxy up into the halo (see filaments in 4.1). These elongated structures were detected only in polarized radio emission at very low levels of signal to noise ratio due to the lower noise in the polarization maps. They have an extension of about 30″ to 50″ and are perpendicular to the disk, which means that, at a distance of 17 Mpc, the polarization filaments are at least 4.1 kpc and 1.7 kpc long without considering inclination. Both filaments in north and south emerge from the plane with a position angle of about 20° and bend towards the minor axis of the disk of the galaxy. From the position of the polarization filaments with respect to the disk, it seems that there is a physical relation with the nuclear outflow produced by the AGN activity. The northern filament of radio polarized emission correlates with observations of Hα (Yoshida et al., 2002) and in X-ray (Iwasawa et al., 2003) where there is a clear detection of the ejection of material from the galactic nucleus into the intra cluster medium (ICM) towards the north-eastern part of the galaxy. In the case of the region around the southern filament of radio polarized emission, there are indications of a less extended Hα outflow from the disk towards the south-western part of the galaxy that coincides with the radio observations.

The symmetric distribution of both polarization filaments with respect to the center of the galaxy suggests that these two features are related and may have a common origin. If this is the case, one possible scenario that could cause such structure is precession of the nuclear outflow that would distribute the injected material from the nucleus symmetrically with respect to the center of the galactic disk. Precession is a well known effect that is present throughout many different scenarios and that occurs at a large variety of scales in astronomy. This effect consists of a change in time of the angular momentum of a rotating body. In a rotating planet for example, the action of the gravitation potential of the Sun (and other bodies of the Solar system to a lesser extent) creates a torque that gives rise to the change in time of the angular momentum vector of that planet. This effect is found in planets and satellites of the Solar system and also in pulsars (Weisberg et al., 1989) and microquasars (Begelman et al., 2006). A spinning black hole at the center of an AGN will also be affected by the action of a torque from a companion black hole in a binary system (Stella & Vietri, 1998) or from a tilted accretion disk of in-falling material (Bardeen & Petterson, 1975). In some of these cases the action of the precession will shape the radio jets ejected by the AGN giving rise to sinusoidal twin outflows that are symmetric with respect to the center of the host galaxy (Cecil et al., 2000). Seyfert galaxies are a good case to study the interaction between a precessing radio jet and its environment
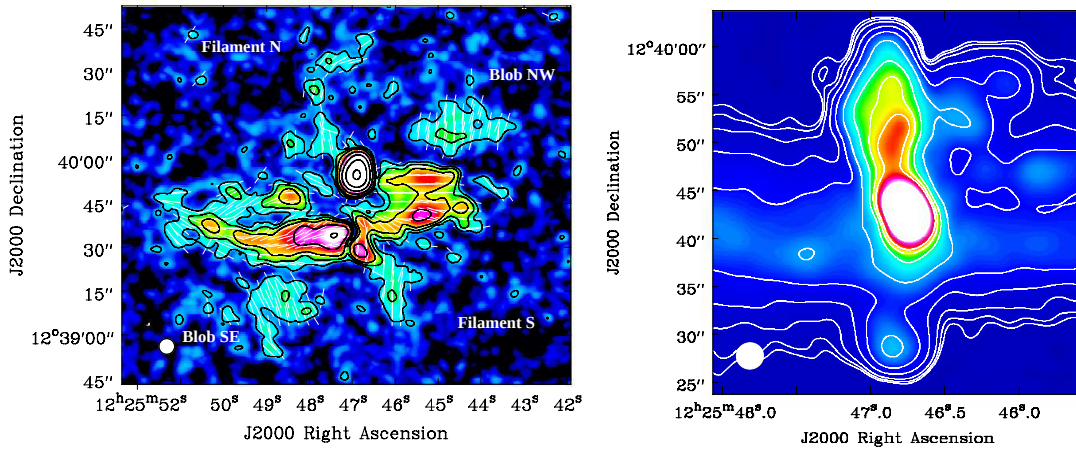
Figure 4.1: Left panel: linearly polarized intensity at $6.0\,\mathrm{GHz}$ in contours plus magnetic vectors with the same vector length, corrected for Faraday rotation, with a resolution of $5.33'' \times 5.33''$ and an rms noise of $2.3\,\mu\mathrm{Jy\,beam^{-1}}$. The contour levels are $(3, 5, 8, 16, 32, 64, 128) \times 2.3\,\mu\mathrm{Jy\,beam^{-1}}$. Both maps have been cleaned with a robust 2 weighting. Right panel: total power map of the same data set of the nuclear outflow. The contour levels are $(3, 4, 6, 12, 24, 50, 100, 150, 200, 400, 800, 1200) \times 6.0\,\mu\mathrm{Jy\,beam^{-1}}$ with a resolution of $2.76'' \times 2.67''$

since the radio jet most likely will push ISM material out of the galactic disk.

In this study we intend to understand the origin of the large scale structure of the magnetic field of the nuclear outflow of NGC 4388 through the comparison between a precession model and the radio polarization maps. NGC 4388 is of special interest due to its kinematics and interaction with the ICM. Thus we can also study the interaction between a precessing outflow and the ram pressure action.

In the present study we will discuss about the possibility of a precession of the nuclear outflow as the origin of the characteristics features observed in NGC 4388. In Section 4.3 we show an analysis of rotation measures of the northern nuclear outflow. Then, in Section 4.4, we make use of a precession model to compare it with the radio data. The inclusion of a direction of the modeled outflow in order to study the direction of the magnetic field of the outflow in the precession scenario is shown in Section 4.4.4. A comparison between the precession model and the complex filaments seen in Hα is presented in Section 4.4.5. In Section 4.6 there is a final discussion.

4.2   Magnetic Field Filaments

In the total radio intensity images of NGC 4388 (see Figure 4.1, right panel) the nuclear outflow clearly extends towards the north about $20''$ from the nucleus. There is no discontinuity like in the southern part where we could only infer the existence of a nuclear outflow by the detection of a hot-spot at about $18'' \approx 1.5\,$kpc from the nucleus. In this case, we only see a connection between the southern hot-spot and the nucleus thanks to the polarized intensity map (Fig. 3.3). The magnetic vectors in the southern part of the nuclear outflow line up with the minor axis of the disk and show a wiggling structure of the magnetic field vectors.

   We consider the symmetric bending with respect to the center of the disk as an indication of a common origin of both polarization filaments. Also, both structures in north and south are similar in length and width. This can be interpreted as the time of ejection from the nucleus being similar.

   There is a difference in brightness between both spots of the northern and southern nuclear outflows. They differ in total intensity flux density by $\cong 8$mJy beam^{-1} although they are similar in area ($18'' \times 8''$). It is unclear why these two features show different magnitudes. The interaction with the ICM could be responsible for this asymmetry since ram pressure is acting only from the south of the galactic disk. Another possibility could be internal asymmetries in the gas density close to the nucleus that affect the propagation of both southern and northern outflows in different ways. This asymmetry is also seen in the polarization filaments that follow both spots being the southern one shorter that the northern one by about $\cong 7''$. This could also be related to the action of ram pressure.

   The magnetic field vectors of these magnetic filaments follow the path along the elongated structure. This indicates that the large scale magnetic field of these polarization filaments is related to the Hα and the X-ray outflows mentioned above. If this is the case, all the outflows events seen in the halo of NGC 4388 have a related origin (see Section 4.4.5).

4.3   Rotation Measures

The map of rotation measures (RM) shown in Fig. 4.2 is produced from the data cubes resulting from an RM synthesis analysis of the C-band C-configuration dataset from the CHANGES survey. Each spectral window has been cleaned using a robust weighting of -2 to achieve higher resolution ($3.99'' \times 3.99''$). The method used to produce this map is the same as the one described in Section 3.2.
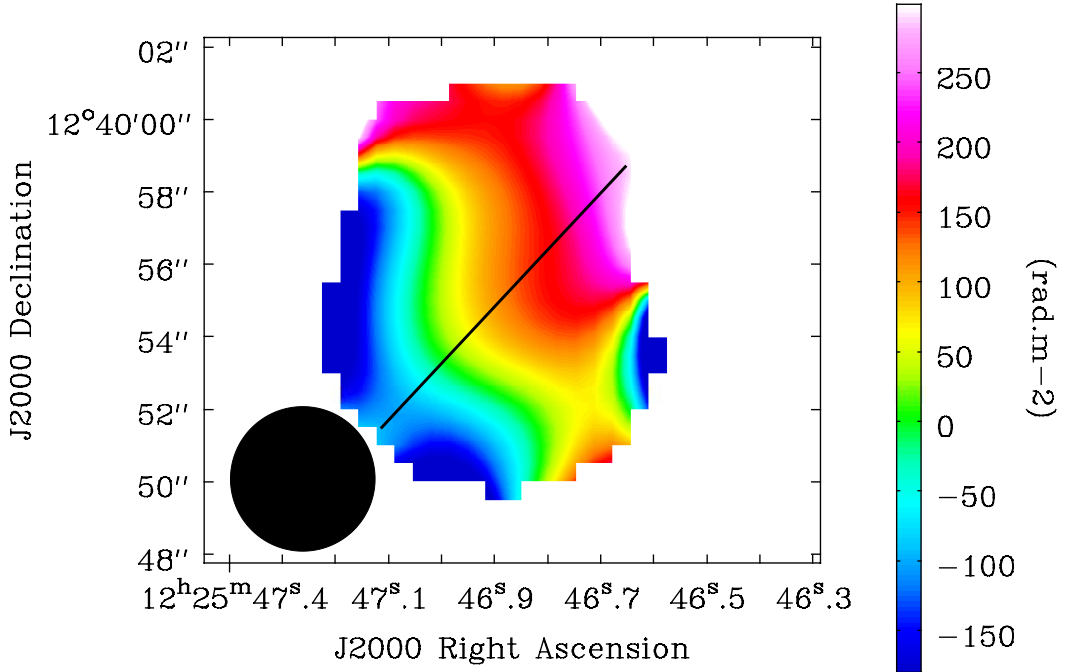
Figure 4.2: Rotation measures map of C-band C-configuration of the northern part of the nuclear outflow. This map was obtained with an RM Synthesis analysis using robust -2 for the imaging of individual spectral windows and that gives a final resolution of $3.99'' \times 3.99''$. The black line indicates the slice shown in Figure 4.3.

With this resolution the northern spot is sampled by $\cong 9$ beam areas which gives us good confidence for the analysis of this structure. The produced images were smoothed to the beam size of the lowest resolution spectral window and primary beam corrected. The values of RM vary roughly from around $-200\,\mathrm{rad\,m^{-2}}$ to $+160\,\mathrm{rad\,m^{-2}}$ crossing the $0\,\mathrm{rad\,m^{-2}}$ value at the center of the region where the maximum polarized intensity is found. In Figure 4.3 we show a slice cut through the polarization region of the northern part of the nuclear outflow in which the asymmetry of RM can be better quantified. The RM values have been not corrected for the foreground RMs of the Milky Way but they are only of the order of $\cong \pm 10\,\mathrm{rad\,m^{-2}}$ (Oppermann et al., 2012) for that region of the
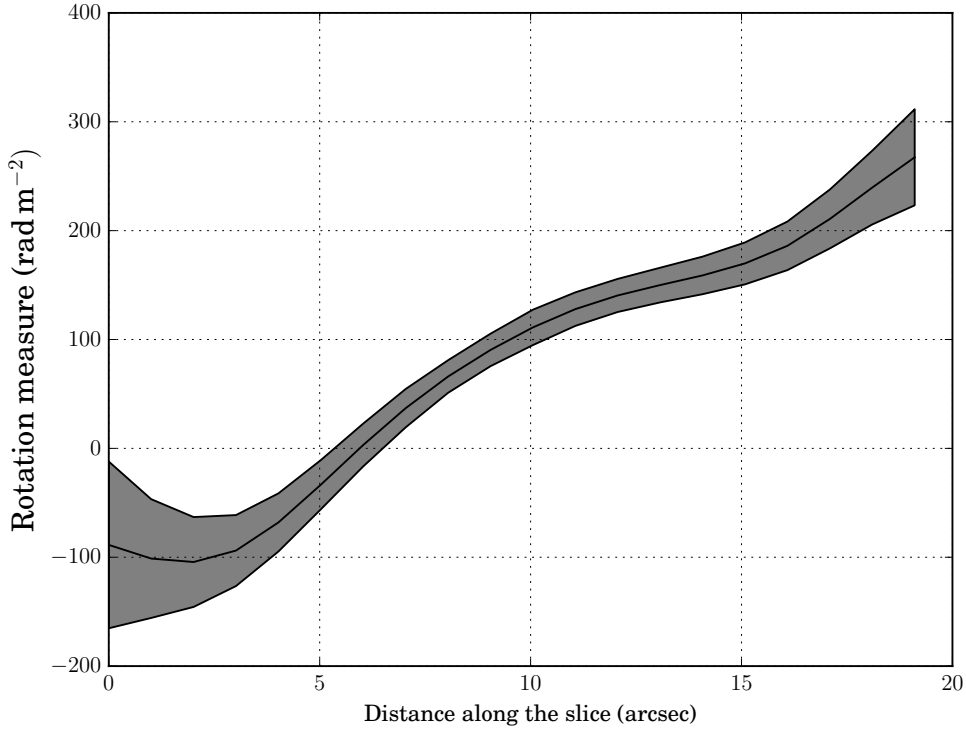
Figure 4.3: Slice of rotation measures from Figure 4.2. The gray shade represents the error in rotation measures.

sky. The error in RM was calculated as $\sigma_{\mathrm{RM}} = 0.5\Delta\phi/(S/N)$ (Iacobelli et al., 2013) where $\Delta\phi \cong 2000\,\mathrm{rad\,m^{-2}}$ is the RMSF width and S/N is the PI signal to noise ratio.

The change in the magnetic field direction with respect to the line of sight would give rise to a change in the RM pattern along an AGN jet. This kind of asymmetry is common in many AGN jets observed in very high resolution studies using very large baseline interferometry (VLBI) (Gabuzda et al., 2015). The polarization angle points in one direction on one side of the jet axis where the magnetic field curves towards the observer and in the opposite direction on the other side of the jet, where the magnetic field curves away from the observer. At the center, between these two sections of the jet, the magnetic field is parallel to the plane of the sky, resulting in an RM of $0\,\mathrm{rad\,m^{-2}}$. Any change in the inclination of the jet with respect to the observer will translate into different absolute values of RM between these two regions and different positions for the $0\,\mathrm{rad\,m^{-2}}$ region with respect to the jet axis.

The asymmetry seen in NGC 4388 could be a product of the presence of a helical magnetic field surrounding the whole nuclear outflow. The energy of the
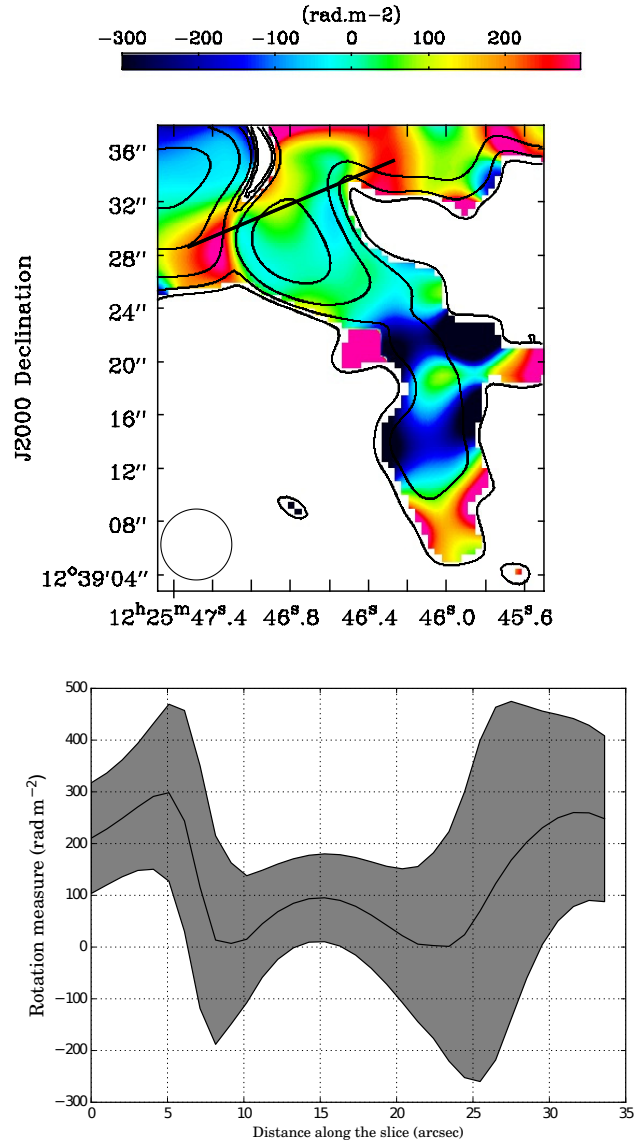
Figure 4.4: Top: detail of the southern nuclear outflow in the C-band C-configuration polarization map with a slice profile (black solid line) taken over the nuclear outflow. Contours of radio polarization intensity are $(3, 4, 6, 12, 24, 48, 96) \times 2.5\,\mu\mathrm{Jy}\,\mathrm{beam}^{-1}$ with a resolution of $5.33'' \times 5.33''$ over a color scale of the rotation measures map at the same resolution. Bottom: slice of rotation measures from the top panel. The gray shade represents the error in rotation measures.

nuclear outflows at kiloparsec scales is low compared to the energy of typical AGN jets studied with VLBI, which are focused on parsec scales. Jets in low luminosity radio galaxies are known to decelerate from relativistic speeds to non-relativistic speeds from parsec scales to kiloparsec scales, respectively (Perucho

et al., 2014). The direction of the vectors in the polarized intensity image is parallel to the outflow axis, contrary to what is expected from a helical magnetic field where magnetic vectors are orientated perpendicular to the jet axis.

The RM map of the southern nuclear outflow shows a drastic change in the RM value ($\cong 300\,\mathrm{rad\,m^{-2}}$) when comparing with the neighboring values at the inter-arm regions. In Figure 4.4 we show a detail of the southern nuclear outflow in the C band-C array polarization map with slice profile taken over the nuclear outflow. This map was made using a robust parameter of 2 in order to detect fainter areas of extended emission. The profile was taken in order to better see the change between spiral arms values and nuclear outflow. This change in RMs might be due to the superposition of the southern nuclear outflow emission and the spiral arm emission which is behind. In Section 3.4.1 we showed a change in the orientation of the magnetic vectors in the same region where we see the change in RMs, thus both effects might be caused by the superposition of the nuclear outflow structure on top of the emission from the spiral arm. It is important to mention that this conclusion cannot be made from the total power maps, since there is no structure visible other than the spot at the end of the nuclear southern outflow.

We conclude that the asymmetry found in the RM map of the northern spot of NGC 4388 has a different origin than that seen in VLBI jets. Thus, this RM pattern is not product of the internal helical structure of a magnetic field created by adding poloidal and longitudinal components but might indeed be the result of the orientation of the magnetic field characterized by the direction of the outflow ejection possibly of helical shape (see Section 4.4.4). Also, the drastic change in the RMs of the southern nuclear outflow supports the idea of having an outflow in front of the spiral arm.

4.4   Precession Model

4.4.1   Basic Parameters

The precession of radio jets and outflows has been well studied in twin-jet systems through analytical models that describe the different epochs of ejections of these objects. One of the best examples of such systems can be found in the microquasar SS 433. The analysis of proper motions in SS 433 by Hjellming & Johnston (1981) explained the extreme radial velocities of the optical jets and also the morphologies seen in the radio jets. By adjusting timescales and velocity in the equations of precession, the model can be extrapolated to galactic scales to study AGN nuclear outflows (Gower et al., 1982; Kharb et al., 2006).

In this study we apply a similar model for the case of NGC 4388. To be able

to compare both model and observations, we show the model data as projected on the plane of the sky and scaled to a distance of 17 Mpc which is the distance to the Virgo cluster.

We have developed an interactive tool (Figure 4.5) to help finding the best combination of parameters with the only constraint of the timescale. In order to decrease the number of solutions to the set of equations, we need to put constraints on the parameters used in the model. The synchrotron lifetime of the CREs along the filaments of polarization can be used as a limit on the total time the jet is operating. Taking the values of total magnetic field from Table 3.1, $\cong (19 \pm 2)\mu G$, we obtain a lifetime for the CREs of $(6.0 - 8.0) \times 10^6$ yr. This timescale already sets the precession period to be $P \cong (3.5 - 4.5) \times 10^6$ yr as inferred from the direct comparison with the observations.

Another parameter included in the equations is the position angle of the jet on the plane of the sky (noted as χ in Table 4.1a). There are VLBI studies that successfully detected the radio nucleus of this galaxy (Giroletti & Panessa, 2009; Mundell et al., 2000), but their estimates of PA are not accurate enough since the jet structure is not resolved in these observations. For this reason, we take as a present-day angle χ the one given by the water maser found by the MEGAMASER project in this galaxy (Kuo et al., 2011). From the rotation curve of the circumnuclear water maser, Kuo et al. (2011) estimated a maser radius of about $\cong 0.3$ pc and a black hole mass of $M_{BH} \approx 8.5 \times 10^6 \, M_{\odot}$. For consistency we take χ perpendicular to the position angle of the maser found in this galaxy. The position angle of the maser is 107° therefore the present-day position angle of the ejection should be perpendicular to that direction ($\chi \cong 17°$). We have found that the angle that better fits the PA of the observed radio emission is $\chi \cong 13°$ which is very close to the perpendicular direction of the maser disk. We discuss this similarity and its implication to the explanation of the origin of the precession in this galaxy in Section 4.5.

Since there is an uncertainty in the rest of the parameters, the set of solutions obtained to fit the data is not unique. This is because there is a degeneracy of the system of equations so that some of the parameters are coupled. Therefore, we need to make assumptions for those parameters that are unknown as velocity, inclination and the opening angle of the precession cone. We find that the maximum inclination of the jet with respect to the line of sight can be of 50°. This is because for larger values of inclinations the shape of the polarization filaments is not well recovered in the modeled curves. Given that the galaxy has an inclination of 79°, the minimum limit of inclination of the nuclear outflow with respect to the line of sight is 11°. Less than that would mean that the southern jet is behind the disk with respect to us but we discarded this option because otherwise we would not see the magnetic vectors along this part of the nuclear outflow (see Section 4.1).

Table 4.1: Precession parameters for NGC 4388

Parameter	Value
i (deg)	$15 - 50$
ψ (deg)	$3 - 10$
χ (deg)	13
v_{north} (km s^{-1})	$1300 - 2300$
v_{south} (km s^{-1})	$500 - 1000$
s_{rot}	$+1$
P (yr)	$(3.5 - 4.5) \times 10^6$
t (yr)	$(6.0 - 8.0) \times 10^6$

(a) i: inclination of the nuclear outflow with respect to the plane on the sky. ψ: opening angle of the precession. χ: position angle of the outflow on the plane of the sky. v: velocity of the outflow. s_{rot}: sense of rotation. P: period of the precession in years. t: total time in years that the outflow is activated constrained by the synchrotron life-time of the CREs of the outflow.

With a limit on the total time since the initial ejection, fixed by the synchrotron lifetime of the CREs in the polarization filaments, we can then put some limits on the velocity and the inclination parameters of the model. We measured an extension of the outflow from the nucleus to the very end of the polarization filaments of $l_{\mathrm{north}} \cong 65''$ and $l_{\mathrm{south}} \cong 35''$ for the northern and southern extensions, respectively. This corresponds to $l_{\mathrm{north}} \cong 5.4\,\mathrm{kpc}$ and $l_{\mathrm{south}} \cong 2.9\,\mathrm{kpc}$ in projection. This difference in longitude between northern and southern extensions might be caused by different velocities in the outflows. This effect will be discussed in following sections. From these values we estimate an inclination between 15° and 50° with corresponding velocities between $1300\,\mathrm{km\,s^{-1}}$ and $2300\,\mathrm{km\,s^{-1}}$ for the northern outflow and $500\,\mathrm{km\,s^{-1}}$ and $1000\,\mathrm{km\,s^{-1}}$ for the southern one. Taking into account the inclination of the outflow, the line of sight component of the velocities estimated for the northern part of the outflow are in good agreement with the velocities measured in Hα studies. This also sets the values for the opening angle of the precession to $\psi \approx 6 - 10°$.

A final parameter s_{rot} defines the direction of rotation of the nuclear outflow being $+1$ counterclockwise (right-handed) or -1 clockwise. For our case we find that the direction of rotation of the nuclear outflow is $s_{\mathrm{rot}} = +1$, counterclockwise.

In Table 4.1a we show the parameters used for the best approach to the data.

This configuration of parameters produces the wiggling structure of the southern nuclear outflow seen in the polarization maps and at the same time gives rise to the two polarization filaments when reaching the galactic halo (see Figure
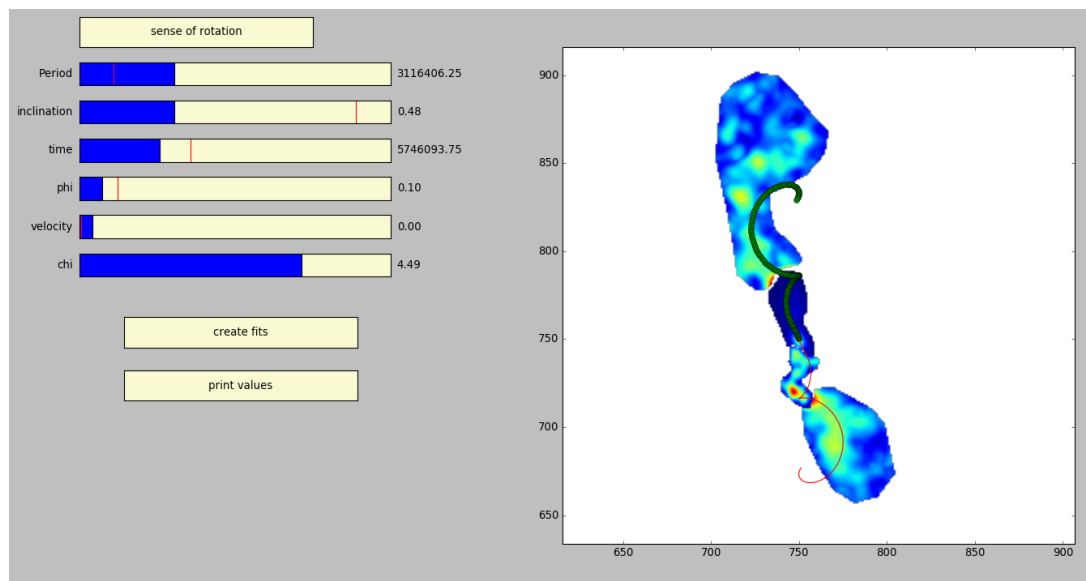
Figure 4.5: Visual tool to adjust the precession model to the radio data. Green points represent the modeled ejected components that point towards the observer and the red continuous line shows the same components but pointing away from the observer. In the background different components of the radio maps of the nuclear outflow are shown. This is added in order to help the user to fit the model to the data. This tool was developed using the module Matplotlib (Hunter, 2007) within Python 2.7 Software Foundation. (Python Language Reference, version 2.7, available at http://www.python.org)

4.6).

It is also noticeable that this set of parameters chosen to fit the radio data is capable to connect the large scale features seen in the VLA observations with the position angle of the maser disk seen in the nucleus of this galaxy. After producing a set of points from the precession model and projecting them onto the plane of the sky in sky coordinates, we smoothed the model map to the beam of $5''$, comparable to our VLA observation (Figure 4.6). This convolution was made in order to better compare the model products with the radio observations that are also smoothed to the same resolution. The modeled smoothed map also shows two 'hot-spots' in north and south that are very similar to the areas where the radio intensity and the polarization increase. We therefore think that both spots are regions where the nuclear outflow has higher inclination with respect to the plane of the sky and lines up with the line of sight where high values of RMs are seen. In other words, it is in those regions where we see more magnetic fields integrated along a similar path length and that makes the synchrotron radiation brighter. This scenario would also explain the high degree of polarization seen in the northern part of the nuclear outflow.

The similarities between the radio data and the precession model are striking

and reveal a possible relation between the large-scale structures seen in polarization and the spots seen in polarization and in total power closer to the nucleus.

Our estimate gives then a minimum active time of 6.0×10^6 yr. Whether the nuclear outflow has been active earlier we cannot tell from our observations.

The presence of a possible nutation of the system is not included in this model but we expect that this effect is of minor impact than the precession at large scales. However, we have to take into account that all these estimations depend on the assumed distance to the Virgo cluster that could in principle add possible errors to the calculation of the speed of the ejection.

We are aware that a relativistic jet could produce helical structures via Kelvin-Helmholtz instabilities. In the present case the speed of the outflow is likely to be mildly relativistic at large scales since this is expected for jets of Seyfert galaxies (Bicknell et al., 1998; Middelberg et al., 2004).

4.4.2 The Asymmetry Between Northern and Southern Polarization Filaments

There is an asymmetry in the length between the northern and southern polarization filaments that is only present when the nuclear outflow reaches the outskirts of the galactic disk. In the case a relativistic outflow ($\beta \geq 0.1$) with a relatively large inclination towards the observer, the model of precession fits well to this asymmetry due to relativistic projection effects. But this idea is in conflict with the Hα images by Yoshida et al. (2002) which show ionized hydrogen next to both polarization filaments. The Hα and X-ray outflows also shows the asymmetry between north and south with non-relativistic speeds. An internal asymmetry close to the point of ejection could cause such an asymmetry at larger distances but this would not answer why the asymmetry is only seen at the very end of the galactic disk.

We propose that the polarization filaments (and with them the Hα and X-ray outflows) are being affected by the ram pressure of the ICM. Since the galaxy is moving towards the south, the ram pressure would suppress the southern part of the outflow and would extend the northern one beyond $\cong 3$ kpc from the nucleus on the plane of the sky. The inclination of the nuclear outflow with respect to the galaxy plane might cause the disk to shield only the inner part of the outflow from the action of the ICM.

It is also expected that the action of ram pressure on the polarization filaments would change the initial inclination with which the nuclear outflow was ejected. In this way, both northern and southern outflows would not share the same central axis anymore and the whole structure would take the U-shape characteristic of radio jets deformed by the ICM ram pressure.
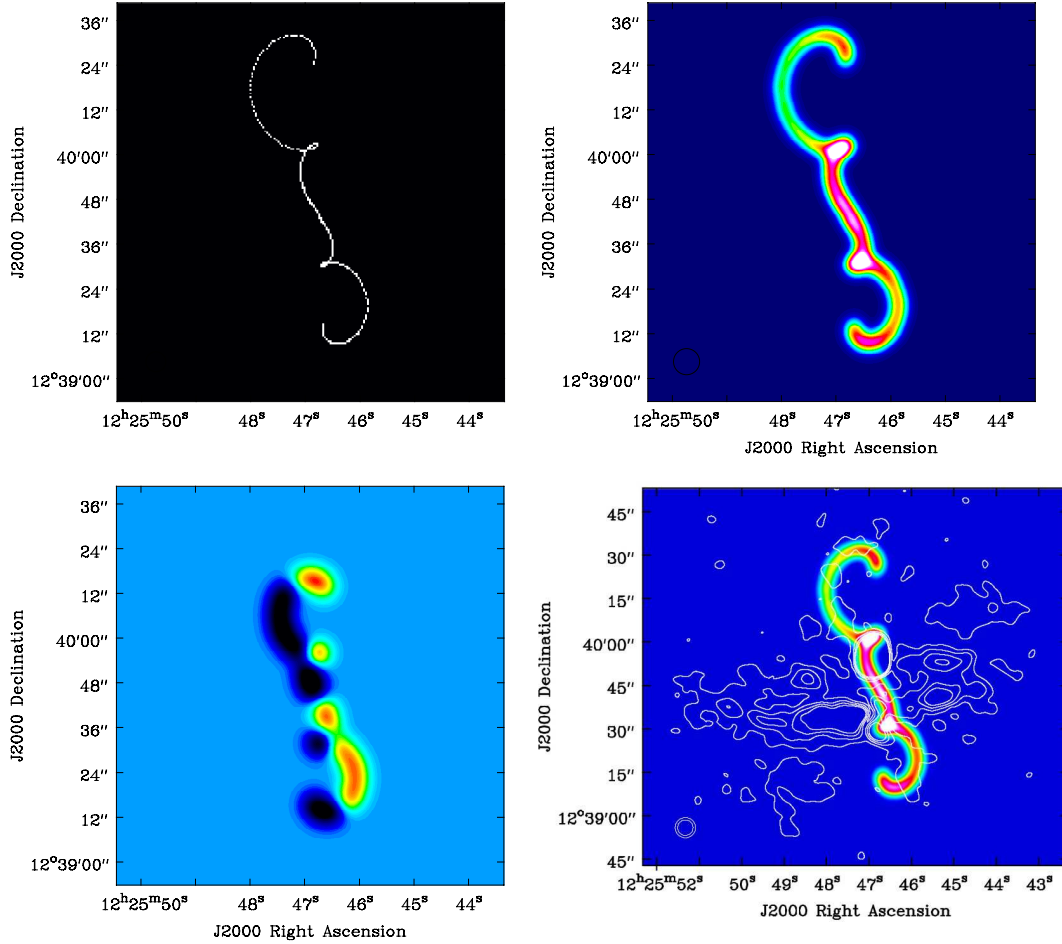
Figure 4.6: Different steps of the procedure for creating modeled maps in order to compare the precession model to the radio data. Top left panel: initial model map in FITS (Flexible Image Transport System) format. Top right panel: same initial map as before but smoothed to the beam of our radio observations ($\cong 5 - 10''$). Bottom left panel: smoothed model map including the direction of the outflow with respect to the observer. Blue and red show that the outflow goes towards or away from the observer, respectively. Bottom right panel: smoothed model map over-plotted with the polarized radio map from EVLA.

4.4.3 Comparison Between the Direction of Ejections and the Magnetic Field Vectors

This model consists on a ballistic precessing outflow that periodically ejects material out into the environment. This means that the individual parts of the
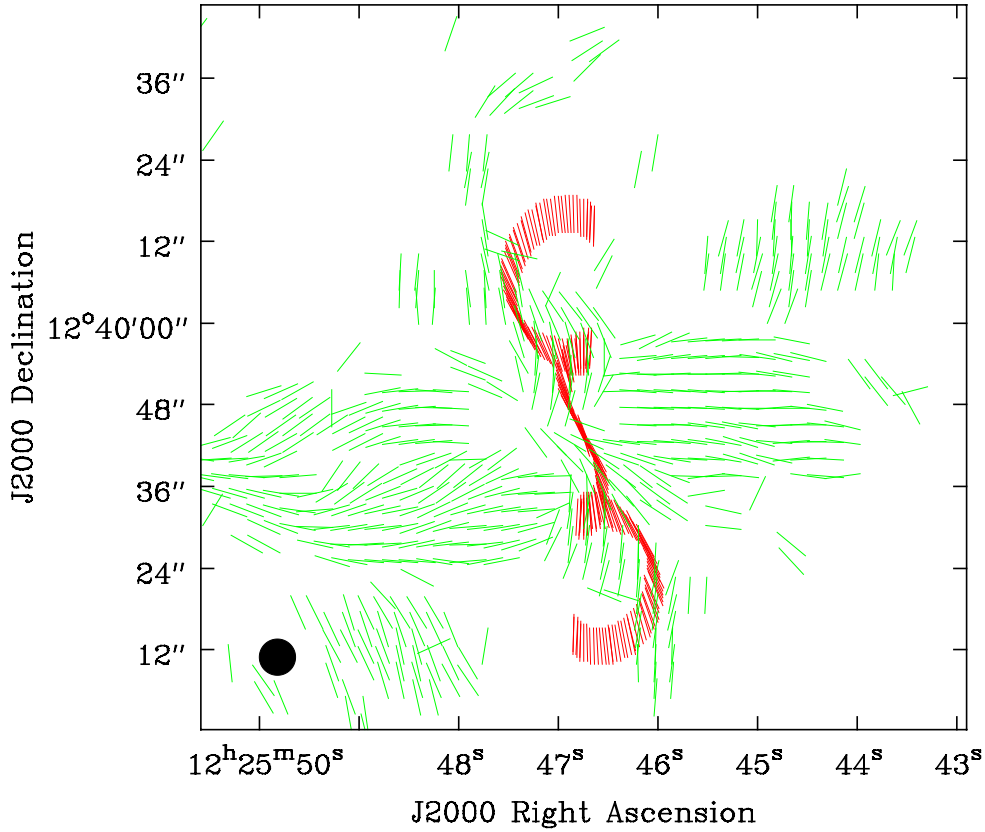
Figure 4.7: Comparison between magnetic field vectors (green) and initial directions of ejections (red). The magnetic field vector map was obtained from the an RM Synthesis analysis and has a resolution of $5.33'' \times 5.33''$ at 6.0 GHz. The length of the vectors of initial directions is chosen with the only purpose of a better visualization.

outflow are only spatially connected and they are not linked by any common larger structure. However, the radio polarized map shows a continuous magnetic field along the northern and southern outflow that correlates with the Hα and the X-ray outflows, suggesting that there is a connection between individual parts of the outflow. One explanation for the presence of a continuous field could be that the magnetic field seen along the filaments was initially part of the ISM surrounding the galactic nucleus and carried out by the individual ejections of the AGN. In this way the magnetic field tends to order in the direction of the outflow and form a continuous structure. In this scenario a continuous connection is expected between the magnetic field along the outflow filaments.

The possibility that the magnetic field originated in the individual ejections

keeps the original direction of the precession axes and does not get disrupted by the surrounding medium can be rejected looking at Figure 4.7. This image shows the vector map where each individual ejection is represented by a vector with the direction which was first characterized at the moment of ejection at the center of the galaxy. This means that the velocity vector given to each ejection has not the same direction as all magnetic field vectors. The ISM magnetic field reacts to the ram pressure created by the individual ejections and tends to align perpendicularly to the direction of the individual ejections by compression.

There have been studies comparing the direction of ejection and the direction of magnetic vectors in the microquasar SS 433 (Stirling et al., 2004; Roberts et al., 2008). Their conclusions are compatible to ours since their comparison between ejection model and magnetic field vectors from polarized radio observations do not show a correlation between magnetic vectors and initial ejection vectors.

4.4.4 Extended Precession Model

Figure 4.8: Radio polarization contours from EVLA overplotted with a smoothed map of the precession model. This model includes the direction of the nuclear outflow towards the observer: blue and red parts indicate oncoming and receding parts from the point of view of the observer, respectively.
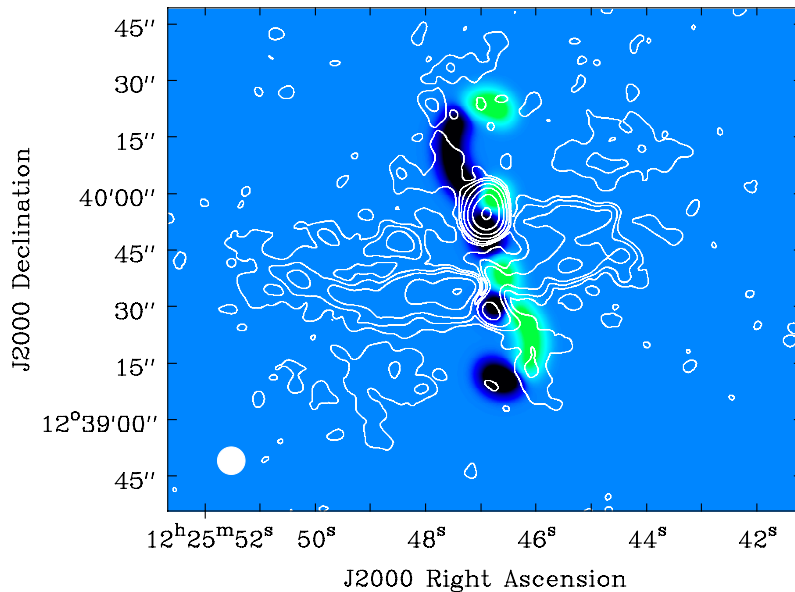
The magnetic field direction in the line of sight can be inferred from the RM study of the radio maps. The sign of the RM will determine the direction of the magnetic field along a given line of sight, being negative if the field lines are going away from the observer and positive if contrary. In a precessing nuclear outflow, it is expected to observe changes in the direction of the gas with respect to the line of sight due to the intrinsic movement around the precession axis. If we now consider that the same direction is also followed by the intrinsic magnetic field within the outflow, then the RM observation should show a change in the sign of the RM values along the main axis of the outflow. This effect is well studied in powerful jets of radio galaxies (Gabuzda et al., 2015) but it has never been observed in the jet/nuclear outflow of a Seyfert galaxy. The northern outflow of NGC 4388 shows a well defined RM asymmetry that could be product of the helical magnetic field created by a precessing outflow. For this reason, we introduced the possibility to show the direction of the outflow with with respect to the observer in the model. Each point of the outflow model has a value of $+1$ or -1 depending on the outflow flows towards or away of the observer, respectively. This addition to the model shows the direction of the nuclear outflow with respect to the observer at every point along the outflow trajectory but it can also be associated to the magnetic field direction (see Figure 4.8).

In Section 4.3 we have shown the characteristic RM map of the nuclear outflow in NGC 4388. The gradient seen in the RM map could be produced by the precession mechanism described above. Figure 4.9 shows the comparison between the RM map generated from the radio observations (left panel) and the modified precession model (right panel). The colors in both maps are shown in such a way that blue and red represent parts of the outflow that are moving towards or away from the observer, respectively. Both maps are overplayed with polarization contours. Our modified precession model also shows a gradient from negative to positive numbers due to a drastic change in the orientation of the nuclear outflow with respect to the observer withing a small area on the plane of the sky. It is notable that in both cases, observation and model maps, the values that indicate the direction of the outflow go through the value of 0 at some point within this particular region. The similarity between observations and precession model is an indication of the origin of the RM feature seen in the northern part of the nuclear outflow of NGC 4388 and provides an independent signature of the precession of this outflow. The present study provides the opportunity to explain the asymmetry in RM seen in the northern outflow by comparing model products and radio data.

The fact that we see an asymmetry in the RM of the northern nuclear outflow is a signature of helicity in this structure. But this helicity does not arise from the combination of poloidal and toroidal field as proposed in the VLBI studies mentioned above. The helicity present in NGC 4388 is a consequence of a stream
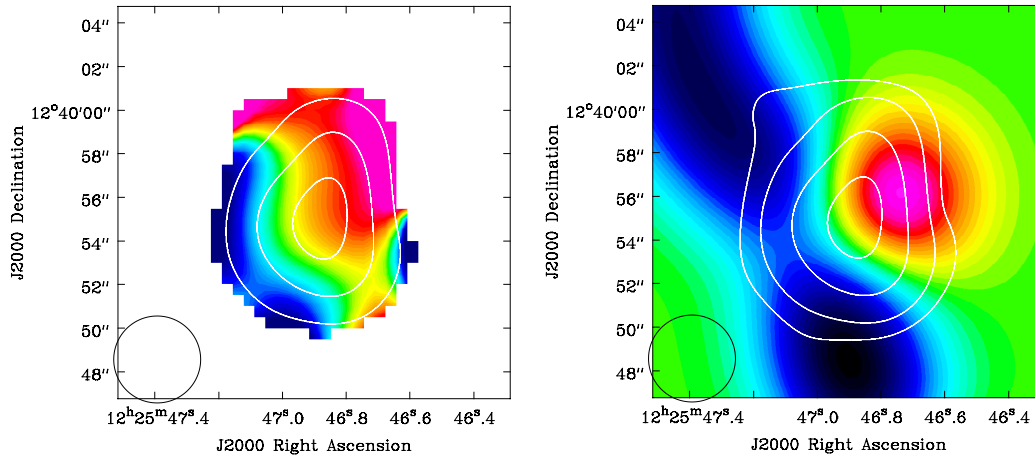
Figure 4.9: Comparison between rotation measures map from the EVLA data (left panel) and the modeled direction of the precessing outflow (right panel). Both maps are overplayed with polarization contours. In the case of the EVLA data map, red and blue indicates magnetic field that points towards and away from the observer. The model map shows red and blue where the nuclear outflow points towards and away from the observer.

of material going along certain axis that varies in time due to a precessing ejecta.

4.4.5 Precession Model Compared to the Hα Outflow

The map generated by the precession model including direction gave very similar RM structures than what is seen in the RM maps from radio observations. It would be ideal to reproduce the outflow much further but there is a limit in the extension we are able to see in the radio observations. This limit depends mainly on the magnetic field strength and the CRE density of the nuclear outflow and therefore on the sensitivity of our observations.

The analysis of the Hα outflow studied by Yoshida et al. (2004) helps to compare our precession model to the nuclear outflow at larger distances from the galactic disk. If we extend the timescale of our model we can estimate how older parts of the outflow would appear in the Hα counterpart. In their Hα study, Yoshida et al. (2004) shows what they call the very extended emission-line region (the 'VEELR') in a velocity field map. This group of filaments and clouds are thought to be kinetically associated and their morphology suggests that they are being pulled out of the ISM of the galaxy by the action of the ram-pressure. In Figure 4.10 we can see a comparison between the Hα velocity

field and an extended version of the precession model. Almost every filament in the Hα map is blue-shifted, meaning that the are moving towards the observer. In the case of the new added parts of the precession model, we can see how most of the northern chunks of the outflow are mainly blue-shifted. We consider this similarity to be remarkable and suitable to explain the why the velocity field that we see in the Hα is mostly blue-shifted.
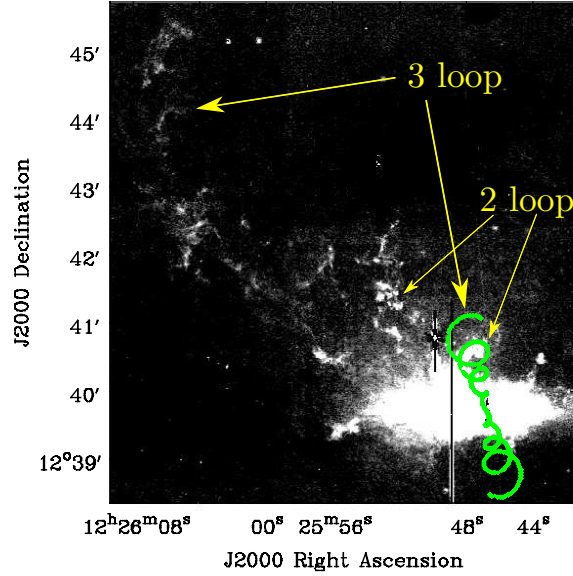
Figure 4.10: Comparison between Hα observations from Yoshida et al. 2002 and the modeled precessing nuclear outflow extended in time-steps. The yellow arrows point to the second and third loop of the modeled precessing outflow in green and the consequent filament in the Hα outflow.

One characteristic of the VEELR filaments is the variety of velocities between the different filaments. They show a complex velocity field within a wide range that goes from $\cong -50\,\mathrm{km\,s^{-1}}$ to $\cong -700\,\mathrm{km\,s^{-1}}$. This fits well with the idea of the filaments being originated in the precessing outflow. The action of a constant ram pressure from the ICM will affect in different ways the kinematics of a cloud that is moving in the same direction of the ram pressure stream (towards the north)and another cloud that is opposite to that stream (towards the south).

Another indication for the VEELR features to have an origin in the precession of the nuclear outflow is the morphology of some of its filaments. Most of them are curved towards the west, against the action of the ram-pressure which is acting towards the opposite direction. We suggest that there are similarities between between the direction of this VEELR filaments and the direction of the

extended filaments in our precession model.

It is possible to extend the timescale of the modeled nuclear outflow by two more periods. The fact that we do not see this extra loops in the observations could be explained by the action of the ram pressure removing them when they reach a certain point in the halo of the galaxy. The disk of the galaxy would shield the nuclear outflow from the ICM stream until the outflow escapes out of the shadowing of the disk. At this point the loops created by the precessing outflow would be moved in the direction in which ram pressure is acting from but partially keeping their intrinsic angular momentum. This can be tested with the time steps of the different loops provided by our model. The third and fourth loops of the precession model are generated 2.8×10^6 yr and 6.3×10^6 yr after the second loop, respectively. If we assume that after being exposed to the ICM stream the clouds associated to the loops travel at the speed of $\cong 2500 \, \mathrm{km \, s^{-1}}$, according to our model, the third and fourth loops would be at a distance of $\cong 7 \, \mathrm{kpc}$ and $\cong 16 \, \mathrm{kpc}$ from their original position, respectively. These distances are in good agreement with the ones measured in the Hα maps of Yoshida et al. (2004) which indicate a distance of $\cong 7 \, \mathrm{kpc}$ and $\cong 20 \, \mathrm{kpc}$ from the origin to the North High Velocity (N-HV) Filaments and the NE High Velocity (NE-HV) Filaments, respectively.

Vollmer & Huchtmeier (2003) reproduced the ISM gas evolution of this galaxy in the presence of a ram pressure action of the ICM. This study showed in great detail the complexity of the gas outflow created after the galaxy passed through its closest approach to the cluster core where the ram pressure peaked at a maximum value of $5 \times 10^{-11} \, \mathrm{dyn \, cm^{-2}}$.

We propose that the complexity and distribution of the velocity field in the clouds and filaments of the Hα northern outflow mainly originates in the precessing nuclear outflow and is stripped away to larger distances by the ram pressure over a period of time of $\cong 6.3 \times 10^6$ yr.

In Figure 4.11 we show a sketch of the precessing system as viewed from a side of the galaxy.

4.5 On the Origin of the Precession of the NGC 4388 Nuclear Outflow

The similarities between the filamentary structures found in the radio maps and the structures obtained from the precession model suggest this scenario is a plausible explanation for the nuclear outflow morphology of NGC 4388. Since the large scale features are then related to small scales of the AGN close to the nucleus, these observations could also show hints on the origin of the precession of the accretion disk in this galaxy. The change in the rotational axis of a rotating
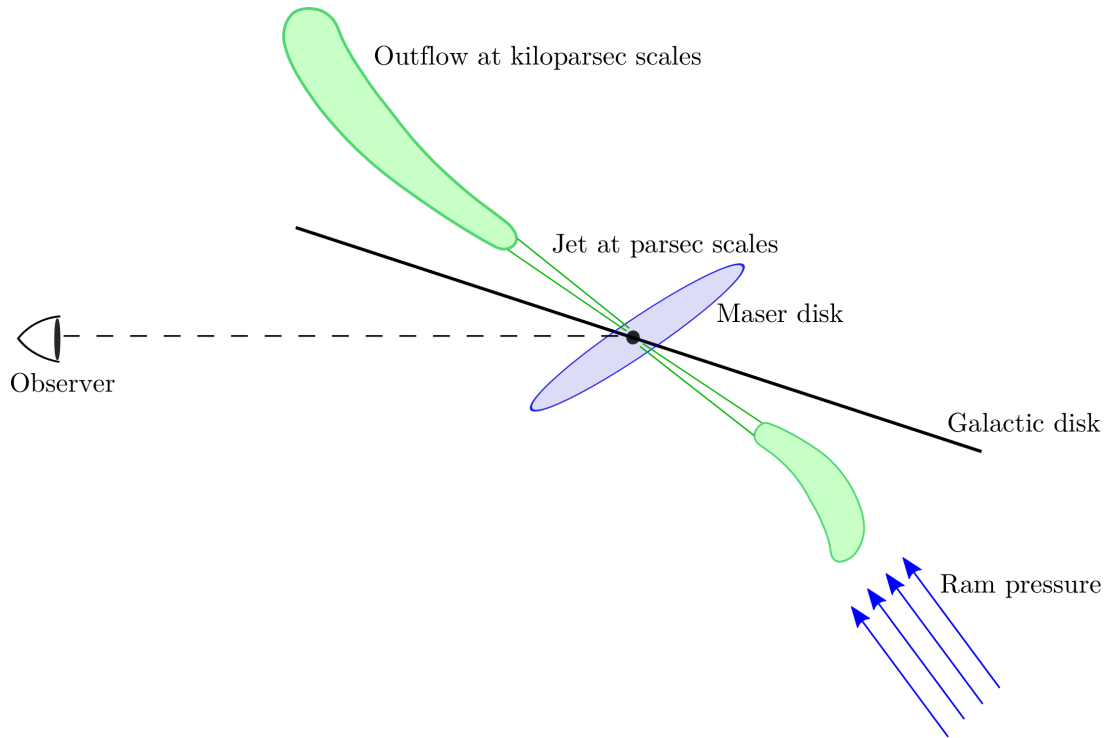
Figure 4.11: Sketch of the nuclear outflow and its position with respect to the maser disk.

body appears when there is a gravitational distortion on the kinematics of a rotating body. In the case of AGN jets this distortion could be the result of the interaction in a binary black hole system (Lobanov & Roland, 2005). This distortion could also be produced by the surrounding tilted accretion disk when the jet material is ejected by a spinning black hole (Lu & Zhou, 2005). In both cases the result is a change in the direction of the angular momentum that creates a sinusoidal shaped jet. In the case of a binary system, the distortion caused by the interaction between the two black holes produces ejected material with a C-shaped morphology (Ekers et al., 1978; Miley, 1980). In the case of a precessing black hole the distortion created has an S-shaped configuration (see Figure 4.12).

The configuration observed in the polarization filaments of NGC 4388 resembles an S-shaped outflow. Therefore, we now consider the second scenario, where the precession is caused by the torque action of the tilted accretion disk on the angular momentum of a spinning black hole. This case is consistent with the perpendicular orientation of the maser with respect to the position angle of the nuclear outflow at different resolutions. In principle, we can estimate the period of the precession with the mass and the mass accretion of the AGN accretion disk through their relation with the precession period (equation 2 in Lu & Zhou 2005):
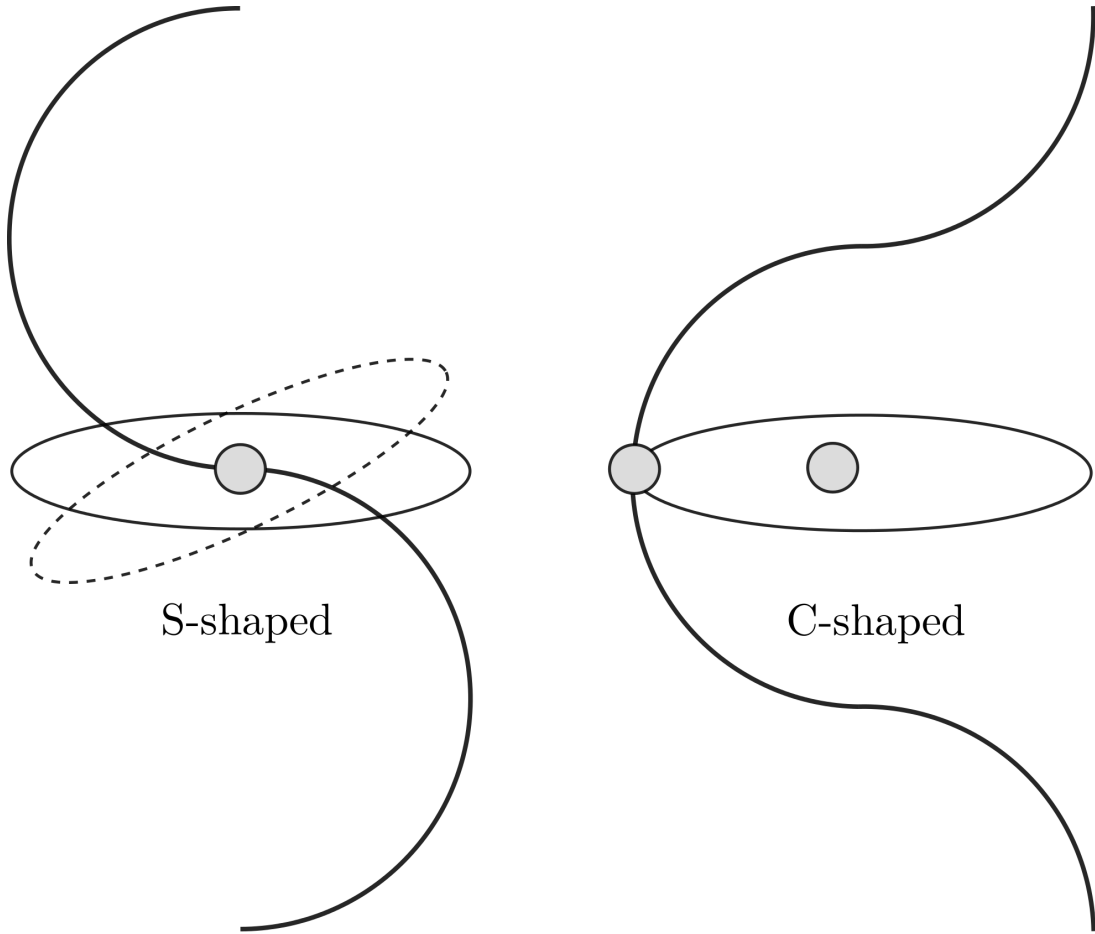
Figure 4.12: Sketch of the different types of sinusoidal jets. Left: S-shaped type caused by a precessing black hole. Right: C-shaped type caused by the rotation of a binary black hole system.

$$P = 10^{9.25} \alpha^{48/35} a^{5/7} (M/10^8 \, M_\odot)^{1/7} (\dot{M}/10^{-2} \, M_\odot \, \mathrm{yr}^{-1})^{-6/5} \, \mathrm{yr}, \qquad (4.1)$$

where P, M and $M_\odot$ are the precession period, mass and accretion mass of the spinning black hole, respectively, α is the dimensionless viscosity parameter, and a is the dimensionless specific angular momentum ($0 < a \leq 1$). We use the black hole mass estimated by Kuo et al. (2011) to compute the Eddington limited accretion rate:

$$\dot{M}_{\mathrm{Edd}} = \frac{4\pi G M m_p}{\eta c \sigma_{\mathrm{T}}}, \qquad (4.2)$$

where η is the efficiency (usually taken as $\eta \approx 0.1$) (Shakura & Sunyaev, 1973), M the mass of the black hole ($M \approx 8.5 \times 10^6 M_\odot$), σ_{T} the Thomson cross-section for electrons, m_p the proton mass, c is the speed of light, and G the gravitational

constant. Thus we get an accretion rate of $\dot{M}_{\mathrm{Edd}} = 0.18\,M_{\odot}\,\mathrm{yr}^{-1}$. We assume the accretion mass to be at least 10% of the Eddington limited accretion rate $\dot{M} = 0.02\,M_{\odot}\,\mathrm{yr}^{-1}$. If we now use our estimate for the period of precession and the accretion mass in Equation 4.1 we obtain that $\alpha^{48/35}a^{5/7} \approx 0.005$ which is within the range of the theoretical values ($\alpha^{48/35}a^{5/7} \approx 0.0002 \cong 1.0$).

4.6   Conclusions

In this study, RM maps of the nuclear outflows of NGC 4388 are presented. These maps were obtained from the C band-C array of the CHANG-ES project and were obtained through an RM synthesis analysis. We have found an asymmetry in the RM pattern of the southern part of the northern spot at the end of the northern nuclear outflow. The RMs vary from negatives values to positive values along the spot, in an area that is covered by $\cong 9$ beam areas. The profile of this spot can be interpreted as the magnetic field changing its direction along the line of sight. We suspect that this RM asymmetry could be due to the action of a precessing nuclear outflow of the northern and southern filaments with respect to the center of the galaxy. Another indication of the precession is the wiggling structure seen in the magnetic field vectors (RM-corrected) along the southern nuclear outflow. The RM of the southern nuclear outflow shows a change ($\cong 300\,\mathrm{rad\,m}^{-2}$) that indicates the presence of a structure in front of the spiral arms. After the change in orientation of the magnetic field vectors at the minor axis of the galactic disk, the change in the RM values is the second indication of a helical outflow structure. These evidences are only seen thanks to the radio polarization observations.

We adopted a precession model that gives similar structures in the morphology of the radio polarization filaments in the halo of NGC 4388. We developed an interactive tool to constrain the precession parameters from astronomical observations. Limited by the synchrotron life time of the CREs in the polarization filaments, which is estimated to be $t \cong (6.0 - 8.0) \times 10^6\,\mathrm{yr}$, the precession model estimates an inclination of $i \cong 15 - 50°$ towards the observer, an opening angle of $\phi \cong 3 - 10°$, and a position angle of $\chi \cong 13°$ on the plane of the sky. We also estimate a velocity of $1300 - 2300\,\mathrm{km\,s}^{-1}$ and $500 - 1000\,\mathrm{km\,s}^{-1}$ for the northern and southern parts of the nuclear outflow, which are consistent with the velocities obtained from Hα studies. The period of the precession is estimated to be $t \cong (3.5 - 4.5) \times 10^6\,\mathrm{yr}$.

With this set of values, the two polarization filaments seen in the radio data are well reproduced in extension and shape by a ballistic precessing outflow. Furthermore, the convolution of the model to match the resolution of the VLA reproduces the two spots seen to the north and south of the nucleus in both radio

polarization and total power.

To constrain the parameters of the precession model we have set the total time of ejection to the synchrotron life time of the electrons at the very end of the radio polarization filaments. We also used the position angle of the maser disk found in this galaxy to fix the present day position angle of the ejections. With this assumption the model can well reproduce the large scale polarization filaments. This indicates a connection between the structures seen at parsec scales next to the nucleus and the structures seen at kiloparsec scales of the polarization filaments.

As a second test, we have included the direction of the precessing outflow with respect to the observer along the line of sight. The convolution of this model map shows a similar structure to that seen in the RM map of the northern spot. The RM map of the radio observations shows an asymmetry from negative to positive RMs across the northern nuclear outflow. The map of the modeled precession shows the same structure at that point due to a change in the direction of the outflow. We interpret this similarity as the result of the magnetic field following the helical direction of a precessing nuclear outflow. This test gives an independent proof of precession being a plausible scenario in the nuclear outflow of this galaxy.

By extending the modeled outflow in time, we have found that the interaction between the ram pressure and the different loops of a precessing nuclear outflow can explain the complexity seen in the Hα outflow towards the north-east of the galaxy. The wide range of velocities, the position with respect to the disk, and the shape of these extended filaments in Hα could be the result of this interaction.

We have considered the interaction between a spinning black hole and a tilted accretion disk as a probable scenario for the origin of the precession in the nucleus of NGC 4388.

Further broad-band polarimetric observations will help to better compare the precession model with the radio data. Specially deeper observations that could reach lower signal to noise ratios and therefore enable a better RM analysis of the fainter parts along the nuclear outflow of NGC 4388. Also detection of polarized emission at lower frequencies (1 GHz, 600-300 MHz) would better constrain the RM values in Faraday space to resolve smaller changes in the magnetic field direction thanks to a wider λ^2 range at these frequencies.

Further Radio Observations of NGC 4388

In this chapter we present a new campaign of observations with the goal of confirm the new features that were found in NGC 4388 in the radio observations of CHANG-ES. To complement the C- and L-band observations of this galaxy we obtained new observations with the EVLA at S-band and X-band in full polarization and at similar resolutions.

We have also obtained new observations of this galaxy at lower frequencies with the Giant Metrewave Radio Telescope (GMRT) interferometer. The galaxy was observed at 610 MHz in Stokes I. These observations are used together with the EVLA datasets to perform an spectral index analysis in this galaxy.

Contents

5.1 Introduction

The polarization products of the C-band data set with both D and C configuration of CHANG-ES were of special interest since they have revealed extended diffuse emission that was never seen before in the halo of NGC 4388. In the previous chapters (see Chapters 3 and 4) we associated these new halo features to two independent processes with different origins. First we analyzed the extended polarization blobs that were detected above and underneath the spiral arms and concluded that they are part of a galactic wind event. Secondly, we studied the polarization filaments that extend from the galactic nucleus and saw that a precession of the nuclear outflow is a possible explanation for the complexity seen in these features. In both cases we have concluded that further observations are needed in order to confirm these ideas. Therefore, the main motivation of this new work is to confirm the theories exposed in the previous chapters about the radio halo of NGC 4388.

5.2 New X-band and S-band Observations

5.2.1 Motivation

In order to compare these new observations with the CHANG-ES maps, the ideal setups are S-band ($2.0 - 4.0$ GHz) B-configuration and X-band ($8.0 - 12.0$ GHz) C-configuration, both with an angular resolution of $\sim 2.1''$, which is better than the $\sim 3.5''$ of the C-band C-configuration of the CHANG-ES sample. We attempted to mitigate the decrease of the flux density (in this case it decreases by a factor of ~ 3 with respect to the CHANG-ES C-band C-configuration dataset) by integrating over more time. S-band was also needed in the C-configuration to study the flux density of the extended emission from the galaxy disk.

In the C-band polarization maps, we did not detect polarization in half of the northern nuclear outflow. X-band observations can help us to study the details of the entire jet in polarization since the Faraday depolarization increases with λ^4 and this can show if there is Faraday depolarization of the foreground disk. With the polarization emission provided by the X-band observations we could be able to trace the magnetic field vectors of the parts close to the disk and find out whether the vectors are parallel to the entire nuclear outflow. This frequency is also very important for showing more details about the southern jet of NGC 4388 since we could see more polarization close to the disk. We can combine the X-band data with the C-band data to improve the orientation of the magnetic vectors of this complex structure.

On the other hand, observing at S-band could clarify whether the depolarization of the northern nuclear outflow takes place in the disk or within the outflow

itself. To confirm the asymmetry seen in the RM map of the northern spot we need to increase the resolution in Faraday space given by $\sqrt{3}(\Delta\lambda^2(S/N))^{-1}$, by increasing $\Delta\lambda^2$. L-band would give better Faraday resolution, however, probably due to strong depolarization effects, polarization at L-band in the CHANG-ES observations was not detected in that region. Also, NGC 4388 is very close to the cluster center which makes the process of cleaning challenging. In this situation, the theoretical noise is hardly reached for the L-band data set from CHANG-ES for this galaxy. From other galaxies in the CHANG-ES sample, we know that the theoretical noise for L-band is $30\,\mu$Jy beam^{-1}, but in the case of NGC 4388 the rms noise is ~ 10 times higher. The presence of M 84 and M 87 introduces artifacts in the image and therefore increases the noise. The effect of M 84 is specially severe since it is situated at the edge of the primary beam so the disrupting effect on the phase center of the observation interferes with the NGC 4388 region. The polarization will also be affected by this problem. In fact we were not able to detect polarization at L-band in the C and D configurations datasets and therefore, it was impossible to perform an RM synthesis analysis with this datasets. This is why S-band observations are of crucial interest since we could discern the causes for the non-detection of polarization emission at L-band.

In C-band the noise introduced by M 87 and M 84 is weaker, resulting in images with great detail and sensitivity at this band. However, the resolution of C-band in Faraday space is not good enough to look for different components in the polarization cube given by RM synthesis. In S-band, the wide band receiver can increase the RM precision to $\simeq 60\,\text{rad/m}^2$. In the C-band polarization cubes the resolution in Faraday space is $\sim 1000\,\text{rad/m}^2$ so the precision in RM is much better at S-band. It is also possible to combine both bands in a single RM synthesis run to improve the resolution in Faraday space.

Detecting polarization at S-band can also help us to better study the southern part of the nuclear outflow. Apart from improving the Faraday resolution, with S-band we can improve the orientation of the magnetic vectors to better characterize the wiggling structure shown by the southern part of the nuclear outflow in the C-band polarization images. The orientation of the magnetic vectors in the northern part of this outflow can also be refined with this observations.

5.2.2 Observations Setup

We observed NGC 4388 at S-band in BnC-configuration of the VLA ($\sim 2.1''$ of resolution) to detect the extended emission and to gain resolution in Faraday space. We also observed NGC 4388 at X-band in the C-configuration to check the depolarization of the jet close to the galaxy disk ($\sim 2.1''$ resolution).

The polarized flux density detected in the C-band C-configuration is about $130\,\mu$Jy in the northern spot, corresponding to $31\,\mu$Jy in X-band C-configuration

Table 5.1: Details of S-band VLA observations

Date of observations	2015 Feb 4
Array	BnC
Central frequency	3.0 GHz
Bandwidth	2.0 GHz
Spectral channels	64
Channel width	2 MHz
Spectral windows	16
Primary calibrator	3C286
Secondary calibrator	J1254+1141
Leakage calibrator	J1407+2827

Table 5.2: Details of X-band VLA observations

Dates of observations	2014 Oct 19 and 26
Array	C
Central frequency	10.0 GHz
Bandwidth	4.0 GHz
Spectral channels	64
Channel width	2 MHz
Spectral windows	48
Primary calibrator	3C286
Secondary calibrator	J1254+1141
Leakage calibrator	J1407+2827

and $81\,\mu$Jy and $900\,\mu$Jy (considering a spectral index of -0.8 and the change of sensitivity with the beam size) in the case of S band for BnC-configuration (note that the confusion level in polarization is much lower than in total intensity). To reach an S/N ratio of 10, according to Equation (1) in the VLA Status Summary, we need 1.31 hours (1.16 hours on-source) of total observation time for S-band BnC-configuration and 3.57 hours (2.83 hours on-source) for X-band C-configuration. Altogether, the total requested time was 5.47 hours. In the case of S-band we took into account that both galaxies are sharing calibrators so the time expended was reduced. The intention is to combine configurations to improve the S/N. For both bands we considered that 15% of the bandwidth could be affected by RFI and in the case of X-band we took into account that the use of the 3-bit digital samplers gives a 15% of sensitivity penalty.

In Tables 5.1 and 5.2 we show the main details of these new VLA observations.

5.2.3 Calibration of S-band and X-band

For the calibration and imaging of these data sets we have followed the same procedure as for the CHANG-es C-band and L-band datasets (see Section 2.2).

In the case of the X-band observations, we have three different days observations from which two of them had to be removed due to bad quality data. The rms noise reached is $20\,\mu$Jy beam^{-1}, higher than the theoretical value.

Although we expect to have poor resolution in Faraday space for the X-band data, RM synthesis has been applied to both datasets to avoid the bandwidth depolarization.

5.2.4 Results at S-band

In Figure 5.1 we show the total power map obtained for S-band with the BnC configuration of the VLA. This map was obtained with a robust parameter of 0. With a robust 2 cleaning the noise increases considerably probably due to gaps in the uv coverage. The resolution of the final radio image is $2.10'' \times 1.69''$ and this allows us to see both spiral arms and the nuclear outflow. There is no detection of the radio features seen at C-band of the CHANG-ES datasets in the halo.

Regarding polarization, there is only a clear detection in the southern spot. The magnetic vectors are orientated mostly towards the south. This is consistent with the CHANG-ES image of the L-band B-configuration dataset where we only detected a faint polarized emission at the same spot (see Figure 2.2). In Figure 5.2 we show the same total power contours but now on top of polarized emission obtained with RM synthesis to avoid the band-width depolarization. In this case we also detect the southern spot, but also some emission from the southern

Figure 5.1: Data of NGC 4388 at 3.0 GHz (S-band) in BnC-configuration of the VLA. Resolution is $2.10'' \times 1.69''$. Total intensity in contours together with magnetic field vectors overlaid on a color scale of the polarized intensity. The contour levels are $(3, 4, 6, 12, 24, 48, 96, 192, 394, 1000) \times 8.0\,\mu\mathrm{Jy\,beam^{-1}}$ with an rms noise of $8.0\,\mu\mathrm{Jy\,beam^{-1}}$.

inter-arm region. The vectors showed in this case are Faraday corrected and their orientation is in agreement with what we see in the C-band polarization images.

Similarly to what we saw previously at L-band, there are no signs of the polarized emission in the northern spot, which for the case of C-band is very strong. From this non-detection we could conclude that there is a strong depolarization at low frequencies in the northern part of the nuclear outflow due to the position of this part of the outflow behind the disk of the galaxy. On the other hand, the southern spot does not suffer of that much depolarization because it extends in front of the southern spiral arm.
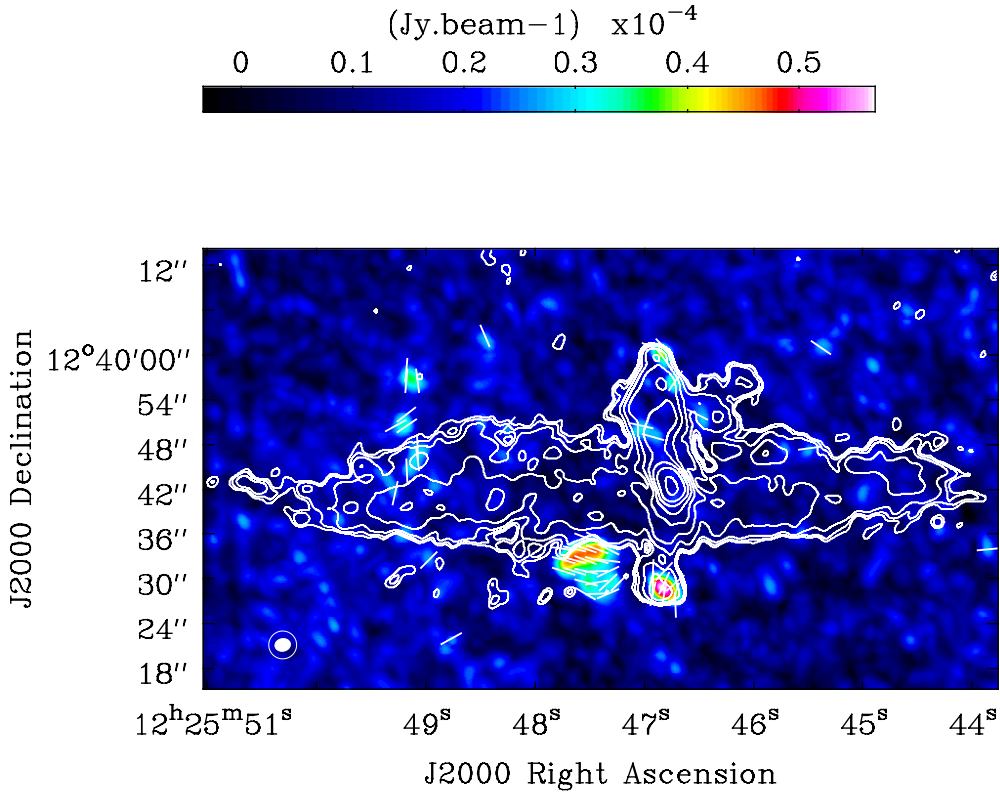
Figure 5.2: Total intensity contours map overlaid on a polarized intensity map plus Faraday corrected magnetic vectors. The resolution of all maps is $3.00'' \times 3.00''$. The contour levels are $(3, 4, 6, 12, 18, 24, 48, 96, 192, 384) \times 15.0 \,\mu\mathrm{Jy\,beam}^{-1}$ with an rms noise of $15.0 \,\mu\mathrm{Jy\,beam}^{-1}$. The polarization was obtained with RM synthesis and the magnetic vectors are Faraday corrected.

5.2.5 Results at X-band

In Figure 5.3 we show the total power map obtained for X-band with the C configuration of the VLA with a resolution of $2.38'' \times 1.83''$ and a rms noise of $20 \,\mu\mathrm{Jy\,beam}^{-1}$. Although the noise is higher than expected due to the use of one single day of observation, we detect both spiral arms and the nuclear outflow. The polarized emission is shown in Figure 5.4. This map was produced using RM synthesis to avoid the band-width depolarization and to correct the magnetic vectors for Faraday rotation. Every spectral window was cleaned with a robust parameter of 2 to ensure more sensitive to the extended emission. We clearly detect polarized emission in the northern spot with an orientation of the Faraday corrected magnetic vectors towards the north-west. The southern spot is not detected probably due to high noise of the map ($16 \,\mu\mathrm{Jy\,beam}^{-1}$). There is polarized emission at the southern inter-arm region as seen at C-band and partly
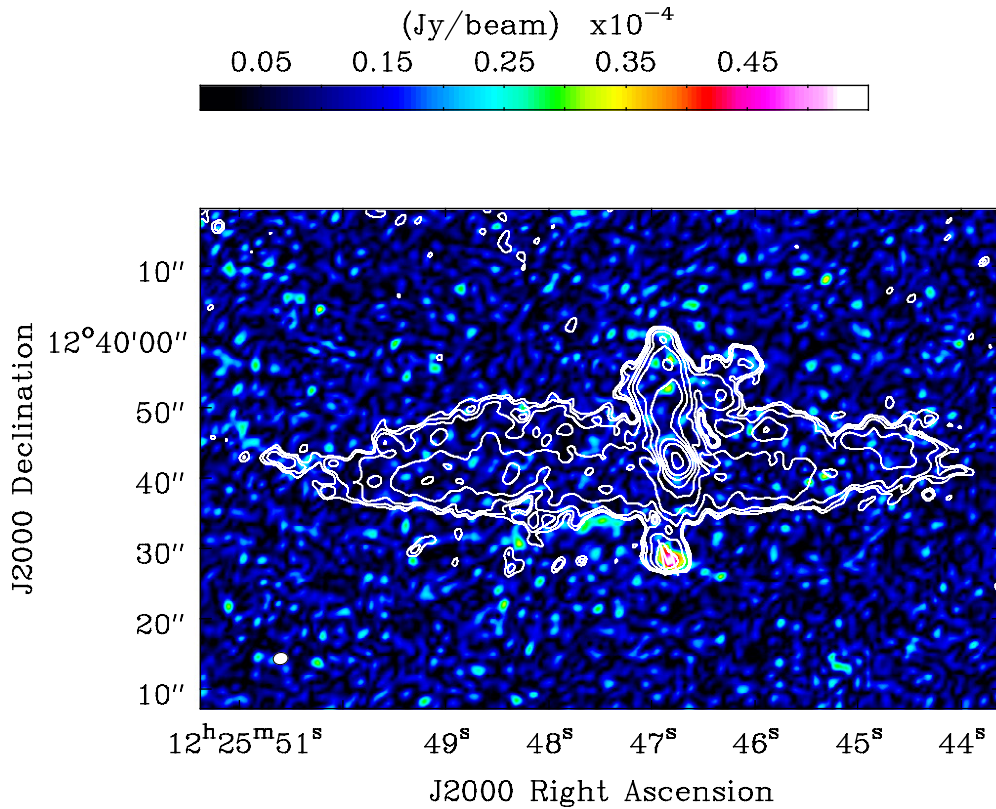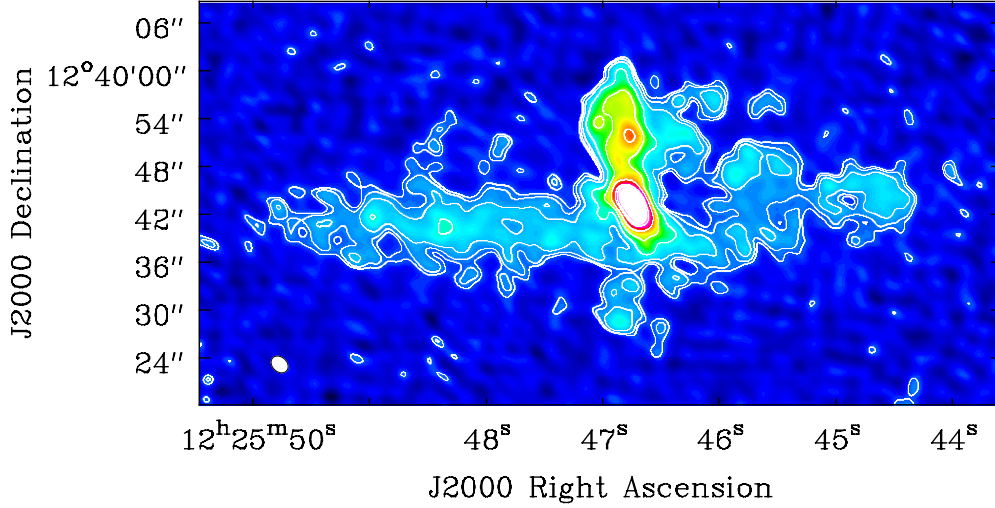
Figure 5.3: Data of NGC 4388 at 10.0 GHz (X-band) in C-configuration of the VLA. Resolution is $2.38'' \times 1.83''$. Total intensity in contours together with magnetic field vectors overlaid on a color scale of the polarized intensity. The contour levels are $(3, 4, 6, 12, 24, 48, 96, 128) \times 20.0\,\mu\text{Jy beam}^{-1}$ with an rms noise of $20.0\,\mu\text{Jy beam}^{-1}$.

at S-band. The orientation of the corrected magnetic vectors is parallel to the major axis of the galaxy like in both C-band and S-band images.

The fact that we did not detect polarized emission along the whole nuclear outflow tells us that the Faraday depolarization might still be strong in this region although for X-band, the Faraday rotation is not as strong as at lower frequencies. The nucleus of the galaxy also shows no polarization at this frequency band.

We performed a cleaning using a robust weighting of -2 to ensure that we observe the northern nuclear outflow with the higher resolution possible. This gives us the highest resolution of the whole sample ($1.59'' \times 1.47''$). In Figure 5.5 we show a comparison between the robust -2 image at X-band and the contours of the southern nuclear outflow at C-band with a robust 0 weighting. The X-band shows a wiggling structure similar to the one showed in Section 3.4.3 where we discussed the apparently wiggling structure of the magnetic field vectors in the C-band dataset from CHANG-ES. Both filamentary structures are similar in length and width. This similarities between both wiggling features of both frequency
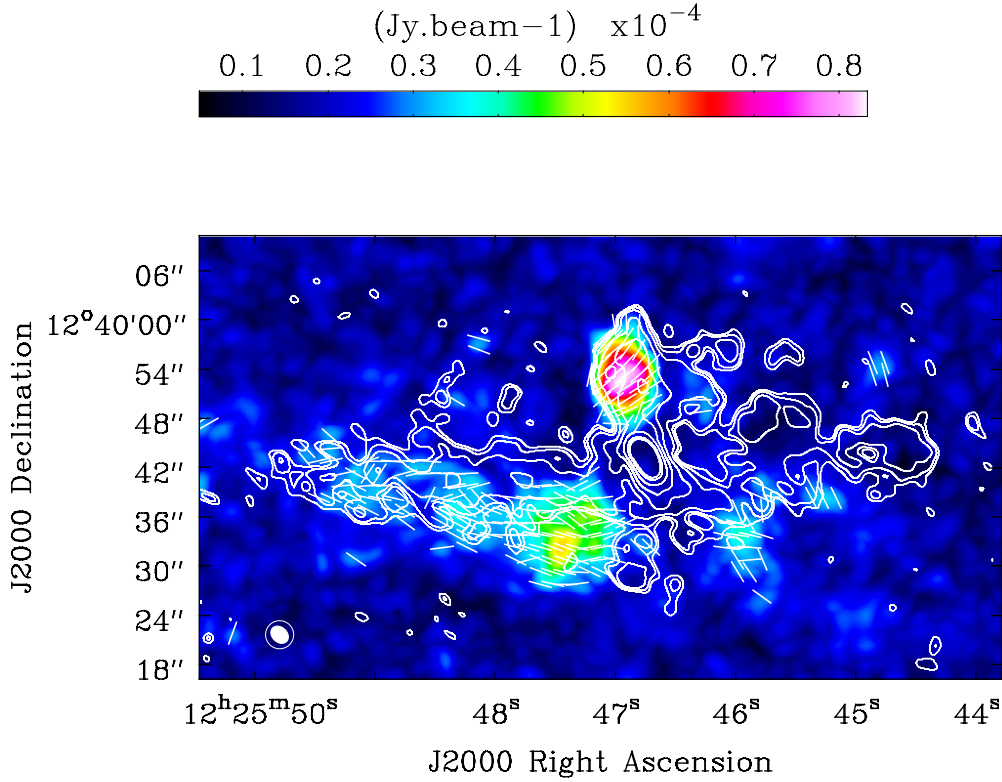
Figure 5.4: Total intensity contours map at $10.0\,\mathrm{GHz}$ (X-band) in C-configuration of the VLA overlaid on a polarized intensity map plus Faraday corrected magnetic vectors. The resolution of the total intensity map is $2.38'' \times 1.83''$. The contour levels are $(3, 4, 6, 12, 24, 48, 96, 128) \times 20.0\,\mu\mathrm{Jy\,beam}^{-1}$ with an rms noise of $20.0\,\mu\mathrm{Jy\,beam}^{-1}$. The polarized emission map was made using RM synthesis. The noise of the polarized emission map is $3.3\,\mu\mathrm{Jy\,beam}^{-1}$.

bands suggest that the two structures are related. In fact, both structures appear to be antisymmetric with respect to the galactic nucleus. This fits well with the precession scenario exposed in Chapter 4 since the precession causes the S-shaped outflow as discussed in Section 4.5. Also, if we compare the orientations of the magnetic vectors at the same position in the C-band observations, they turn towards the same orientation as the filament seen in X-band, suggesting that those magnetic vectors have some relation with the polarization vectors of the northern spot seen at C-band (Section 3.4.3).
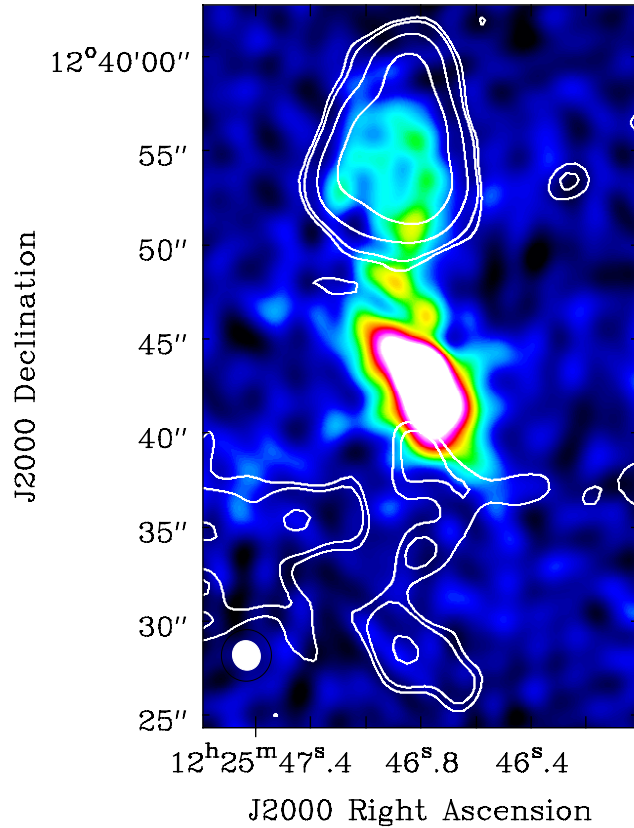
Figure 5.5: Total intensity of X-band (10.0 GHz) C-configuration with a resolution of $1.59'' \times 1.47''$ over contours of C-band (6.0 GHz) C-configuration $((3, 4, 8, 16, 32, 64, 128) \times 4.5 \, \mu\text{Jy beam}^{-1})$.

5.3   GMRT at 610 MHz

5.3.1   Motivation

Observing at low radio frequencies (< 1 GHz) is crucial to study the synchrotron emission of CREs in the halo of galaxies since at this frequency domain, galaxies are dominated by the non-thermal component of the spectrum. The extension of a radio halo depends on the CREs propagation and their energy losses and therefore on the frequency of observation. The change of size in halo can be best tested in observations of edge-on galaxies because we get to see their entire radio halo. The observations at low frequencies of these kind of galaxies are of crucial interest to understand the physics of CREs propagation (Heesen et al., 2009).

Table 5.3: Details of GMRT observations

Date of observations	2016 Jan 2
Central frequency	610.0 MHz
Bandwidth	32.0 MHz
Spectral channels	512
Channel width	62.5 kHz
Primary calibrator	3C286 and 3C147
Secondary calibrator	1123+055 and 1330+251

The main goal of these observation campaign is to confirm the origin of the polarized blobs observed in the radio halo of NGC 4388. The detection of a extended radio halo will allow a spectral index distribution analysis of these areas.

In the case of galactic winds, the radio continuum emission could arise due to old relativistic plasma having steep spectral index ($\alpha_{nt} \approx 1$) due to synchrotron and/or inverse-Compton losses. Such emission are difficult to observe at higher frequencies. Comparing the radio continuum emission at these low frequencies to the existing CHANG-ES data, and to the ionized gas through Hα and X-ray data and H I modeling (Vollmer & Huchtmeier, 2003) is crucial to understand these structures.

At such low frequencies, the synchrotron emission dominates the radio spectrum (Basu et al., 2012). This could allow us to confirm the magnetic field in the halo of the galaxy. At the frequencies of the CHANG-ES datasets the free-free emission adds errors to the magnetic field estimation. The study of radio continuum spectrum at the position of the polarized features and the variation of spectral index in the halo will enable us to measure the velocities of the galactic wind and the nuclear outflow. This observations are therefore crucial in supporting the two scenarios.

5.3.2   Observation Setup

We observed NGC 4388 with the Giant Metrewave Radio Telescope (GMRT) at 610.0 MHz in total intensity. We got a total time of 10 hours at 610.0 MHz that together with our observations at higher frequency of VLA help us to better understand the radio morphology and CRE energy loss processes in the halo of this galaxy. This is the first observation of NGC 4388 at 610.0 MHz.

There are archival 330.0 MHz data observations of GMRT for a total on-source time of $\sim$ 1 hour. The rms noise reached for such setup is $\sim 400 - 500\,\mu$Jy beam^{-1}, which is not enough to address our scientific goals. Also, with that short observation time, the uv-coverage is not well sampled and this gives

rise to deconvolution errors that distort the final image.

The GMRT at 610 MHz provides an angular resolution of $\sim 6''$ and a theoretical noise of $\sim 20\,\mu\text{Jy beam}^{-1}$ in a full synthesis run ($\sim 8\,\text{hours}$ on source). This would be enough to detect the faintest regions of the radio halo at 3σ level.

5.3.3   Calibrations of the GMRT Dataset

The calibration of these data were performed using the NRAO Astronomical Image Processing System (AIPS[1]), a software package to calibrate and image interferometric observations. Specifically, we have used the AIPS-31DEC04 version. The main reason to use this software was because of a better performance when cleaning large field of view images and a faster response when doing self-calibration of sources that are far from the phase center of the observation.

In Table 5.3 we show the details of these new observations. Due to the long exposure time of the total observation, we made use of two different flux calibrators -3C286 and 3C147- so we could calibrate the galaxy scans by making two groups of scans with two individual runs of flux calibration. The same had to be done for the chosen phase calibrators (1123+055 and 1330+251). In total, we observed the flux calibrators and the phase calibrators for $\sim 16\,\text{minutes}$ and $\sim 56\,\text{minutes}$, respectively.

The cleaning process was performed by dividing the field of view of the observation into different areas with the same extension. We used natural weighting to be more sensitive to the extended emission. After cleaning the calibrated data, several runs of self calibration were needed in order to get rid of phase errors mainly introduced by M 87 and M 86. Similarly to what we encountered in the L-band datasets of CHANG-ES, the presence of many strong radio sources in the Virgo cluster makes cleaning at low frequencies challenging and the theoretical noise is hardly reached.

5.3.4   Results on the GMRT Observations

The rms noise reached in the final image (see Figure 5.6) is substantially higher ($\sim 170\,\mu\text{Jy beam}^{-1}$) than the theoretical noise. The obtained resolution ($6.50'' \times 4.53''$ with PA = 69.21°) allows us to distinguish the spiral arms and both northern and southern nuclear outflows. We also detect extended and diffuse radio emission towards the north-eastern part of the galactic disk, that coincides in space with the Hα outflow studied by Yoshida et al. 2004. Two new blobs of total power align towards the southern part of the halo.

In Figure 5.7 we show a comparison between the GMRT 610 MHz final image and the polarized emission at C-band from CHANG-ES. Although there are no

---

[1]http://www.aips.nrao.edu/index.shtml
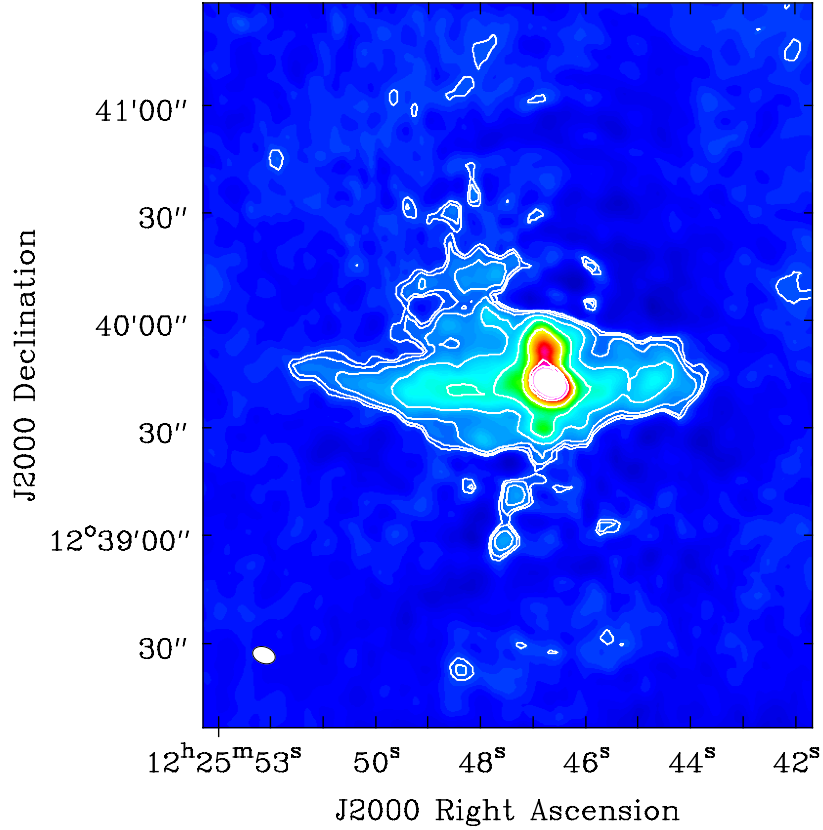
Figure 5.6: Total power map of GMRT at 610.0 MHz on color scale overlaid with contours of total power of $(3, 4, 6, 12, 24, 48, 96, 128) \times 170 \, \mu$Jy beam^{-1} and a resolution of $6.50'' \times 4.53''$ with PA $= 69.21°$.

detections of the polarization blobs seen in the polarization observations of VLA at C-band, we see some 4σ contours in the same region. The extended emission seen towards the north-eastern part of the halo coincides with the northern polarization filament seen at C-band. This detection confirms the detection of this filamentary structure in radio total power. However, there is no detection of the southern polarized filament in the southern part.

In Figure 5.8 we show the spectral index map between the GMRT 610 MHz data and the VLA 6.0 GHz D plus C configuration dataset. We clearly detect a difference in the spectral indices of northern and southern nuclear outflows. Also, the values of spectral index in the north-eastern outflow are steeper than the ones in the spiral arms because of the aging of CREs in the halo.
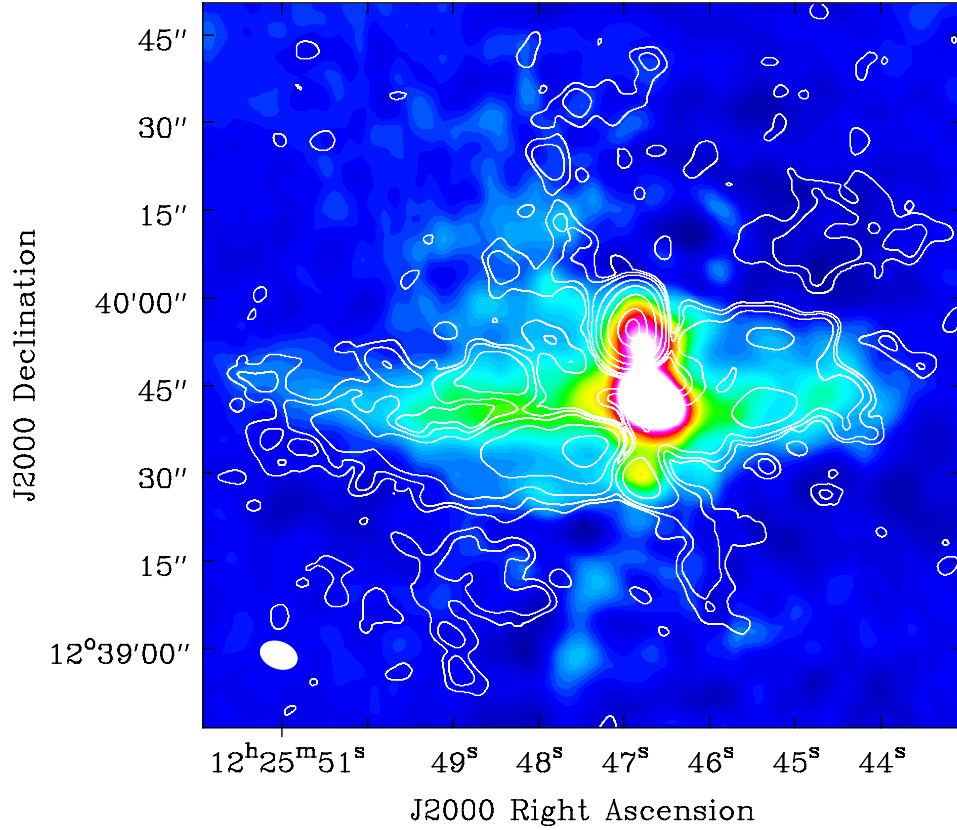
Figure 5.7: Total power map of GMRT at $610.0\,\mathrm{MHz}$ ($6.50'' \times 4.53''$ with $\mathrm{PA} = 69.21°$) compared to contours of polarized emission of C-band ($6.0\,\mathrm{GHz}$) C-configuration ($(3, 4, 6, 12, 24, 48, 96, 128) \times 2.3\,\mu\mathrm{Jy\,beam}^{-1}$) and a resolution of $5.33'' \times 5.33''$.

5.4   Spectral Distribution Analysis

We have extended the CHANG-ES observations with three more frequencies that extend the radio flux measurements to higher frequencies (X-band 10 GHz) and to lower frequencies (GMRT 610 MHz). The S-band (3 GHz) filled the gap between L-band (1.5 GHz) and C-band (6 GHz) existing in the survey. With this wide range of frequencies we can estimate the spectral index distribution of this galaxy with much higher precision than from an in-band spectral index.

In particular we are interested in the behavior of the spectral index distribution of the nuclear outflows for which we have estimated different physical parameters through the analytical model presented in Chapter 4. Thanks to the resolution of the new observations we can track the flux density of both northern
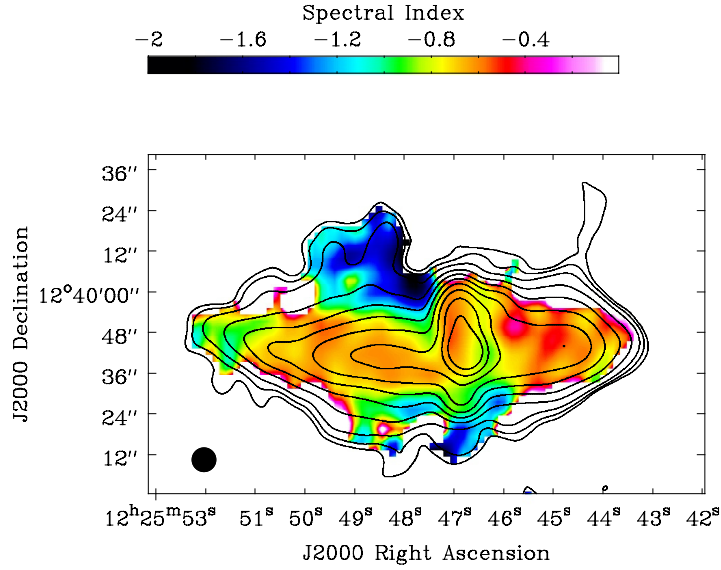
Figure 5.8: Spectral index map (in color scale) between 610.0 MHz (GMRT) and 6.0 GHz (VLA) overlaid on total power contours of C-band (6.0 GHz) C- plus D-configuration of $((3, 4, 6, 12, 24, 48, 96, 192, 384, 768) \times 6.7\,\mu\mathrm{Jy\,beam}^{-1})$ with a resolution of $7''$.

and southern nuclear outflow from X-band to GMRT frequencies. We have measured the flux density in the northern and southern nuclear outflows of the total power maps of each band (see Figure 5.9). For this task we had to smooth all maps to the same beam size ($30''$) and select a common area that excludes the nuclear emission as well as the spiral arms emission. From the linear fitting of all data points we find a flatter spectral index in the case of the northern outflow ($\alpha_{\mathrm{north}} = -0.55 \pm 0.01$) than the southern one ($\alpha_{\mathrm{south}} = -1.00 \pm 0.01$).

The spectral index could be flatter in northern outflow due to the contribution of thermal electrons. We can estimate the thermal fraction difference between both parts of the nuclear outflow from the following expression:

$$I_{\mathrm{tot}} = A \cdot I_{\mathrm{syn}} + B \cdot I_{\mathrm{th}} = A \cdot \nu^{-\alpha_{\mathrm{syn}}} + B \cdot \nu^{-0.1}, \tag{5.1}$$

where I_{th} is the thermal distribution to the total radio intensity flux, I_{syn} is the non-thermal distribution to the total radio intensity flux, A and B are constants, and α_{syn} is the spectral index. Figures 5.10 and 5.11 show the comparison between thermal and non-thermal contributions in both cases. This analysis also shows a negligible thermal contribution in the northern part of the nuclear out-
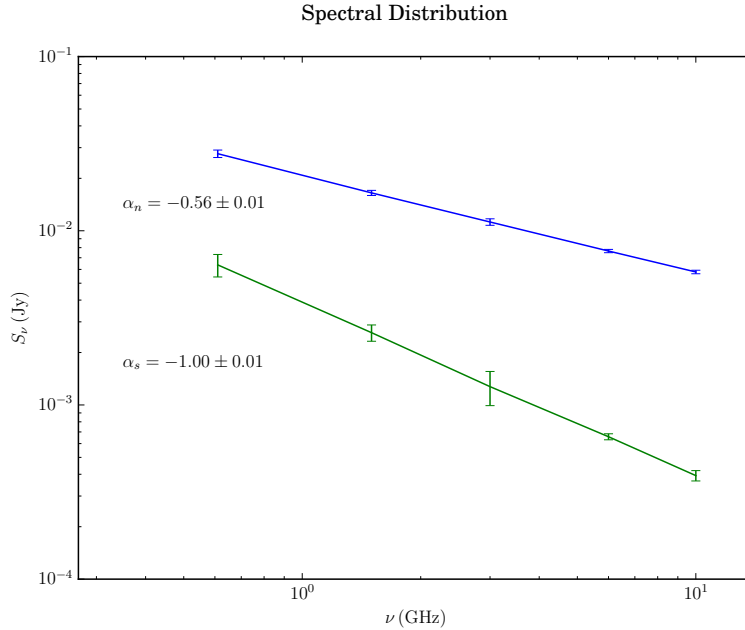
Figure 5.9: Spectral energy distribution of the northern (blue solid line with error bars) and southern (green solid line with error bars) nuclear outflows.

flow.

Since the thermal contribution is very small in both outflows, the difference in the spectral index must come from a different reason. On possibility could be a difference in velocities between the northern and the southern nuclear outflows. The action of the ram pressure would increase the velocity of the northern outflow and decrease the velocity of the southern outflow giving rise to different spectral indices.

5.5   Analysis of the Nuclear Outflow Velocities

NGC 4388 is moving supersonically through the ICM of Virgo at $\sim 1700\,\mathrm{km\,s^{-1}}$. We consider now that both spots are lobes produced by the interaction between nuclear jets of the AGN and the ICM. This interaction creates a shock front that can accelerate cosmic particles to relativistic speeds due to the diffusive shock acceleration (DSA) mechanism (Blandford & Eichler, 1987; Brunetti & Jones, 2014). The jet injects CREs into the ICM and their energy obtain a power-law distribution. The spectral index of an astrophysical shock is related to the Mach number ($\mathcal{M}$) of the shock in the following way (Blandford & Eichler, 1987; Brunetti & Jones, 2014):

Figure 5.10: Spectral distribution of the northern nuclear outflow. The blue points with error bars represent radio fluxes points and the green solid line is the fit curve. Blue and red solid lines represent the non-thermal and thermal flux densities of the total emission, respectively. A and B refer to the constants values in Equation 5.1 and α is the spectral index.

$$\gamma_{inj} = 2\alpha_{inj} + 1 = 2\frac{\mathcal{M}^2 + 1}{\mathcal{M}^2 - 1}, \tag{5.2}$$

where γ_{inj} and α_{inj} are the spectral index of the CRE energy spectrum and the spectral index of the synchrotron spectrum, respectively. From this equation we can estimate the relation between the spectral index and the Mach number:

$$\mathcal{M} = \sqrt{\frac{\alpha_{inj} + 1.5}{\alpha_{inj} - 0.5}}, \tag{5.3}$$

which is valid for CRE ages smaller than the synchrotron lifetime ($t_{\mathrm{CRE}} < t_{syn}$). Under these conditions, we estimate Mach numbers of $\mathcal{M}_{\mathrm{north}} = 6.40 \pm 0.30$ ($\alpha_{\mathrm{north}} = -0.55 \pm 0.01$) for the northern spot and of $\mathcal{M}_{\mathrm{south}} = 2.30 \pm 0.02$ ($\alpha_{\mathrm{south}} = -1.00 \pm 0.01$) for the southern one.

In Chapter 4 we estimated speeds for the nuclear outflows of $500 - 1000\,\mathrm{km\,s^{-1}}$ for the southern part of the nuclear outflow and $1300 - 2300\,\mathrm{km\,s^{-1}}$ for the northern one. The ICM ram pressure might be responsible for a more elongated northern nuclear outflow. Now we can check if the velocities obtained from the
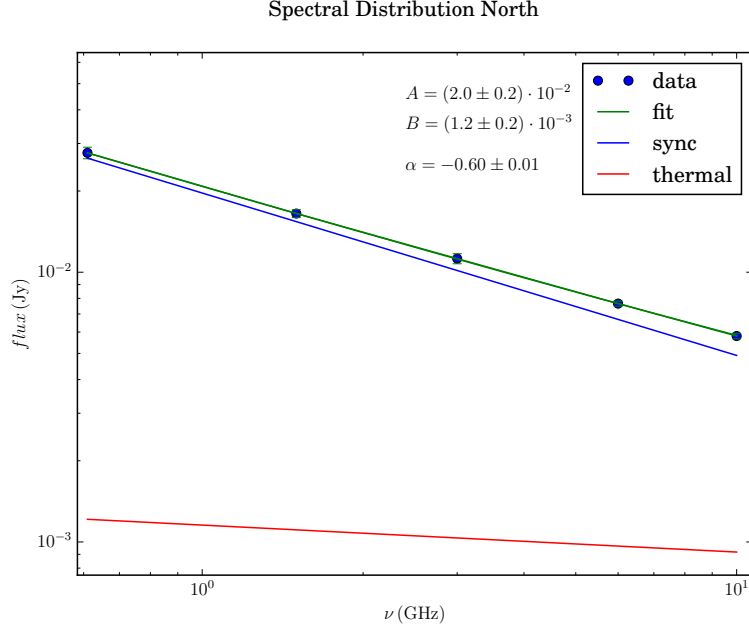
Spectral Distribution South
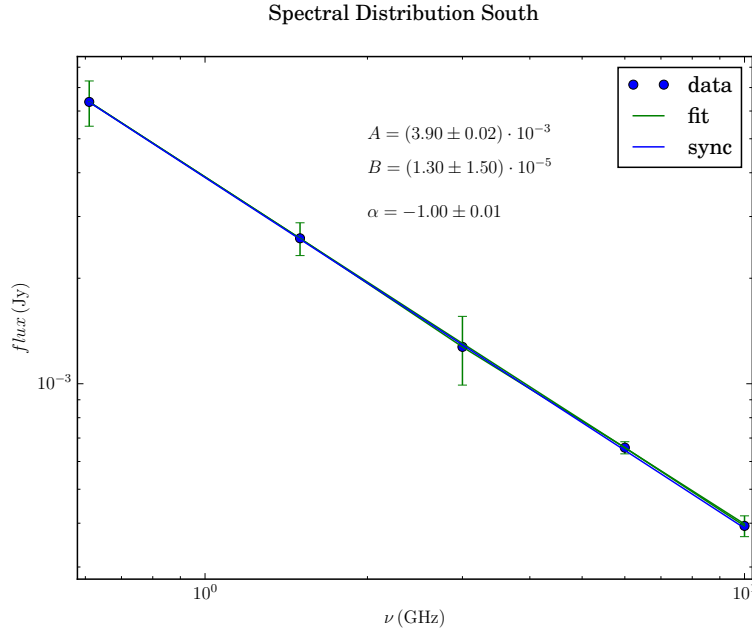
Figure 5.11: Spectral distribution of the southern nuclear outflow. The blue points with error bars represent radio fluxes and the green solid line the is fit curve. The blue solid line represents the non-thermal flux density of the total emission. A and B refer to the constants values in Equation 5.1 and α is the spectral index.

precession model are consistent with our estimates of the Mach number at the spot shocks.

The Mach number depends on the velocity of the outflow and on the sound speed of the medium in which the shock occurs. The difference in the Mach number between northern and southern spots could therefore be caused by a different outflow velocities. We now consider these scenario to explain the different Mach numbers.

5.5.1   Different Outflow Speeds

In Section 4.4.5 we discussed the possible interaction between the precessing nuclear outflow and the ICM ram pressure. The polarization filaments are different in size so there must be differences in their intrinsic properties. The parameters that describe the precession model (see Section 4.4.1) could be different for northern and southern outflows. If we fix the total time of the ejection according to the synchrotron life time, other parameters can vary in order to get the different size between both outflows. Therefore, the difference in the spectral indices obtained for the northern and southern spots would be the second independent indication of the interaction between the ICM and the nuclear outflow

of NGC 4388.

If we assume the sound speed to be homogeneous in the halo of the galaxy, this results in a difference in the velocity between both spots in order to see a difference in the Mach numbers. From X-ray observations we know that the sound speed is $c_{\mathrm{ICM}} \cong 750\,\mathrm{km\,s^{-1}}$ for the ICM (Böhringer et al., 1994). However, from the precession model we estimate that both spots are still within the halo of the galaxy and consequently the sound speed of the ICM should not be used. We can deduce the sound speed within the halo of the galaxy from our halo pressure analysis from Section 3.4.5. A thermal pressure of the hot gas in the halo of $P_{\mathrm{th}} \cong (3 \pm 2) \times 10^{-12}\,\mathrm{dyn\,cm^{-2}}$ and using a density of $n \cong 4 \times 10^{-3}\,\mathrm{cm^{-3}}$ and a temperature of $kT = 0.5\,\mathrm{keV}$ give a sound speed of $\sim (210 \pm 70)\,\mathrm{km\,s^{-1}}$. This value is smaller than the one observed for the ICM and larger than the average value for the ISM and hence is a reasonable sound speed for the halo of a galaxy.

We can now compute the velocities of the nuclear outflow with the Mach numbers obtained from our spectral index analysis. This results in velocities of $v_{\mathrm{north}} \cong (1300 \pm 500)\,\mathrm{km\,s^{-1}}$ and $v_{\mathrm{south}} \cong (500 \pm 170)\,\mathrm{km\,s^{-1}}$ for the northern and the southern nuclear outflows, respectively. These velocities are in good agreement with the ones computed from the precession model of Section 4.4.1.

The different velocities found at the spots when assuming the same sound speed could have two explanations. Firstly, as mentioned already in Section 3.4.1, there could be an internal asymmetry in the ISM close to the nucleus that makes unequal the distribution of the ejection energy. This might explain the reason why the northern nuclear outflow shows a stronger radio emission. The velocity would also be different since one part of the outflow would interact stronger with the ISM environment (Perucho et al., 2014).

Secondly, if the internal asymmetries are not high, ram pressure could be responsible for the different distribution of the nuclear outflows. In this situation the southern outflow would be suppressed by the interaction with the ICM and its velocity would decrease as it reaches the outskirts of the halo. In contrast, the northern nuclear outflow would increase its velocity towards the same direction of the ram pressure action. It seems that the spots are areas of the outflow where the effect of the ram pressure starts to be more determinant since both spots are at the same distance from the nucleus of the galaxy. The interaction with the ICM environment is then more obvious in the polarization filaments, where the elongated structures extend already out of the galactic halo and there is a clear difference in length between northern and southern polarization filaments. This scenario fits well with the idea exposed in Section 4.4.5 where we discussed the possible interaction between the ram pressure and the precessing nuclear outflow as a responsible for the complex Hα structures seen in the halo of NGC 4388. In this scenario the nuclear outflows are at some point being accelerated. If we look at the gradients between velocities of of northern and southern outflows,

there is a discrepancy with the model. The precession model predicts a gradient of $\sim 400\,\mathrm{km\,s^{-1}}$ for a range of inclinations of $20 - 40°$. The gradient seen from the radio spectral index analysis is $\sim 800\,\mathrm{km\,s^{-1}}$. This discrepancy suggests that the acceleration must be causing the northern outflow to be faster than what the model predicts and slower in the case of the southern outflow. This acceleration parameter is missing in the model but it would explain the discrepancy between the velocity gradients between the northern and southern outflows.

The fact that both halves of the nuclear outflow have different velocities has direct implications on the morphology of the radio structure as seen on the plane of the sky. The precession model must be modified in order to fit both parts of the outflow at the same time. In principle, one could think that if the velocities are different, the inclinations also differ from the northern and southern extensions. However, if we set different inclinations in the precession model, the opening angle parameter ϕ must also be different. This is hard to explain since both polarization filaments have similar shapes and the wiggling structure seen along the inner part of the nuclear outflows (see Section 5.2.5) are also similar.

As a consistency check, we can now estimate the inclination of the nuclear outflow according to the lengths measured on the plane of the sky of both halves of the radio structure: $\sim 5.9\,\mathrm{kpc}$ for the northern half and $\sim 2.9\,\mathrm{kpc}$. The difference in Mach numbers is:

$$\mathcal{M}_{\mathrm{north}} - \mathcal{M}_{\mathrm{south}} = \frac{v_{\mathrm{north}} - v_{\mathrm{south}}}{c_{\mathrm{sound}}}, \tag{5.4}$$

where c_{sound} is the speed of the sound in that medium, and the velocities (v_{north} and v_{south}) of the outflow must be computed taken into account the inclination of the outflow. Assuming a total time of ejection according to the synchrotron lifetime of $(6.0 - 8.0) \times 10^6\,\mathrm{yr}$, the inclination is obtained from the following expression:

$$\sin(i) = \frac{\Delta l}{t} \cdot \frac{1}{\Delta \mathcal{M}\, c_{\mathrm{sound}}} \tag{5.5}$$

where Δl and $\Delta \mathcal{M}$ are the gradients between the lengths and the Mach numbers of the northern and southern parts of the outflow, respectively. This sets a lower limit for the inclination of $24 - 33°$, which is consistent with the estimates of the precession model.

We conclude that our estimates in the velocity and the inclination of the nuclear outflow obtained from the precession model are in good agreement with the spectral index distribution analysis of the wide range of frequencies data sample assuming a shock scenario between the outflows and the ICM. The difference in length between both halves of the nuclear outflow must be caused by the acceleration caused by the interaction with the ICM ram pressure.

5.6 Conclusions

As a follow up project of the observations of NGC 4388 from the CHANG-ES project, we have performed a campaign of observations in order to confirm and further study the new features found in the radio halo of this galaxy.

We have observed NGC 4388 at the frequency bands of S-band $(2.0-4.0\,\mathrm{GHz})$ and X-band $(8.0-12.0\,\mathrm{GHz})$ with the BnC- and C-configuration of the VLA. These observations are needed to complement the CHANG-ES observations.

The S-band observations are of special interest because they fill the gap between the C-band and L-band observations of the CHANG-ES sample. In the total power image we resolve the spiral arms as well as the nuclear outflow. The polarized emission map shows polarization only in the southern spot and partly in the southern spiral inter-arm region. The magnetic vectors are mainly parallel to the minor axis of the galaxy in the southern spot. The absence of polarized emission in the northern outflow could mean that this region suffers from strong depolarization already at S-band.

To obtain more details of the properties of the nuclear outflow we also observed this galaxy at X-band. These observations give us the highest resolution of the whole sample. We detect both spiral arms and the nuclear outflow in total power. The images of polarized intensity obtained with RM synthesis show strong polarization of the northern spot with Faraday corrected magnetic vectors pointing towards the north-west. The fact that we do not detect polarized emission towards the nucleus suggest that there is strong depolarization due to the position of the northern nuclear outflow behind the northern spiral arm. The highest resolution image shows a wiggling structure in the northern nuclear outflow, very similar to what it is seen in the southern nuclear outflow of the polarized intensity image of the C-band data set. We suggest that this wiggling features are indeed related and they fit to the precession scenario since together they form an S-shaped outflow.

We also showed new total intensity observations at low frequencies $(610.0\,\mathrm{MHz})$ performed with the GMRT telescope. The total intensity image of these observations show both spiral arms as well as the nuclear outflow. We detect an extended and diffuse region that extends towards the north-east from the galactic disk. This emission correlates with the northern polarized arc of the C-band images obtained from the VLA as well as with the extended Hα outflow found in the halo of the galaxy.

With the broad coverage in frequencies of the combination of these new datasets and the CHANG-ES observations, we performed an spectral index distribution analysis of the nuclear outflow in NGC 4388. We have measured the integrated fluxes for the northern and the southern nuclear outflow at all frequencies available. We obtained spectral indices of $\alpha_{\mathrm{north}} = -0.55 \pm 0.01$ and

$\alpha_{\text{south}} = -1.00 \pm 0.01$ for the total intensity of the northern and southern nuclear outflows, respectively. The fit of these fluxes, with a thermal and a non-thermal components shows a negligible thermal fraction in the northern nuclear outflow.

For explaining this difference between the spectral indices of northern and southern spots, we propose diffusive shock acceleration of CREs produced by the interaction with the ICM environment. Our estimates give Mach numbers of $\mathcal{M}_{\text{north}} = 6.4 \pm 0.30$ ($\alpha_{\text{north}} = -0.55 \pm 0.01$) for the northern spot and of $\mathcal{M}_{\text{south}} = 2.30 \pm 0.02$ ($\alpha_{\text{south}} = -1.00 \pm 0.01$) for the southern one. As the Mach number depends on the velocity and the sound speed of the medium in which the shock is produced, this can be explained by a difference in velocities between the outflows. From Chapter 3 we estimated a sound speed of $\sim (210 \pm 70) \, \text{km} \, \text{s}^{-1}$ which is a reasonable value for the halo of a galaxy. This results in velocities of $v_{\text{north}} \cong (1300 \pm 500) \, \text{km} \, \text{s}^{-1}$ and $v_{\text{south}} \cong (500 \pm 170) \, \text{km} \, \text{s}^{-1}$ for the northern and the southern nuclear outflows, respectively. The action of the ram pressure probably pushes the ISM material towards the north and suppresses the southern outflow, and this is reflected in the spectral indices obtained with radio data.

From the spectral index analysis, assuming an ejection time according to the synchrotron lifetime of $(6.0 - 8.0) \times 10^6 \, \text{yr}$, and according to the lengths of the outflows on the plane of the sky, we also derived a lower limit for the inclination of $\cong 24 - 33°$, which is consistent with the estimates of the precession model.

The different velocities would also explain the difference in length between the polarization filaments seen in this galaxy. A possible explanation for the different velocities could be that they are accelerated. This acceleration might cause the northern outflow to be faster than what the model predicts and slower in the case of the southern outflow. For this reason we think that the precession model should be modified in order to include the action of ram pressure onto the outflow.

We conclude that our estimates in the velocity and the inclination of the nuclear outflow obtained from the precession model are in good agreement with the spectral index distribution analysis of our data sample, supporting the shock scenario between the nuclear outflows and the ICM.

Future Work

Contents

6.1   Future Work

6.1.1   New Hα Observations

NGC 4388 is an outstanding galaxy as several physical processes are simultaneously at play, e.g., ram pressure due to the motion of the galaxy in the dense cluster medium, galactic winds, perhaps driven by star-formation, and also host an AGN. An existing study on this galaxy has shown interesting features in Hα (Yoshida et al., 2002). These Subaru observations show galactic outflows and a complex system of Hα filaments.

New VLA radio observations from the CHANG-ES survey (Irwin et al., 2012) show very interesting features in polarized radio continuum. Our analysis of the $5 - 7\,\mathrm{GHz}$ data (at $5.3''$ resolution) reveals extensions above and below the disk in polarized intensity. The northern arc-like feature in polarized emission closely follows the Hα emission (Yoshida et al., 2004), perhaps caused by a nuclear outflow. Through heuristic calculation of the age of electrons in the blobs we find the velocity to be $\sim 270\,\mathrm{km s}^{-1}$, similar to typical galactic wind velocity. How to produce these coherent features is not well understood. Shock compression of the magnetic field due to the outflows enhances the radio (especially the polarized) continuum emission and it is a possible scenario. For the first time, we detect the southern nuclear outflow in both total and polarization intensity.
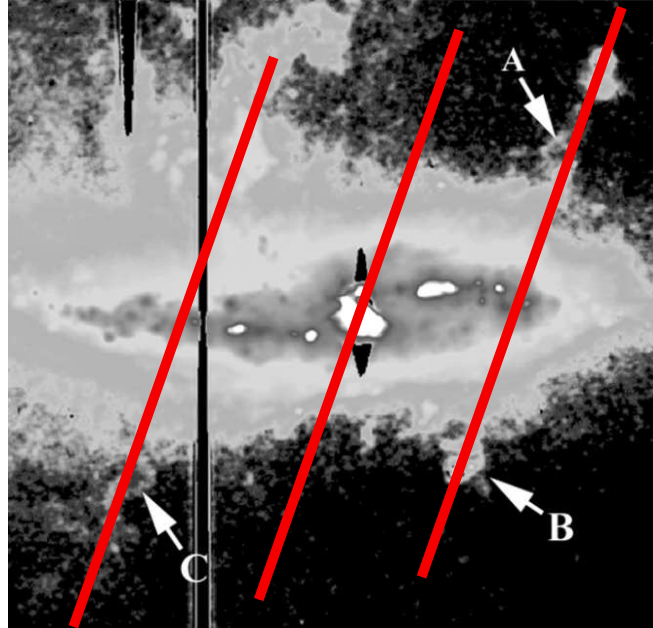
Figure 6.1: Optical map of NGC 4388 from Yoshida et al. 2004. Red lines indicate the orientation of the slits needed.

Therefore, new Hα observations with the Subaru Telescope would be ideal to do deep optical spectroscopy of three particular areas of this galaxy and then constrain their velocities. The comparison between the radio data and the Hα is crucial to confirm the galactic wind scenario and to calculate important parameters of the nuclear outflow such as speed, orientation and energy. We would require a spectral resolution of $\sim 30\,\mathrm{km\,s^{-1}}$ at three different places of the galaxy. We want to cover points A, B and C (see Figure 11 of (Yoshida et al., 2004)) plus an extra slit on the nucleus to get a velocity reference. We estimate a blue-shifted emission in the southern galactic wind (C) and a red-shifted emission on the northern counterpart (A) (see Figure 6.1). As for the southern arc-like structure (B), we expect a red-shifted emission with a speed of the order of that in the northern counter nuclear outflow.

It would be also interesting to perform a study using Integral Field Spectroscopy. This is a novel technique capable of producing velocity maps of Hα in a single observation without the constrains of classical spectroscopic observations where the observation is limited by the size of the slit (Mármol-Queraltó et al., 2011).
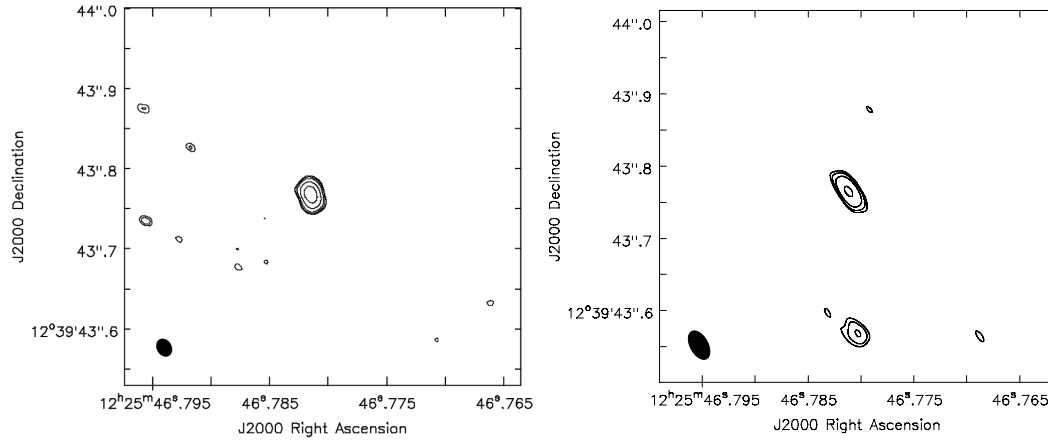
Figure 6.2: Left panel: observations of the nucleus of NGC 4388 at 1.6 GHz with EVN in 2008 from (Giroletti & Panessa, 2009). Total intensity contours of $(3, 4, 6, 12, 24) \times 25\,\mu$Jy beam^{-1}. Right panel: observations of the same region at 1.6 GHz with EVN in 2012. Total intensity contours of $(3, 4, 6, 12, 24) \times 33\,\mu$Jy beam^{-1} (own work). The beam of the observation is shown at the bottom left corner of both images.

6.1.2 VLBI Observations

The AGN of NGC4388 was observed in 2008 with the European VLBI Network (EVN) (Giroletti & Panessa, 2009) at 1.6 GHz and 5.0 GHz. Only the 1.6 GHz observations succeeded to detect the nucleus of this AGN (see left panel of Figure 6.2) with a flux density of 1.3 mJy/beam and an extension of 6 mas. More recent EVN observations (2012) of the same object also at 1.6 GHz show the nucleus as well as an extended spot towards the south (see right panel of Figure 6.2). These new observations seem to reveal an ejection event from the nucleus during the last years. To confirm such scenario we would need new EVN observations. We expect to reach enough signal to noise to detect and confirm the outflow and maybe reveal further new features.

If we detect the new feature we will be able to calculate the speed of the outflow and give some estimates for its energy. These new observations will also be crucial to estimate the inclination of the jet. The ratio between the flux densities of the southern outflow and the noise in the northern counterpart will serve to compute the inclination of the AGN jet thanks to the Doppler boosting effect. VLBI observation (EVN) are of crucial interest if we want to put limits to the speed of individual nuclear ejections.

6.1.3   Further Low Frequencies Observations

Observing the impact of the ICM on halos, winds or nuclear outflows of galaxies is key to improve models of cluster of galaxies. Multi frequency studies of external galaxies and in particular, high sensitivity polarization observations are essential to tune models that explain the evolution of galaxies and the cluster that hosts them. The Virgo cluster is a perfect laboratory to test these interactions since it is dynamically young and therefore it contains a large fraction of spirals. Also, because it is the nearest cluster to us, we can obtain a good compromise between sensitivity and resolution in our observations. Virgo is not the only cluster with these characteristics. For example the Eridanus and the Fornax clusters are only about 20 Mpc away in which about 70 percent of the galaxies are spirals and irregulars while the Coma cluster is too far to study individual galaxies in detail. Eridanus is doable with VLA but Fornax could be a follow-up project for the Squared Kilometre Array (SKA) in the future due to its low declination.

With surveys using broadband receivers we would be able to make further studies of the impact of ICM on the galactic field of galaxies within a cluster environment. These studies could very well be complemented by models describing the effects that we see in the observations. Lower frequency observations with Low Frequency ARray (LOFAR) $(120 - 180\,\mathrm{MHz})$ and upgraded GMRT (uGMRT) $(300 - 600$ and $600 - 900\,\mathrm{MHz})$, where clusters are brighter due to the steep spectral index, would complement the VLA observations. These observations can extend current numerical models of cluster galaxies (Roediger et al., 2006) to include the magnetic field contribution.

A follow up project from these observations could be looking for polarized background radio sources in different clusters. The rotation measure changes with the distance from the cluster center. The radiation of background sources that goes through the ICM of a cluster will get affected by the magnetic field and plasma and we could detect this effect in our Faraday depth maps generated by RM synthesis. For this purpose, we would need high resolution in Faraday space which is only possible using polarization at very low frequencies (LOFAR or GMRT).

6.2   Applying the Precession Model to Other Sources

As precession is present at many different scales, we could apply the same method presented in Chapter 4 to constrain physical properties of nuclear outflows. The combination of this tool with an RM analysis of the radio maps is of great interest to get information about the morphology and evolution of these structures. These
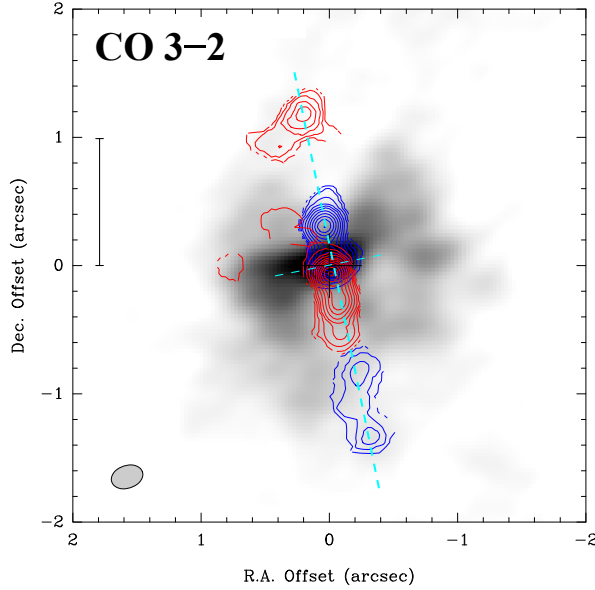
Figure 6.3: ALMA CO $3-2$ ($345\,\mathrm{GHz}$) of the nuclear outflow of a radio-quiet galaxy NGC 1377 Aalto et al. (2016). The systemic velocity is shown in greyscale ($1700-1760\,\mathrm{km\,s^{-1}}$), and velocity reversals of the outflow are shown in red and blue contours. The contours levels are $1.0 \times (1, 2, 3, 4, 5, 6, 7, 8, 9)\,\mathrm{Jy\,km\,s^{-1}\,beam^{-1}}$. The dashed lines represent the orientation of the jet axis and the nuclear disk. The beam shape is represented in the bottom left of the image and the vertical bar indicates a scale of $100\,\mathrm{pc}$.

studies are not necessary restricted to VLA observations since ALMA is also capable of detecting these processes. Aalto et al. 2016 observed a radio quiet galaxy at high resolution CO $3-2$ ($345\,\mathrm{GHz}$) observations with ALMA (see Figure 6.3). They found changes along the jet axis in the velocity of the outflow from $-150\,\mathrm{km\,s^{-1}}$ to $+150\,\mathrm{km\,s^{-1}}$ which could be explained by the precession of a molecular outflow.

6.3 Depolarization Analysis

We have gathered observations of NGC 4388 at many frequency bands in full Stokes. It would be of special interest to perform a depolarization analysis of the polarization spectrum of the polarized outflow features in NGC 4388. Our VLA data shows a decrease of the degree of polarization of the polarized spots in the nuclear outflow, being higher at X-band and C-band and lower at S-band. At L-band the depolarization effects are too strong but we still could use the weak ($\sim 3.5\sigma$) polarization signal detected in the southern spot (see Figure 2.2).

Summary

7.1 Magnetic Outflows of NGC 4388

Our new VLA $5 - 7$ GHz broadband observations of the edge-on Virgo Cluster galaxy NGC 4388 allowed us to reach unprecedentdly low noise levels, revealing striking new details of this object. The polarized emission, obtained for the first time for this galaxy with RM synthesis, shows extensions of the magnetic field toward the outskirts of the galaxy, indicating a connection between disk and halo. Two polarized filamentary structures appear at the end of both northern and southern nuclear outflows, which correlate with features seen in Hα and X-ray observations. The change in orientation of the magnetic vectors (corrected for Faraday rotation) in the southern spiral arm reveals for the first time the southern nuclear outflow. Furthermore, two horizontally extended blobs of polarized emission are observed in the halo, about 2 kpc above and below the northeastern and southwestern spiral arms, respectively, well separated from the nuclear outflows. Within these blobs, the ordered magnetic field is oriented perpendicular to the galactic disk.

The comparison between multiwavelength observations of prototype galactic winds shows that NGC 4388 does not host a symmetric galactic superwind driven by a nuclear starburst. We suggest that, together with Hα, X-ray, and total power emission being located closer to the spiral arms within the halo, the blobs of polarized emission trace a galactic wind, which most likely originates from separate star-formation regions in the spiral arms. In such a scenario the cosmic-ray electrons (CREs) travel from the spiral arms into the halo, reaching projected vertical distances of up to $\cong 3.3$ kpc from the galactic nucleus. Assuming equipartition between total CR particles and the magnetic field, we estimate total magnetic field strengths for different parts of the galaxy taking into account individual spectral indices and path lengths. In particular, our estimate of the total magnetic field strength for the polarization blobs is $(11 \pm 2)\,\mu$G. With this magnetic field strength, the synchrotron lifetime of electrons in the polarized blobs is (12 ± 3) Myr. For traveling a distance of $\cong 3.3$ kpc, the average outflow velocity of those particles is (270 ± 70) km s^{-1}, which agrees with the typical speed of a galactic wind expanding from the spiral arms into the halo.

The observed symmetry of the polarized halo features in NGC 4388 excludes a compression of the halo gas by ICM ram pressure. We estimate the halo

magnetic pressure and the ram pressure of the galactic wind to be $P_{\text{halo}} \approx 3 \times 10^{-12}\,\text{dyn}\,\text{cm}^{-2}$. This pressure is comparable to the thermal pressure derived from X-ray observations. We also estimated an ICM density of $n_{\text{ICM}} \cong 1 \times 10^{-4}\,\text{cm}^{-3}$.

The estimate of the ICM ram pressure based on the velocity of the galaxy from dynamical models and a radially averaged ICM density profile from X-ray observations yields $P_{\text{ICM}} \cong 3 \times 10^{-12}\,\text{dyn}\,\text{cm}^{-2}$, in agreement with our estimate of the thermal halo pressure. Allowing for ICM clumping, the actual ram pressure acting on NGC 4388 might be up to few times higher than what is expected based on a given galaxy velocity and an ICM density determined from X-ray and Sunyaev–Zel'dovich (SZ) observations.

NGC 4388, besides NGC 4569, is the second galaxy in the Virgo Cluster that shows a galactic outflow resisting ICM ram pressure. The detection of a radio halo around other cluster spiral galaxies could be used for an estimate of ICM density and ram pressure within a factor of a few.

7.2 Precession of the Nuclear Outflow of NGC 4388

We found an asymmetry in the rotation measure (RM) pattern of the southern part of the northern spot at the end of the northern nuclear outflow. The RMs vary from negatives values to positive values along the spot, in an area that is covered by $\cong 9$ beam areas. The RM profile of this spot can be explained by a magnetic field changing its direction along the line of sight. We suspect that this RM asymmetry could be due to the action of a precessing nuclear outflow of the northern and southern filaments with respect to the center of the galaxy. Another indication of the precession is the wiggling structure seen in the magnetic field vectors (RM-corrected) along the southern nuclear outflow. The RM of the southern nuclear outflow shows a change $\cong 300\,\text{rad}\,\text{m}^{-2}$ that indicates the presence of a structure in front of the spiral arms. After the change in orientation of the magnetic field vectors at the minor axis of the galactic disk, the change in the RM values is the second indication of a helical outflow structure. These evidences are only seen thanks to the radio polarized observations.

We adopted a precession model for the accretion disc around the AGN and the nuclear outflow. This gives similar structures in the morphology of the radio polarization filaments in the halo of NGC 4388. We developed an interactive tool to constrain the precession parameters from astronomical observations.

To constrain the parameters of the precession model we set the total time of ejection to the synchrotron life time of the electrons at the very end of the radio polarization filaments. We also used the position angle of the maser disk found in this galaxy to fix the present day position angle of the ejections. With this

assumption the model can well reproduce the large scale polarization filaments. This indicates a connection between the circumnuclear megamaser disk seen at parsec scales next to the nucleus and the structures seen at kiloparsec scales of the polarization filaments.

Limited by the synchrotron life time of the CREs in the polarization outflows, which is estimated to be $t \cong (6.0 - 8.0) \times 10^6 \, \mathrm{yr}$, the precession model estimates an inclination of $i \cong 15 - 50°$ towards the observer, an opening angle of $\phi \cong 3 - 10°$, and a position angle of $\chi \cong 13°$ on the plane of the sky. We also estimate a velocity of $1300 - 2300 \, \mathrm{km \, s^{-1}}$ and $500 - 1000 \, \mathrm{km \, s^{-1}}$ for the northern and southern parts of the nuclear outflow, respectively, which are consistent with the velocities obtained from Hα studies. The action of the ram pressure probably pushes the ISM material towards the north and suppresses the southern outflow. The period of the precession is estimated to be $P \cong (3.5 - 4.5) \times 10^6 \, \mathrm{yr}$. With this set of values, both polarization filaments seen in the radio data are well reproduced in extension and shape by a ballistic precessing outflow. Furthermore, the convolved model to match the resolution of the VLA reproduces the two spots seen to the north and south of the nucleus in both radio polarization and total power.

As a second test, we included the direction of the precessing outflow with respect to the observer along the line of sight. The convolution of this model map shows a similar structure to that seen in the RM map of the northern spot. The RM map of the radio observations shows an asymmetry from negative to positive RMs across the northern nuclear outflow. The map of the modeled precession shows the same structure at that point due to a change in the direction of the outflow. We interpret this similarity as the result of the magnetic field following the helical direction of a precessing nuclear outflow. This test gives an independent indication of precession being a plausible scenario in the nuclear outflow of this galaxy.

7.3 Further Radio Observations of NGC 4388

To complement the CHANG-ES observations we observed NGC 4388 at the S $(2 - 4 \, \mathrm{GHz})$ and X $(8 - 12 \, \mathrm{GHz})$ frequency bands of the VLA in order to confirm and further study the new features found in the radio halo of this galaxy.

The S-band observations are of special interest because they fill the gap between the C-band $(5 - 7 \, \mathrm{GHz})$ and L-band $(1 - 2 \, \mathrm{GHz})$ observations of the CHANG-ES sample. The polarized emission map shows polarization only in the southern spot and partly in the southern spiral inter-arm region. The magnetic vectors are mainly parallel to the minor axis of the galaxy in the southern spot. The absence of polarized emission in the northern outflow could mean that this region suffers from strong depolarization already at S-band.

To obtain more details of the properties of the nuclear outflow we also ob-
served this galaxy at X-band. These observations give us the highest resolution of
the whole sample. The images of polarized intensity obtained with RM synthesis
show strong polarization of the northern spot with Faraday corrected magnetic
vectors pointing towards the north-west. The fact that we do not detect polar-
ized emission towards the nucleus suggest that there is strong depolarization due
to the position of the northern nuclear outflow behind the northern spiral arm.
The highest resolution image shows a wiggling structure in the northern nuclear
outflow, very similar to what it is seen in the southern nuclear outflow of the
polarized intensity image of the C-band data set. We suggest that these wiggling
features are related and fit to the precession scenario since together they form
an S-shaped outflow.

We also showed new total intensity observations at low frequencies (610 MHz)
performed with the GMRT telescope. The total intensity image of these obser-
vations show both spiral arms as well as the nuclear outflow. We detect an
extended and diffuse region that extends towards the north-east from the galac-
tic disk. This emission correlates with the northern polarized arc of the C-band
images obtained from the VLA as well as with the extended Hα outflow found
in the halo of the galaxy.

An spectral distribution analysis of the nuclear outflow in NGC 4388 shows
spectral indices of $\alpha_s = -0.55$ and $\alpha_s = -1.00$ for the total intensity of the
northern and southern nuclear outflows, respectively. For explaining this differ-
ence we propose the scenario of diffusive shock acceleration of CREs produced
by the interaction with the ICM environment. Our estimates give Mach num-
bers of $\mathcal{M}_n = 6.4 \pm 0.30$ ($\alpha_n = -0.55 \pm 0.01$) for the northern spot and of
$\mathcal{M}_s = 2.30 \pm 0.02$ ($\alpha_s = -1.00 \pm 0.01$) for the southern one. As the Mach
number depends on the velocity and the sound speed of the medium in which
the shock is produced, this can be explained by a difference in outflows ve-
locities. From Chapter 3 we estimated a sound speed of $\cong (210 \pm 70)\,\mathrm{km\,s^{-1}}$
which is a reasonable value for the halo of a galaxy. This results in velocities
of $v_{\mathrm{north}} \cong (1300 \pm 500)\,\mathrm{km\,s^{-1}}$ and $v_{\mathrm{south}} \cong (500 \pm 170)\,\mathrm{km\,s^{-1}}$ for the northern
and the southern nuclear outflows, respectively. This is reflected in the spectral
indices obtained with radio data. From the spectral index analysis, assuming
an ejection time according to the synchrotron lifetime of $(6.0 - 8.0) \times 10^6\,\mathrm{yr}$,
and according to the lengths of the outflows on the plane of the sky, we also
derive a lower limit for the inclination of $\cong 24 - 33°$, which is consistent with
the estimates of the precession model.

We conclude that our estimates in the velocity and the inclination of the
nuclear outflow obtained from the precession model are in good agreement with
the spectral index distribution analysis of our data sample, supporting the shock
scenario between the nuclear outflows and the ICM.

Bibliography

Aalto, S., Costagliola, F., Muller, S., et al. 2016, A&A, 590, A73 (Cited on page 97.)

Abadi, M. G., Moore, B., & Bower, R. G. 1999, MNRAS, 308, 947 (Cited on page 9.)

Adebahr, B. 2013, PhD thesis, University of Bochum (Cited on page 19.)

Adebahr, B., Krause, M., Klein, U., et al. 2013, A&A, 555, A23 (Cited on page 35.)

Allen, R. J., Sancisi, R., & Baldwin, J. E. 1978, A&A, 62, 397 (Cited on page 13.)

Arribas, S., Colina, L., Bellocchi, E., Maiolino, R., & Villar-Martín, M. 2014, A&A, 568, A14 (Cited on page 38.)

Arshakian, T. G., & Beck, R. 2011, MNRAS, 418, 2336 (Cited on page 31.)

Bardeen, J. M., & Petterson, J. A. 1975, ApJ, 195, L65 (Cited on page 48.)

Basu, A., Mitra, D., Wadadekar, Y., & Ishwara-Chandra, C. H. 2012, MNRAS, 419, 1136 (Cited on page 81.)

Beck, R. 2001, Space Sci. Rev., 99, 243 (Cited on page 30.)

—. 2007, A&A, 470, 539 (Cited on page 34.)

—. 2015, A&A, 578, A93 (Cited on page 2.)

—. 2016, A&A Rev., 24, 4 (Cited on page 1.)

Beck, R., & Krause, M. 2005, Astronomische Nachrichten, 326, 414 (Cited on pages 7, 30, 33 and 38.)

Beck, R., & Wielebinski, R. 2013, in Planets, Stars and Stellar Systems. Volume 5: Galactic Structure and Stellar Populations, ed. T. D. Oswalt & G. Gilmore, 641 (Cited on pages 29 and 38.)

Begelman, M. C., King, A. R., & Pringle, J. E. 2006, MNRAS, 370, 399 (Cited on page 48.)

Bicknell, G. V., Dopita, M. A., Tsvetanov, Z. I., & Sutherland, R. S. 1998, ApJ, 495, 680 (Cited on page 58.)

Binggeli, B., Sandage, A., & Tammann, G. A. 1985, AJ, 90, 1681 (Cited on page 9.)

Bîrzan, L., Rafferty, D. A., McNamara, B. R., Wise, M. W., & Nulsen, P. E. J. 2004, ApJ, 607, 800 (Cited on page 17.)

Blandford, R., & Eichler, D. 1987, Phys. Rep., 154, 1 (Cited on page 86.)

Böhringer, H., Briel, U. G., Schwarz, R. A., et al. 1994, Nature, 368, 828 (Cited on pages 41 and 89.)

Brentjens, M. A., & de Bruyn, A. G. 2005, A&A, 441, 1217 (Cited on pages 6, 27 and 28.)

Brunetti, G., & Jones, T. W. 2014, International Journal of Modern Physics D, 23, 1430007 (Cited on page 86.)

Burn, B. J. 1966, MNRAS, 133, 67 (Cited on page 6.)

Cayatte, V., van Gorkom, J. H., Balkowski, C., & Kotanyi, C. 1990, AJ, 100, 604 (Cited on page 24.)

Cecil, G., Greenhill, L. J., DePree, C. G., et al. 2000, ApJ, 536, 675 (Cited on page 48.)

Chamandy, L., Subramanian, K., & Shukurov, A. 2013, MNRAS, 428, 3569 (Cited on page 2.)

Chamaraux, P., Balkowski, C., & Gerard, E. 1980, A&A, 83, 38 (Cited on page 9.)

Chung, A., van Gorkom, J. H., Kenney, J. D. P., Crowl, H., & Vollmer, B. 2009, AJ, 138, 1741 (Cited on pages 9, 24, 37 and 42.)

Chyży, K. T., Soida, M., Bomans, D. J., et al. 2006, A&A, 447, 465 (Cited on pages 42 and 46.)

Dahlem, M. 1997, PASP, 109, 1298 (Cited on page 35.)

Damas-Segovia, A., Beck, R., Vollmer, B., et al. 2016, ApJ, 824, 30 (Cited on page 46.)

Dressler, A. 1980, ApJ, 236, 351 (Cited on page 8.)

Dunn, R. J. H., Allen, S. W., Taylor, G. B., et al. 2010, MNRAS, 404, 180 (Cited on page 17.)

Ekers, R. D., Fanti, R., Lari, C., & Parma, P. 1978, Nature, 276, 588 (Cited on page 66.)

Falcke, H., Wilson, A. S., & Simpson, C. 1998, ApJ, 502, 199 (Cited on pages 24, 29 and 33.)

Fouqué, P., Solanes, J. M., Sanchis, T., & Balkowski, C. 2001, A&A, 375, 770 (Cited on page 9.)

Fraternali, F., & Binney, J. J. 2006, MNRAS, 366, 449 (Cited on page 3.)

Gabuzda, D. C., Knuettel, S., & Reardon, B. 2015, MNRAS, 450, 2441 (Cited on pages 52 and 62.)

Giovanelli, R., & Haynes, M. P. 1983, AJ, 88, 881 (Cited on page 9.)

Giroletti, M., & Panessa, F. 2009, ApJ, 706, L260 (Cited on pages 24, 55 and 95.)

Gower, A. C., Gregory, P. C., Unruh, W. G., & Hutchings, J. B. 1982, ApJ, 262, 478 (Cited on page 54.)

Gunn, J. E., & Gott, I. J. R. 1972, ApJ, 176, 1 (Cited on pages 9 and 42.)

Heald, G. 2009, in IAU Symposium, Vol. 259, IAU Symposium, ed. K. G. Strassmeier, A. G. Kosovichev, & J. E. Beckman, 591–602 (Cited on pages 6 and 27.)

Heald, G. 2015, in Astrophysics and Space Science Library, Vol. 407, Magnetic Fields in Diffuse Media, ed. A. Lazarian, E. M. de Gouveia Dal Pino, & C. Melioli, 41 (Cited on pages 6 and 27.)

Heesen, V., Beck, R., Krause, M., & Dettmar, R.-J. 2009, A&A, 494, 563 (Cited on pages 3, 38 and 80.)

Hjellming, R. M., & Johnston, K. J. 1981, ApJ, 246, L141 (Cited on page 54.)

Hummel, E., Beck, R., & Dettmar, R.-J. 1991, , 87, 309 (Cited on page 13.)

Hummel, E., & Saikia, D. J. 1991, A&A, 249, 43 (Cited on pages 24 and 29.)

Hummel, E., van Gorkom, J. H., & Kotanyi, C. G. 1983, ApJ, 267, L5 (Cited on page 24.)

Hunter, J. D. 2007, Computing In Science & Engineering, 9, 90 (Cited on page 57.)

Iacobelli, M., Haverkorn, M., & Katgert, P. 2013, A&A, 549, A56 (Cited on page 52.)

Irwin, J., Beck, R., Benjamin, R. A., et al. 2012, AJ, 144, 43 (Cited on pages 14, 15, 26 and 93.)

Iwasawa, K., Wilson, A. S., Fabian, A. C., & Young, A. J. 2003, MNRAS, 345, 369 (Cited on pages 24, 34, 36 and 48.)

Kellermann, K. I., Kovalev, Y. Y., Lister, M. L., et al. 2007, Ap&SS, 311, 231 (Cited on page 32.)

Kennicutt, J. R. C. 1983, AJ, 88, 483 (Cited on page 9.)

Kharb, P., O'Dea, C. P., Baum, S. A., Colbert, E. J. M., & Xu, C. 2006, ApJ, 652, 177 (Cited on page 54.)

Klein, U., & Fletcher, A. 2015, Galactic and Intergalactic Magnetic Fields (Cited on pages 4 and 5.)

Krause, M. 2009, in Revista Mexicana de Astronomia y Astrofisica Conference Series, Vol. 36, Revista Mexicana de Astronomia y Astrofisica Conference Series, 25–29 (Cited on page 3.)

Krause, M. 2011, ArXiv e-prints, arXiv:1111.7081 (Cited on page 30.)

Kronberg, P. P., Lesch, H., & Hopp, U. 1999, ApJ, 511, 56 (Cited on page 3.)

Kukula, M. J., Pedlar, A., Baum, S. A., & O'Dea, C. P. 1995, MNRAS, 276, 1262 (Cited on pages 24 and 29.)

Kulsrud, R. M., & Zweibel, E. G. 2008, Reports on Progress in Physics, 71, 046901 (Cited on page 1.)

Kuo, C. Y., Braatz, J. A., Condon, J. J., et al. 2011, ApJ, 727, 20 (Cited on pages 24, 55 and 67.)

Li, J.-T., Li, Z., Wang, Q. D., Irwin, J. A., & Rossa, J. 2008, MNRAS, 390, 59 (Cited on page 35.)

Lin, C. C., & Shu, F. H. 1964, ApJ, 140, 646 (Cited on page 2.)

Lobanov, A. P., & Roland, J. 2005, A&A, 431, 831 (Cited on page 66.)

Longair, M. S. 1994, High energy astrophysics. Volume 2. Stars, the Galaxy and the interstellar medium. (Cited on page 3.)

Lu, J.-F., & Zhou, B.-Y. 2005, ApJ, 635, L17 (Cited on page 66.)

Mármol-Queraltó, E., Sánchez, S. F., Marino, R. A., et al. 2011, A&A, 534, A8 (Cited on page 94.)

Middelberg, E., Roy, A. L., Nagar, N. M., et al. 2004, A&A, 417, 925 (Cited on page 58.)

Miley, G. 1980, ARA&A, 18, 165 (Cited on page 66.)

Moore, B., Katz, N., Lake, G., Dressler, A., & Oemler, A. 1996, Nature, 379, 613 (Cited on page 9.)

Mora, S. C., & Krause, M. 2013, A&A, 560, A42 (Cited on page 3.)

Mundell, C. G., Wilson, A. S., Ulvestad, J. S., & Roy, A. L. 2000, ApJ, 529, 816 (Cited on page 55.)

Nulsen, P. E. J. 1982, MNRAS, 198, 1007 (Cited on page 9.)

Oosterloo, T., & van Gorkom, J. 2005, A&A, 437, L19 (Cited on pages 24 and 25.)

Oppermann, N., Junklewitz, H., Robbers, G., et al. 2012, A&A, 542, A93 (Cited on page 51.)

Pappalardo, C., Lançon, A., Vollmer, B., et al. 2010, A&A, 514, A33 (Cited on pages 24 and 41.)

Pearson, T. J., & Zensus, J. A. 1987, in Superluminal Radio Sources, ed. J. A. Zensus & T. J. Pearson, 1–11 (Cited on page 32.)

Perley, R. A., & Butler, B. J. 2013, ApJS, 204, 19 (Cited on page 15.)

Perucho, M., Martí, J. M., Laing, R. A., & Hardee, P. E. 2014, MNRAS, 441, 1488 (Cited on pages 53 and 89.)

Pizzo, R. F., & de Bruyn, A. G. 2009, A&A, 507, 639 (Cited on page 19.)

Planck Collaboration, Ade, P. A. R., Aghanim, N., et al. 2015, ArXiv e-prints, arXiv:1511.05156 (Cited on pages 42 and 44.)

Ranalli, P., Comastri, A., Origlia, L., & Maiolino, R. 2008, MNRAS, 386, 1464 (Cited on page 35.)

Rau, U., & Cornwell, T. J. 2011, A&A, 532, A71 (Cited on page 15.)

Roberts, D. H., Wardle, J. F. C., Lipnick, S. L., Selesnick, P. L., & Slutsky, S. 2008, ApJ, 676, 584 (Cited on page 61.)

Roediger, E., & Brüggen, M. 2008, MNRAS, 388, 465 (Cited on page 41.)

Roediger, E., Brüggen, M., & Hoeft, M. 2006, MNRAS, 371, 609 (Cited on pages 41, 44, 45 and 96.)

Shakura, N. I., & Sunyaev, R. A. 1973, A&A, 24, 337 (Cited on page 67.)

Soida, M., Krause, M., Dettmar, R.-J., & Urbanik, M. 2011, A&A, 531, A127 (Cited on pages 35 and 36.)

Sokoloff, D. D., Bykov, A. A., Shukurov, A., et al. 1998, MNRAS, 299, 189 (Cited on page 31.)

Stella, L., & Vietri, M. 1998, ApJ, 492, L59 (Cited on page 48.)

Stirling, A. M., Spencer, R. E., Cawthorne, T. V., & Paragi, Z. 2004, MNRAS, 354, 1239 (Cited on page 61.)

Strickland, D. K., Heckman, T. M., Weaver, K. A., Hoopes, C. G., & Dahlem, M. 2002, ApJ, 568, 689 (Cited on pages 34 and 35.)

Strickland, D. K., Ponman, T. J., & Stevens, I. R. 1997, A&A, 320, 378 (Cited on page 35.)

Swaters, R. A., Sancisi, R., & van der Hulst, J. M. 1997, ApJ, 491, 140 (Cited on page 3.)

Tonnesen, S., & Bryan, G. L. 2009, ApJ, 694, 789 (Cited on page 45.)

Urban, O., Werner, N., Simionescu, A., Allen, S. W., & Böhringer, H. 2011, MNRAS, 414, 2101 (Cited on pages 42 and 44.)

Veilleux, S., Bland-Hawthorn, J., Cecil, G., Tully, R. B., & Miller, S. T. 1999, ApJ, 520, 111 (Cited on page 38.)

Vikhlinin, A., Markevitch, M., & Murray, S. S. 2001, ApJ, 551, 160 (Cited on page 41.)

Vollmer, B. 2009, A&A, 502, 427 (Cited on pages 25, 41, 43 and 44.)

Vollmer, B., Cayatte, V., Balkowski, C., & Duschl, W. J. 2001, ApJ, 561, 708 (Cited on pages 25 and 45.)

Vollmer, B., & Huchtmeier, W. 2003, A&A, 406, 427 (Cited on pages 24, 41, 65 and 81.)

Vollmer, B., Soida, M., Beck, R., et al. 2013, A&A, 553, A116 (Cited on pages 8, 10 and 25.)

—. 2007, A&A, 464, L37 (Cited on pages 25 and 42.)

Vollmer, B., Soida, M., Chung, A., et al. 2010, A&A, 512, A36 (Cited on pages 24, 25 and 42.)

—. 2008, A&A, 483, 89 (Cited on page 42.)

Weisberg, J. M., Romani, R. W., & Taylor, J. H. 1989, ApJ, 347, 1030 (Cited on page 48.)

Weżgowiec, M., Urbanik, M., Beck, R., Chyży, K. T., & Soida, M. 2012, A&A, 545, A69 (Cited on pages 24 and 25.)

Weżgowiec, M., Vollmer, B., Ehle, M., et al. 2011, A&A, 531, A44 (Cited on pages 25, 31 and 40.)

Wiegert, T., Irwin, J., Miskolczi, A., et al. 2015, AJ, 150, 81 (Cited on pages 22 and 26.)

Wielebinski, R., & Beck, R., eds. 2005, Lecture Notes in Physics, Berlin Springer Verlag, Vol. 664, Cosmic Magnetic Fields (Cited on page 1.)

Yasuda, N., Fukugita, M., & Okamura, S. 1997, ApJS, 108, 417 (Cited on page 9.)

Yoshida, M., Yagi, M., Okamura, S., et al. 2002, ApJ, 567, 118 (Cited on pages 21, 24, 27, 29, 31, 34, 35, 44, 48, 58, 64 and 93.)

Yoshida, M., Ohyama, Y., Iye, M., et al. 2004, AJ, 127, 90 (Cited on pages 24, 29, 34, 43, 63, 65, 82, 93 and 94.)

Zhuravleva, I., Churazov, E., Kravtsov, A., et al. 2013, MNRAS, 428, 3274 (Cited on page 44.)

Erklärung

Ich versichere, dass ich die von mir vorgelegte Dissertation selbständig angefertigt, die benutzten Quellen und Hilfsmittel vollständig angegeben und die Stellen der Arbeiteinschlielich Tabellen, Karten und Abbildungen –, die anderen Werken im Wortlaut oder dem Sinn nach entnommen sind, in jedem Einzelfall als Entlehnung kenntlich gemacht habe; dass diese Dissertation noch keiner anderen Fakultät oder Universität zur Prfung vorgelegen hat; dass sie noch nicht verffentlicht worden ist sowie, da ich eine solche Veröffentlichung vor Abschluss des Promotionsverfahrens nicht vornehmen werde. Die Bestimmungen dieser Promotionsordnung sind mir bekannt. Die von mir vorgelegte Dissertation ist von Prof. Dr. Michael Kramer betreut worden.

Unterschift:
_____ -

Datum: